Marangoni convection : numerical model and experiments

Marangoni Convection:

Numerical Model and Experiments

A.W.J.P. den Boer

Marangoni Convection:
Numerical Model and Experiments

Marangoni Convection:
Numerical Model and Experiments

PROEFSCHRIFT

ter verkrijging van de graad van doctor aan de
Technisch Universiteit Eindhoven, op gezag van
de Rector Magnificus, prof. dr. M. Rem, voor
een commissie aangewezen door het College van
Dekanen in het openbaar te verdedigen op
woensdag 27 november om 16.00 uur

door
Antonius Waltherus Jacobus Petrus den Boer
geboren te Tilburg

Dit proefschrift is goedgekeurd door de promotoren:

prof. ir. J.K. Nieuwenhuizen
en
prof. dr. ir. H.W.M. Hoeijmakers

Copromotor: dr. C.W.M. van der Geld

Boer, Antonius Waltherus Jacobus Petrus den

Marangoni Convection: Numerical Model and Experiments /
Antonius Waltherus Jacobus Petrus den Boer. – Eindhoven: Technische
Universiteit Eindhoven
Proefschrift Technische Universiteit Eindhoven. – Met lit.
opg. – Met samenvatting in het Nederlands.
ISBN 90–386–0049–6

Contents

Chapter 1

Motivation, objectives and outline of the present study

1.1 Introduction and objectives

In the design of process equipment the prediction of liquid flow and gas-liquid interface behaviour is of great importance. Most predictive tools are nowadays based on numerical algorithms to solve the governing equations. In the bulk liquid, the governing equations account for the external forces, such as gravity, and shear forces due to the viscosity of the liquid. These are the well-known Navier-Stokes equations. At gas-liquid interfaces other forces are active. Stresses related to surface tension act in a direction normal to the interface; these stresses cause bubbles to have a (nearly) spherical shape. Stresses caused by a gradient of the surface tension, however, act parallel to the gas-liquid interface. The flow caused by this tangential stress at the gas-liquid interface is referred to as Marangoni convection [1]. A gradient in the surface tension at a gas-liquid interface can be caused by:

- a temperature gradient, it causes the so-called thermocapillary effect [1][2][3][4][5][6][7][8][9][10].
- a concentration gradient, it causes the so-called destillocapillary effect. A concentration gradient is caused by:
  - a solvent inhomogeneously evaporating from the liquid [11]
  - a solvent inhomogeneously dissolved in the liquid [12]
  - a concentration gradient of soluble surfactants at the surface [13][14][15][16].
- an electrical potential [17].

The objectives of this study are:

- to develop an algorithm to facilitate the prediction of Marangoni convection,
- to perform experiments to quantify the Marangoni forces in some practical applications where a temperature gradient causes a surface tension gradient.

In section 1.2 some practical applications of Marangoni convection are described. In section 1.3 existing numerical tools are described and compared. In section 1.4 a new computational method is proposed and motivated. In section 1.5 the experiments are outlined and motivated.

[1] Named after the Italian Physicist Carlo Marangoni (1840-1925).

1.2 On the importance of Marangoni convection; the applicability of this study

Marangoni convection is of great interest for the industry. It is applied, for instance, to the drying of hydrophilic surfaces [12]. Silicon wafers are hydrophilic surfaces which are used for the production of integrated circuits. Vapour of a water-soluble organic liquid is inhomogeneously absorbed into the water meniscus on a partially immersed solid substrate. Due to differences in absorption along the meniscus interface, see Fig. 1.1, a surface tension gradient is induced. The gradient causes the meniscus to contract through a Marangoni flow which dries the substrate and causes the water-vapour interface to flatten, as desired. Residual film thickness with this type of drying is more than one order of magnitude smaller than with conventional (spin) drying.

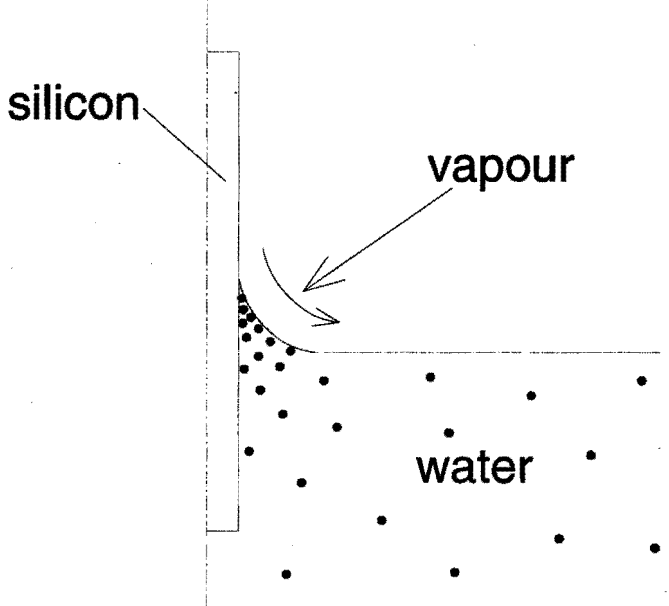

Figure 1.1: Marangoni drying of hydrophilic surface.

A second example is heat recovery and cleaning of exhaust gases with the aid of plastic compact heat exchangers. In such applications, heat is transferred from an air/steam-mixture to cooling water. On the plastic condenser plates the condensation occurs dropwise. Along the interface of the drops a temperature gradient is induced which causes thermocapillary Marangoni convection, see Fig. 1.2. These Marangoni flows may increase the net heat transfer rates [1].

Yet another example is cooling equipment in space. A liquid is externally heated and bubbles are formed at a wall. If some air is still present to allow for a varying partial vapour pressure at the inside of the bubble, bubbles attached to the wall have a varying surface tension due to a temperature gradient in the boundary layer of the liquid along the wall. The resulting thermocapillary motion dominates buoyancy in microgravity conditions and hence influences bubble growth and detachment [18].

Marangoni convection also plays an important role in thin layers of paint, coatings, glues [15], welding, metallurgy, printing ink on solid walls and in floating zones in crystals growth in space

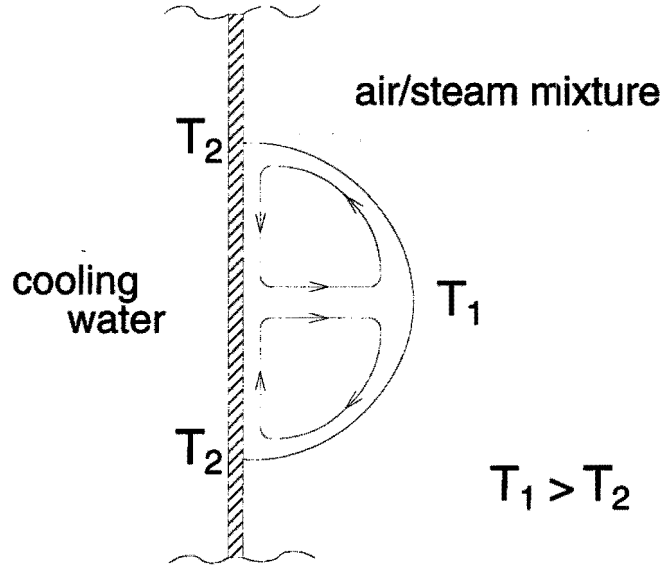

Figure 1.2: Marangoni convection in droplets.

[2][9][10] or material processing applications [5].

In this thesis, a predictive tool of Marangoni convection and related interfacial behaviour is presented. The geometries studied have been chosen such that they are generic for realistic situations. This work aims at facilitating the simulation of Marangoni flows in, for example, the applications described above.

1.3 Existing numerical tools

Several tools nowadays exist for numerically solving the governing equations of Marangoni flows [19][20][21]. They are surveyed below in order to facilitate the introduction of a new computational method in section 1.4 and in order to sketch the capabilities of current predictive tools. It is emphasized that this survey may be far from complete from a numerical point of view. It is, however, intended as a general guide and introduction to the mechanical engineer who usually merely applies the methods developed by others.

Main categories in which the numerical tools can be divided are:

1. the Finite Difference Method (FDM),
2. the Boundary Element Method (BEM),
3. the Finite Element Method (FEM),
4. the Collocation Method (CM).

A common drawback of these techniques is that usually problems arise with the accuracy, reliability and calculation time when free boundaries with dynamic conditions have to be taken into account.

Since the problem addressed in this thesis involves free boundaries with special stress conditions these are relevant drawbacks that have to be fully assessed and, if possible, solved adequately.

The calculation time of FDM, see appendix A, is large when the governing equations have the complexity that is common in dynamic interface simulations. Another disadvantage is that if the boundaries are curved the formulation of FDM is more difficult. A solution is interpolation, but this makes the problem more complex especially when complicated boundary conditions have to be imposed. Also local grid refining near the boundaries is hard to apply, which makes FDM less flexible than other methods as FEM. A transformation from the physical space to a computational space could in principle solve problems with curved boundaries, but this too is complex in many applications. In addition, artificial oscillations may occur if due to the boundary condition the solution near the boundary fluctuates strongly. These features of FDM are discussed in more detail in appendix A.

The application of BEM, see appendix A, has been merely successful for solving linear homogeneous differential equations and gets complicated for other equations, e.g. the full Navier-Stokes equations. Extra source terms must then be taken into account that render the numerical treatment with BEM complex. Some features of BEM are discussed in appendix A.

In FEM a solution is constructed by minimisation (e.g. Ritz-method) or by weighted residuals (e.g. Galerkin method). In the former method a matrix is generated that in general is dense. Its condition number is bad and, when many elementary functions are used, rounding-off errors may be hard to control. The Galerkin method is more general in use and more direct. A disadvantage of both methods is that numerical problems occur in the velocity-pressure formulation for the pressure p since the continuity equation does not contain the pressure. This makes the handling of problems with stress conditions at an interface involving the pressure cumbersome. Several ways are nowadays known to address this coupling problem. Advantages and drawbacks of these tools are described in appendix A.

The fourth method, the collocation method (CM), is a special form of FEM with the weight function chosen as the Dirac Delta-function centred at the collocation points:

$$\phi_i = \Delta(x - x_i) \quad i = 1, .., N \tag{1.1}$$

with:

$$\Delta(x) = \lim_{\Delta \to 0} \begin{cases} 0 & x < -\dfrac{\Delta}{2} \\ \dfrac{1}{\Delta} & -\dfrac{\Delta}{2} < x < \dfrac{\Delta}{2} \\ 0 & x > \dfrac{\Delta}{2} \end{cases} \tag{1.2}$$

and

$$\int_x \Delta(x - x_i)\, dx = 1 \tag{1.3}$$

In the present study this method is applied as further discussed in section 1.4.

In combination with FEM or CM spectral methods can be used. Spectral methods in an orthogonal system encompass a linear transformation between the (exact) solution and a sequence of expansion coefficients. This is usually called the finite transform between the physical space and a transformed space. An example is the approximation of periodic functions by a Fourier-series. Functions can be described both through their values in physical space and through their coefficients in transformed space. Spectral methods are based on weighted residual techniques, see appendix A. Exponential

convergence [2] (or spectral accuracy) is obtained if the exact solution is known to be a series of special expansion functions.

Spectral accuracy is guaranteed, see Canuto et al. [22], if orthogonal systems are used as basic functions with suitable interpolation points.

In this thesis spectral techniques are applied in the numerical method to be presented.

All the techniques described above have been applied for solving the partial differential equations, PDEs, that govern liquid motion with stress conditions at free interfaces, see section 1.1. Some examples are given below to show that this was not without problems for difficult situations [23][24][25].

Strani et al. [24] used a computational method for thermocapillary convection in a rectangular cavity based on finite differences in curvilinear coordinates with the surface deformation of the interface neglected. Although the results look reliable, they did not represent solutions for free interfaces.

Lu [23] used BEM to analyze thermocapillary convection near a free surface in a rectangular cavity with heated isothermal side walls in microgravity. He found reliable results when the interface was immobile and straight. He found a large deformation of the interface when the interface was mobile, which was not verified by other researchers.

Shopov et al. [25] used FEM to model the transient behaviour of deformable liquid interfaces with surface tension effects. The method works good for relatively large deformations of the free surface but is not robust in the case of small deformations.

It is concluded that good solutions have been obtained, with existing techniques, for problems with fixed interfaces, but that with a free interface with the stress conditions that govern Marangoni flows, no fully reliable methods were reported. The main problems seem to be difficulties in adapting the grid to a moving, free interface, the number of iterations necessary at each timestep, numerical diffusion, the velocity-pressure coupling and the form of the stress conditions at the free interface. In this thesis a new method is presented to describe thermocapillary convection of deformable gas-liquid interfaces with interfacial stress conditions. This method is outlined in section 1.4. Some of the problems mentioned above will be seen to be solved. The solution obtained is, for example, fully closed. No iterations are necessary at a timestep.

1.4 Outline of the new algorithm

In the method presented in this study, the Navier-Stokes equations, subject to the appropriate boundary conditions, are solved numerically to determine the flow field of the Marangoni driven convection. The method predicts the evolution in time of the velocity in a thin liquid layer and the corresponding free interface motion. The gradient in the tangential surface tension at the free interface is prescribed, e.g. obtained from experimental observations to be described below. The pressure is eliminated by integrating the Navier-Stokes equations along closed contours intersecting the free surface while using the normal stress condition at the interface. The contour integrals result in expressions which are linear in the unknown coefficients of the expansion used for the velocity field. The algorithm, based on a spectral collocation method with a self-adapting grid of collocation points, simultaneously satisfies the contour-integrated Navier-Stokes equations as well as the tangential stress condition at the points of the free interface. Advantages of the method used are:

- the simplicity to accommodate physical symmetries via the basis functions [26],
- its potential for rapid grid convergence

[2] Exponential convergence means that the approximation converges exponentially to the exact solution when increasing the number of test functions.

- the possibility to determine derivatives of the solution analytically.

For the computation of the nonlinear terms the fast Fourier technique cannot be used. An adapted Singular-Value-Decomposition (SVD) method is applied which weights the contour-integrated Navier-Stokes equations and the tangential stress condition and achieves spectral accuracy. The precise location of the collocation points is not crucial since in the SVD method much more computational points are used than necessary. Since the tangential stress condition is driving the flow it is central in and even guide the solution procedure.

The coupling of the velocity field and the interface motion, as prescribed by the kinematic boundary condition, is achieved in a direct manner utilizing a series of orthogonal functions for both the velocity field and the position of the interfacial contour combined with an Adams-Bashford integration technique. Since the solution of the velocity field and the interface position are based on truncated expansions the accuracy of the solution is directly controlled. An explicit time integration is used, so that the solution at the next time level is obtained directly without iteration.

Without loss of generality, a single velocity expansion is used for the entire computational domain, i.e. only one "finite" element is exploited. In this way, coupling-problems at element boundaries are avoided and the main emphasis is on satisfying the boundary conditions at the dynamic free interface. If more complex geometries are examined, more elements can in principle be used with the elements not in close proximity to the interface described by e.g. FEM type methods. All additional elements are then stationary while the interface is moving. The method presented in this thesis could be used for the elements near the interface for accurately and conveniently imposing the interfacial stresses.

Since no iteration is used, and since the driving forces are transparently accounted for via the contour integrals and the tangential stress condition, the present method is believed to facilitate the understanding of the effects of the Marangoni force on the flow.

1.5 Outline of the new experiments

The main reason for performing new experiments is to accurately measure the temperature gradient along the interface while simultaneously visualizing the Marangoni flow. In the literature, several experiments on Marangoni convection are reported. Destillocapillary convection has been investigated often, [11][12][13][14][15][16], but these experiments lack information on the driving surface tension gradient at the interface since the concentration gradient along an interface is difficult to measure. In the case of thermocapillary convection some attempts were made to measure the established temperature gradient. However, the temperature gradient was mostly not really quantified [27][28] or was measured at a solid-liquid interface and not at the free liquid-gas interface. Some investigators used thermocouples to measure the temperature gradient along the gas-liquid interface [2][7]. However, the thermocouples disturb the interface and results are not reliable. In the experimental approach utilized in this thesis the temperature gradient along the gas-liquid interface is measured accurately using a non-intrusive thermovision system. This system detects the infrared light emitted from positions at the interface as a measure for the local temperature. The interface is not disturbed. The dependence of the surface tension σ on the temperature T is derived prior to the experiment. For the liquids used in this thesis the gradient $d\sigma/dT$ is negative, which means that the driving force generates motion from warm to cold areas along the interface, see [29]. Flows are visualized and measured from aside by a video-recording system.

The temperature at various positions of the interface and velocity field in the liquid are measured simultaneously to ensure that the driving condition is known and that the corresponding flow pattern is observed.

The experiments are performed for two configurations:

- A thin layer heated from above using a straight radiating canthal wire
- A hemispherical droplet cooled from below by means of a Peltier-element.

Many experiments described in the literature have been performed under microgravity conditions, this to avoid the influence of gravity [2][4][5][7][10][11][28]. Flexibility in performing experiments in microgravity is not high due to lack of space and time. For space-lab missions voluminous equipment cannot be used, since often experiments are piggy-back experiments. Furthermore, in drop towers [4][28] the observation time at microgravity conditions is limited, apart from the difficulty to build up a suitable set-up. Experiments on earth do not have these drawbacks. The equipment used for the experiments described in this thesis are easily adapted and directly controllable. Also conditions of the air (e.g. temperature and humidity) or main process and equipment parameters (e.g. temperature of the liquid and the thickness of the liquid layer) are readily varied. By cooling from outside the surface tension gradient in the vessel is regulated and a nearly stationary situation is feasible.

In the experiments at 1-g conditions described in this thesis buoyancy effects are minimal since the hotter liquid lies on top. The liquid composition is varied to investigate the effect of different liquid properties on the thickness of the layer where, near the interface, Marangoni convection is observed.

1.6 Contents of the thesis

In this thesis a model is presented based on a new method to describe thermocapillary convection for free gas-liquid interfaces with interfacial stress conditions. The method is introduced, and first applied to a thin liquid layer in a rectangular cavity in chapter 2. It is applied to a small droplet on a flat plate in chapter 5. Alternative expansions for the velocity field in and the interface of the thin liquid layer are discussed in chapter 3. The measurements performed to produce data for the validation of the numerical simulation of the flow in a liquid layer are described in chapter 4, and those for the droplet in chapter 6. Numerical simulation of these two cases is presented in chapter 7. Concluding remarks and suggestions for future research are given in chapter 8.

Chapter 2

A spectral collocation method for a dynamically changing interface and Marangoni convection in a liquid layer

2.1 Introduction

The algorithm described in this chapter is based on a method in which the pressure is eliminated by using contour integrals of the momentum equations. In this chapter this new numerical method will be applied to a thin liquid layer in a cavity with a free interface, see also [30].

This geometry is chosen to enable the prediction of flows for several applications. For example, for the drying of silicon wafers, see section 1.2, a thin layer of water is contracted through a Marangoni flow. Furthermore, this geometry can be used for studying the spreading effect of surfactants on a thin liquid film as occurs in the pulmonary airways and alveoli. Here surfactants are of great importance in the functioning of the lung system [13][16][14]. The liquid film serves as a barrier between the air and the wall of the airways and as protection against airborne particles or aerosols. Diseases like asthma, pulmonary infections and hyaline membrane disease occurring in premature neonates can be treated by inhaling an aerosol spray which thins the layer by local reduction of the surface tension.

In section 2.2 the cavity problem is introduced. First the problem statement is described in section 2.2.1, then the physical model is introduced in section 2.2.2 and this section ends with the governing equations in section 2.2.3. The numerical method is described in section 2.3. The expansions of the velocity and the interface height are presented in section 2.3.1, the contour integrals in section 2.3.2, the tangential stress condition in section 2.3.3, the adapted SVD method used to satisfy the equations resulting from the contour integrals and the tangential stress condition in section 2.3.4 and the computation of the interface deformation in section 2.3.5. Section 2.4 discusses the results of a number of applications. A constructed test case with analytical solution is considered in section 2.4.1. Flows due to prescribed surface tension histories are described in section 2.4.2.

2.2 The cavity problem

2.2.1 Problem statement

The geometry considered is a cross-section of a rectangular cavity with a liquid layer at the bottom. A surface tension gradient at the interface can be established, for example, by a wire radiating heat from above on the layer, see chapter 4. Applications of this geometry are given in chapter 1 and section 2.1. The half length of the cavity, L, is typically 40 mm, whereas the initially constant thickness of the

liquid layer, h_0^*, is typically 0.5 mm. In this chapter, for the coordinates x and y, the height of the interface h^*, the velocity in x-direction u, the velocity in y-direction v, the time t, the pressure p and the gravity g the starred quantities are dimensional and plain ones are dimensionless. The length of the cavity L, the viscosity μ, the mass density ρ and surface tension σ are only used in dimensional form and are written without star.

2.2.2 Physical model

It is assumed that the flow is two-dimensional in the (x,y)-plane, see Fig. 2.1. Because of symmetry,

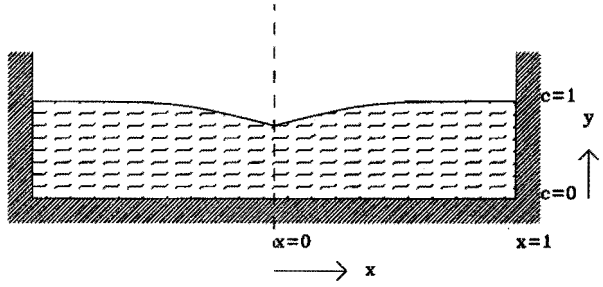

Figure 2.1: Schematic of the configuration.

only the right half of the cavity has to be considered.

At the bottom ($y = 0$) and at the right wall ($x = 1$) the conditions of no-slip ($u = 0$ at $y = 0$ and $v = 0$ at $x = 1$) and no-penetration ($v = 0$ at $y = 0$ and $u = 0$ at $x = 1$) are satisfied. This implies that $h = 1$ at $x = 1$. The assumptions of the physical model are:

1. The flow is two-dimensional, effects due to turbulence are neglected;
2. The surface tension gradient is known at all times and positions along the interface;
3. Matter at the interface has the same properties as matter in the liquid;
4. The liquid has constant physical properties, i.e. the mass density ρ and the dynamic viscosity μ_{li} are constant;
5. The liquid is incompressible and Newtonian;
6. The dynamic viscosity, μ_g, of the gas-phase is negligible compared to the dynamic viscosity μ_{li} of the liquid-phase.

2.2.3 Governing equations

The continuity equation for an incompressible fluid is:

$$\frac{\partial u^*}{\partial x^*} + \frac{\partial v^*}{\partial y^*} = 0 \tag{2.1}$$

The Navier-Stokes equations describe the diffusion of velocity in the liquid layer. The components of the Navier-Stokes equation in x-direction and y-direction can be arranged as:

$$\frac{\partial p^*}{\partial x^*} = \mu \left(\frac{\partial^2 u^*}{\partial x^{*2}} + \frac{\partial^2 u^*}{\partial y^{*2}} \right) - \rho \left(\frac{\partial u^*}{\partial t^*} + u^* \frac{\partial u^*}{\partial x^*} + v^* \frac{\partial u^*}{\partial y^*} \right) \tag{2.2}$$

$$\frac{\partial p^*}{\partial y^*} = \mu\left(\frac{\partial^2 v^*}{\partial x^{*2}} + \frac{\partial^2 v^*}{\partial y^{*2}}\right) - \rho\left(\frac{\partial v^*}{\partial t^*} + u^*\frac{\partial v^*}{\partial x^*} + v^*\frac{\partial v^*}{\partial y^*}\right) + \rho g^* \tag{2.3}$$

The tangential stress condition at the interface is a balance between the viscous shear and the surface tension gradient and reads:

$$\mu\left(1 - \left(\frac{\partial h^*}{\partial x^*}\right)^2\right)\left(\frac{\partial u^*}{\partial y^*} + \frac{\partial v^*}{\partial x^*}\right) + 4\mu\frac{\partial h^*}{\partial x^*}\frac{\partial v^*}{\partial y^*} = \left(1 + \left(\frac{\partial h^*}{\partial x^*}\right)^2\right)^{1/2}\left(\frac{\partial \sigma}{\partial x^*}\right) \tag{2.4}$$

The tangential stress condition is the driving force of the Marangoni convection. This equation therefore plays a dominant role in the present study. The normal stress condition at the interface, $(y = h)$, is a relation for the pressure drop over the interface:

$$p^* = p_0^* - 2\mu\left(\frac{1 - (\frac{\partial h^*}{\partial x^*})^2}{1 + (\frac{\partial h^*}{\partial x^*})^2}\right)\frac{\partial u^*}{\partial x^*} - 2\mu\frac{\frac{\partial h^*}{\partial x^*}}{1 + (\frac{\partial h^*}{\partial x^*})^2}\left(\frac{\partial u^*}{\partial y^*} + \frac{\partial v^*}{\partial x^*}\right) - \sigma\left(\frac{\frac{\partial^2 h^*}{\partial x^{*2}}}{\left(1 + (\frac{\partial h^*}{\partial x^*})^2\right)^{3/2}}\right) \tag{2.5}$$

with p^* the pressure in the liquid and p_0^* the pressure of the air. Eq. (2.5) is reduced by substituting $(\partial u^*/\partial y^* + \partial v^*/\partial x^*)$ obtained from Eq. (2.4) in Eq. (2.5), resulting in:

$$p^* = p_0^* - 2\mu\left(\frac{1 + (\frac{\partial h^*}{\partial x^*})^2}{1 - (\frac{\partial h^*}{\partial x^*})^2}\right)\frac{\partial u^*}{\partial x^*} - 2\left(\frac{\frac{\partial h^*}{\partial x^*}}{\left(1 - (\frac{\partial h^*}{\partial x^*})^2\right)\left(1 + (\frac{\partial h^*}{\partial x^*})^2\right)^{1/2}}\right)\frac{\partial \sigma}{\partial x^*} - \sigma\left(\frac{\frac{\partial^2 h^*}{\partial x^{*2}}}{\left(1 + (\frac{\partial h^*}{\partial x^*})^2\right)^{3/2}}\right) \tag{2.6}$$

The time evolution of the interface is obtained by using the kinematic boundary condition:

$$\frac{\partial h^*}{\partial t^*} - v^* + u^*\frac{\partial h^*}{\partial x^*} = 0 \tag{2.7}$$

where u^* and v^* are to be evaluated at the free interface. This boundary condition states that the normal component of the velocity of the liquid at the interface has to be equal to the normal component of the velocity of the interface, this because of the absence of mass transport through the interface.

Since the surface tension gradient is prescribed as a function of position and time the energy equation nor diffusion of concentration are considered.

The governing equations are made dimensionless so that all important quantities can be taken into account without loss of accuracy. The dimensionless coordinates in x- and y-direction are defined as $x = x^*/L$ and $y = y^*/h_0^*$, respectively. In case v^* is small and the interface remains almost planar $(\partial h^*/\partial x^* \approx 0)$ the tangential stress condition can be approximated by $\mu\partial u^*/\partial y^* = \partial\sigma/\partial x^* +$ h.o.t.. It then follows that the characteristic velocity in x-direction is $\Delta\sigma\ h_0^*/(L\ \mu)$. Here $\Delta\sigma$ is the characteristic spreading parameter, analogously defined as by Gaver et al. [13]. For destillocapillary flows $\Delta\sigma$ is typically the difference in surface tension between water and ethanol at 20°C ($\Delta\sigma = \sigma_{water,air} - \sigma_{ethanol,air} = 49.5 \times 10^{-3}$ N/m). The dynamic viscosity of the liquid μ_{li} [1], is taken to be that of water (1.002×10^{-3} Pa s). From Eq. (2.1) with $x = x^*/L$ and $y = y^*/h_0^*$ it follows that $v = v^*\ \mu\ L^2/\left(\Delta\sigma\ h_0^{*2}\right)$. The characteristic time is $t^* = L/u^*$, with u^* the velocity due to tangential

[1] μ_{li} is in other parts of this thesis abbreviated as μ.

surface tension gradient at the interface, so $t = t^* \, \Delta\sigma \, h_0^* / (\mu \, L^2)$. The pressure has order of magnitude $\Delta\sigma / h_0^*$, so $p = p^* \, h_0^* / \Delta\sigma$. The gravity is made dimensionless as $g = g^* \, \mu^2 \, L^4 / \left((\Delta\sigma)^2 \, h_0^{*3} \right)$. The Reynolds number, Re, based on the horizontal velocity component and h_0^*, is defined with the aspect ratio $A = h_0^* / L$ (1/80 typically) and ρ the mass density of water (998 kg/m^3) by $Re = \Delta\sigma \, A \, h_0^* \, \rho / \mu^2$. Typical values are $Re = 300 - 3000$. S_x and S_{gr} are dimensionless quantities related to the surface tension gradient and the surface tension, respectively, which follow from Eqs. 2.4 and 2.5. In Eq. (2.8) the relations are given.

$$\begin{array}{rclrclrcl} u & = & \frac{u^* \mu L}{\Delta\sigma h_0^*} & v & = & \frac{v^* \mu L}{\Delta\sigma h_0^* A} & & & \\ t & = & \frac{t^* \Delta\sigma h_0^*}{\mu L^2} & p & = & \frac{p^* h_0^*}{\Delta\sigma} & g & = & \frac{h_0^{*2} \rho g^*}{\Delta\sigma} \\ Re & = & \frac{\Delta\sigma A h_0^* \rho}{\mu^2} & S_x & = & L \frac{\frac{\partial\sigma}{\partial x^*}}{\Delta\sigma} & S_{gr} & = & \frac{\sigma_{water}}{\Delta\sigma} \end{array} \tag{2.8}$$

The Navier-Stokes equations used in the present method have the following dimensionless form:

$$ReA \left(\frac{\partial u}{\partial t} + u \frac{\partial u}{\partial x} + v \frac{\partial u}{\partial y} \right) = -\frac{\partial p}{\partial x} + \frac{\partial^2 u}{\partial y^2} + A^2 \frac{\partial^2 u}{\partial x^2} \tag{2.9}$$

$$ReA^3 \left(\frac{\partial v}{\partial t} + u \frac{\partial v}{\partial x} + v \frac{\partial v}{\partial y} \right) = -\frac{\partial p}{\partial y} + A^2 \left(\frac{\partial^2 v}{\partial y^2} + A^2 \frac{\partial^2 v}{\partial x^2} \right) + g \tag{2.10}$$

The dimensionless form of the tangential stress condition is:

$$\left(1 - D^2\right) \left(\frac{\partial u}{\partial y} + A^2 \frac{\partial v}{\partial x} \right) + 4AD \frac{\partial v}{\partial y} = \left(1 + D^2\right) S_x \tag{2.11}$$

where:

$$D \equiv A \frac{\partial h}{\partial x} \tag{2.12}$$

In approximate form ($A \to 0$) this relation reads $\partial u / \partial y = ((1 + D^2)/(1 - D^2)) \, S_x$, so diffusion of the velocity component in x-direction depends on the gradient of the surface tension.

The normal stress condition in dimensionless form is:

$$\Delta p = -A^2 \left(\frac{S_{gr} \frac{\partial^2 h}{\partial x^2}}{N^3} + \frac{2N^2 \frac{\partial u}{\partial x}}{1 - D^2} + \frac{2 S_x \frac{\partial h}{\partial x}}{1 - D^2} \right) \tag{2.13}$$

where: $\Delta p = p - p_0$ and

$$N \equiv \left(1 + D^2\right)^{1/2} \tag{2.14}$$

The first term on the right-hand side of Eq. (2.13) contains the curvature of the interface. The surface tension S_{gr} dampens interfacial deformation, the gradient in the surface tension S_x sets the liquid into motion.

The kinematic boundary condition in dimensionless form is:

$$\frac{\partial h}{\partial t} = v - u \frac{\partial h}{\partial x} \tag{2.15}$$

2.3 Numerical method

The algorithm is based on a spectral point collocation method. In this method, the solution u, is approximated by a truncated finite sum of functions, see section 2.3.1. The velocity component u is determined by the set of equations imposed at a set of collocation points. In y-direction a moving grid of collocation points is given by $c_i = y_i^*/h^*(x,t)$ for $i = 1 \ldots n_k$, with $h^*(x,t)$ the height at the interface at different times, see Fig. 2.1. In section 2.3.1 also the expansion of the free interface is given. Contour integrals, introduced in section 2.3.2, together with the tangential stress condition at the interface, as described in section 2.3.3, yield the system of equations of the numerical method. These equations are weighted and solved by an adapted SVD method, described in section 2.3.4. A closed solution is obtained. The computation of the interface deformation is described in section 2.3.5.

2.3.1 Expansions

In this section the expansions used for the cavity problem are described. Alternative expansions for this problem are considered in chapter 3. For other applications, for example a droplet condensing on a plate, different expansion are needed, see chapter 6.

The dimensionless component of the velocity in x-direction is expressed as [2]:

$$u(x,y,t) = \sum_{i=0}^{n_{ic}-1} \sum_{k=0}^{n_{kc}-1} d_{i,k} \sin(\pi(k+1)x) \left(\frac{y}{h}\right)^{i+1} \tag{2.16}$$

with n_{kc} the highest mode of the Fourier-expansion and n_{ic} the highest power of the polynomial-expansion. For constant relative height $c = y/h$, a Fourier-series is selected since roll-cells like those occurring in Bénard-cells [31][32] are expected to develop. For the y-direction a polynomial is chosen in order to increase the convergence speed and since the motion is not restricted to small areas near the interface. The $d_{i,k}$-coefficients are taken time-dependent to enable the prediction of the time evolution of the Marangoni flow. The choice of the velocity expansion satisfies the condition of symmetry with respect to the line $x = 0$, the no-slip condition at the bottom $y = 0$, and the no-penetration condition at $x = 1$. The dimensionless velocity in y-direction, v, is derived from the continuity equation upon substitution of Eq. (2.16) and subsequent integration from $y = 0$ where $v = 0$ (no-penetration condition) to y:

$$v(x,y,t) = \sum_{i=0}^{n_{ic}-1} \sum_{k=0}^{n_{kc}-1} d_{i,k} \sin(\pi(k+1)x) \frac{i+1}{i+2} \frac{\partial h}{\partial x} \left(\frac{y}{h}\right)^{i+2} \tag{2.17}$$

$$- \sum_{i=0}^{n_{ic}-1} \sum_{k=0}^{n_{kc}-1} d_{i,k} \cos(\pi(k+1)x) \frac{\pi(k+1)}{i+2} h \left(\frac{y}{h}\right)^{i+2} \tag{2.18}$$

To satisfy also the no-slip condition $v = 0$ at $x = 1$ it follows that:

$$d_{i,n_{kc}-1} = \frac{1}{n_{kc}} \sum_{k=0}^{n_{kc}-2} (k+1)\, d_{i,k} (-1)^{n_{kc}+k} \quad \text{for } i = 0 \ldots (n_{ic}-1) \tag{2.19}$$

i.e., the last coefficient, $d_{i,n_{kc}-1}$ is determined once the others have been calculated. (2.19) is added to the set of equations resulting from the discretization of the governing equations and is solved simultaneously.

For the position of the free interface, h, the following expansion is employed:

$$h(x,t) = 1 + \sum_{m=1}^{n_b} b_m \cos(\pi m x) \tag{2.20}$$

with n_b the number of time-dependent b_m-coefficients.

[2] $u(x,y,t)$, $v(x,y,t)$ and $h(x,t)$ are in other parts of this thesis abbreviated as u, v and h respectively.

2.3.2 Contour integrals

The spatial discretization of the flow field is chosen equidistant in x and c-direction, so that the resolution is everywhere the same. The grid points are the collocation points, see Fig. 2.2. The division in the y-direction adapts automatically to the time-dependent position of the interface since constant values of $c = y/h$ are used. In x-direction there are n_k collocation points, in c-direction n_i collocation points are chosen.

For each collocation point a contour integral of the pressure is calculated. A contour starts at a collocation point, first moves to the right to the nearest collocation point, then proceeds at constant x-value to the interface, then crosses the interface into the gas, turns left to a position above the collocation point where the contour was started, again crosses the interface into the fluid and finally closes at the collocation point where is started, see Fig. 2.2. The pressure drop over a closed contour

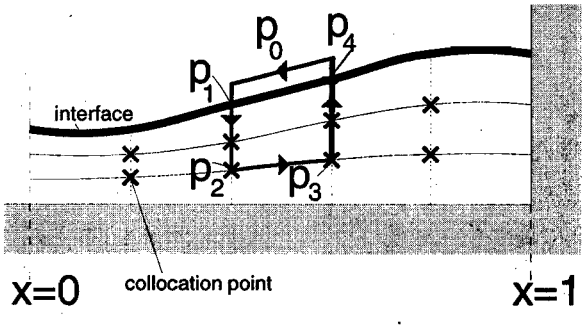

Figure 2.2: Schematic of closed contour integral.

is zero, so:

$$(p_0 - p_1) + (p_1 - p_2) + (p_2 - p_3) + (p_3 - p_4) + (p_4 - p_0) = 0 \tag{2.21}$$

For $(p_1 - p_2)$, $(p_2 - p_3)$ and $(p_3 - p_4)$ the following expressions are used:

$$(p_1 - p_2) = \int_{y=c_i h}^{y=h} \left(\frac{\partial p}{\partial y}\right)_{x=x_i} dy \tag{2.22}$$

$$(p_2 - p_3) = \int_{x=x_{i+1}}^{x=x_i} \left(\frac{\partial p}{\partial x} + c_i \frac{\partial h}{\partial x}\frac{\partial p}{\partial y}\right)_{y=c_i h} dx \tag{2.23}$$

$$(p_3 - p_4) = \int_{y=h}^{y=c_i h} \left(\frac{\partial p}{\partial y}\right)_{x=x_{i+1}} dy \tag{2.24}$$

The term $\partial p/\partial x + c_i\ \partial h/\partial x\ \partial p/\partial y$ is the variation of the pressure along the grid line $y = c_i h$. The components of the pressure gradients, $\partial p/\partial x$ and $\partial p/\partial y$, follow from Eqs. (2.9) and (2.10) as:

$$\frac{\partial p}{\partial x} = \frac{\partial^2 u}{\partial y^2} + A^2 \frac{\partial^2 u}{\partial x^2} - Re\ A \left(\frac{\partial u}{\partial t} + u \frac{\partial u}{\partial x} + v \frac{\partial u}{\partial y}\right) \tag{2.25}$$

$$\frac{\partial p}{\partial y} = A^2 \left(\frac{\partial^2 v}{\partial y^2} + A^2 \frac{\partial^2 v}{\partial x^2} - Re\ A \left(\frac{\partial v}{\partial t} + u \frac{\partial v}{\partial x} + v \frac{\partial v}{\partial y} \right) \right) + g \tag{2.26}$$

The normal stress condition, Eq. (2.13), is used for $(p_0 - p_1)$ and $(p_4 - p_0)$. Rewriting this equation for $p_4 - p_0$ yields:

$$p_4 - p_0 = -A^2 \left(\frac{S_{gr} \frac{\partial^2 h}{\partial x^2}}{N^3} + \frac{2N^2 \frac{\partial u}{\partial x}}{1 - D^2} + \frac{2S_x \frac{\partial h}{\partial x}}{1 - D^2} \right) \tag{2.27}$$

The pressure contour integrals consist of among other things the velocity terms $\partial u/\partial t$ and $\partial v/\partial t$, which upon discretization contain the time-derivatives of the $d_{i,k}$-coefficients, the so-called $e_{i,k}$-coefficients. These coefficients describe the evolution of the velocity field. [3]

A matrix equation is formed by the many (10,000 typically) contour integrals using Eq. (2.21) with the e-vector consisting of the $e_{i,k}$-coefficients:

$$\underline{\underline{B}}'\, e = \underline{w} \tag{2.28}$$

For clarity, in this and next sections the matrices are denoted by $\underline{\underline{\ }}$ and the vectors have subscript $\underline{\ }$. The vectors, d and e, do not have a subscript.

2.3.3 Tangential stress condition

The tangential stress condition at the interface is given by Eq. (2.11), i.e.:

$$\left(1 - D^2\right) \left(\frac{\partial u}{\partial y} + A^2 \frac{\partial v}{\partial x} \right) + 4\ A\ D \frac{\partial v}{\partial y} = (1 + D^2)\ S_x \tag{2.29}$$

This condition is the driving force for the Marangoni flows, therefore this equation has to be considered with care. The right-hand side vector contains the prescribed gradient S_x which at the interface creates a velocity component in tangential direction. The velocity in lower layers is established due to viscous effects. This condition applied at the collocation points on the interface (typically 100) results in a set of equations in terms of the $d_{i,k}$-coefficients, given in matrix form:

$$\underline{\underline{C}} d = \underline{q} \tag{2.30}$$

2.3.4 Singular Value Decomposition

There are two sets of equations which have to be solved simultaneously, namely the equations formed by the contour integrals, Eq. (2.28), and the equations derived from the tangential stress condition at the interface, Eq. (2.30). The former consists of typically 10,000 equations for 300 unknown $d_{i,k}$-coefficients, the latter consist of typically 100 equations for the 300 unknown $e_{i,k}$-coefficients. These sets of equations are ill-conditioned, and therefore an adapted SVD technique is used to solve these sets of equations.

First the SVD technique is described and then its application in the present method is explained. More details are described in [33].

A SVD of an overdetermined matrix $\underline{\underline{D}}_{m \times n}$ with $m > n$ is a decomposition of $\underline{\underline{D}}$ into three matrices $\underline{\underline{U}}_{m \times m}$, $\underline{\underline{\Sigma}}_{m \times n}$ and $\underline{\underline{V}}_{n \times n}$ such that

$$\underline{\underline{D}} = \underline{\underline{U}}\ \underline{\underline{\Sigma}}\ \underline{\underline{V}}^T \tag{2.31}$$

[3] The $d_{i,k}$-coefficients are the elements of a $(n_{kc} \times n_{ic})$-matrix with columns $d_{i,0}, d_{i,1}, \ldots, d_{i,n_{kc}-1}$. Vector d is defined as $d = ({d_{i,0}}^T, {d_{i,1}}^T, \ldots, {d_{i,n_{kc}-1}}^T)^T$. A similar definition is used for the e-vector.

The first n columns of $\underline{\underline{U}}$ are the columns of matrix $\underline{\underline{U_1}}$ and the last $m-n$ columns of $\underline{\underline{U}}$ are the columns of matrix $\underline{\underline{U_2}}$, i.e.:

$$\begin{array}{ll} \underline{\underline{U}} = (\underline{\underline{U_1}}; \underline{\underline{U_2}}) & \underline{\underline{U_1}} = (u_1, \cdots, u_n) \quad \underline{\underline{U_2}} = (u_{n+1}, \cdots, u_m) \\ \underline{\underline{V}} = (v_1, \cdots, v_n) & \\ \underline{\underline{U}}^T \underline{\underline{U}} = \underline{\underline{I_m}} & \underline{\underline{V}}^T \underline{\underline{V}} = \underline{\underline{I_n}} \\ \underline{\underline{\Sigma}} = diag(\sigma_1, \cdots, \sigma_n) & \end{array} \tag{2.32}$$

with $\sigma_1 \geq \cdots \geq \sigma_n \geq 0$.

The columns of $\underline{\underline{U}}$ are called the left singular vectors of $\underline{\underline{D}}$, the columns of $\underline{\underline{V}}$ are the right singular vectors of $\underline{\underline{D}}$ and the diagonal elements of $\underline{\underline{\Sigma}}$ are the singular values of matrix $\underline{\underline{D}}$. The singular values of $\underline{\underline{D}}$ are the square roots of the eigenvalues of $\underline{\underline{D}}^T \underline{\underline{D}}$. Consider an arbitrary system of equations $\underline{\underline{D}}\underline{x} = \underline{b}$. A total least-squares solution of this equation is obtained by calculating the SVD of $(\underline{\underline{D}}; \underline{b})$ [4] in:

$$(\underline{\underline{D}}; \underline{b})(x^T; -1)^T = 0 \tag{2.33}$$

Define $\underline{\underline{E}} \stackrel{\text{def}}{=} (\underline{\underline{D}}; \underline{b})$. If the singular values of $\underline{\underline{E}}$ are $\sigma_1, \sigma_2, \ldots, \sigma_n, \sigma_{n+1}$ with $\sigma_1 \geq \cdots \geq \sigma_{n+1} \geq 0$ then the condition-number of the matrix $\underline{\underline{E}}$ is defined as σ_1/σ_{n+1} and is ∞ if $\sigma_{n+1} = 0$. To obtain a well conditioned problem of Eq. (2.33) the smallest singular values are set equal to zero. If the smallest i-singular values are set to zero then SVD determines the best rank $(n+1-i)$-approximation $(\underline{\underline{D_i}}'; \underline{b_i}')$ of $\underline{\underline{E}} = (\underline{\underline{D}}; \underline{b})$ in the Frobenius norm, i.e. $\|(\underline{\underline{E}} - \underline{\underline{P}})\|_F \geq \|\underline{\underline{E}} - (\underline{\underline{D_i}}'; \underline{b_i}')\|_F$ for all possible matrices $\underline{\underline{P}}$ with dimensions $m \times (n+1)$. The Frobenius norm of the matrix $\underline{\underline{D}}_{m \times n}$ is defined by $\|\underline{\underline{D}}_{m \times n}\|_F = \sqrt{\sum_{j=1}^{m} \sum_{l=1}^{n} d_{j,l}^2}$. The matrix equation $(\underline{\underline{D_i}}'; \underline{b_i}')(x^T; -1)^T = 0$ is solved using the normal method. It uses the following properties of the SVD: The left singular vectors are the eigenvectors of the matrix $\underline{\underline{E}}\underline{\underline{E}}^T$, and the right singular vectors are the eigenvectors of the matrix $\underline{\underline{E}}^T \underline{\underline{E}}$.

How the SVD technique is applied in the numerical method of this thesis is described in the following. The first step in solving the two sets of matrix equations, Eqs. (2.28) and (2.30), simultaneously is the reduction of the number of unknowns. The $e_{i,k}$-coefficients are expressed in terms of the $d_{i,k}$-coefficients using a second-order Adams-Bashford integration technique:

$$d_{ik,t+\Delta t} = \frac{1}{2} \left(3\, e_{ik,t} - e_{ik,t-\Delta t}\right) \Delta t + d_{ik,t} \tag{2.34}$$

$e_{ik,t-\Delta t}$ are the coefficients of the e-vector of previous step. Rewriting Eq. (2.34) yields:

$$e_{ik,t} = \frac{1}{3} \left(\frac{2}{\Delta t} \left(d_{ik,t+\Delta t} - d_{ik,t}\right) + e_{ik,t-\Delta t} \right) \tag{2.35}$$

Substitution of Eq. (2.35) in Eq. (2.28) results in matrix equation:

$$\underline{\underline{B}}\, d = \underline{z} \quad \text{or} \quad (\underline{\underline{B}}; \underline{z})(d^T; -1)^T = 0 \tag{2.36}$$

Now the number of unknowns is halved.

The number of rows of matrix $\underline{\underline{B}}$ is equal to the number of collocation points in the fluid. In tests described later on, 10,000 collocation points ($= n_k \times n_i$) are used for solving 300 ($= n_{kc} \times n_{ic}$) coefficients. So a matrix $\underline{\underline{B}}$ is formed with dimensions $10,000 \times 300$.

Matrix equation (2.30), containing the discretized tangential stress condition at the interface, has 100 ($= n_k$) rows and 300 $d_{i,k}$-coefficients. The adapted SVD calculates for this matrix equation the singular values in the same manner as for the system of equations resulting from the discretized contour integrals.

[4] A block-matrix is formed: vector $\underline{b}$ is added as column to the right of matrix $\underline{\underline{D}}$.

The singular values of $\underline{\underline{\tilde{C}}} \stackrel{def}{=} (\underline{\underline{C}}; \underline{q})$ and $\underline{\underline{\tilde{B}}} \stackrel{def}{=} (\underline{\underline{B}}; \underline{z})$ show a characteristic pattern, see for example Fig. 2.3 and 2.4. There is a sharp transition from significant singular values to noise related singular values. r is the number of significant singular values associated with the matrix equation of the tangential stress condition, $\underline{\underline{\tilde{C}}}$, and j is the number of significant singular values associated with the matrix equation of the contour integrals, $\underline{\underline{\tilde{B}}}$. For more details, see appendix B and [33]. Let $\underline{\underline{C'}}$ be

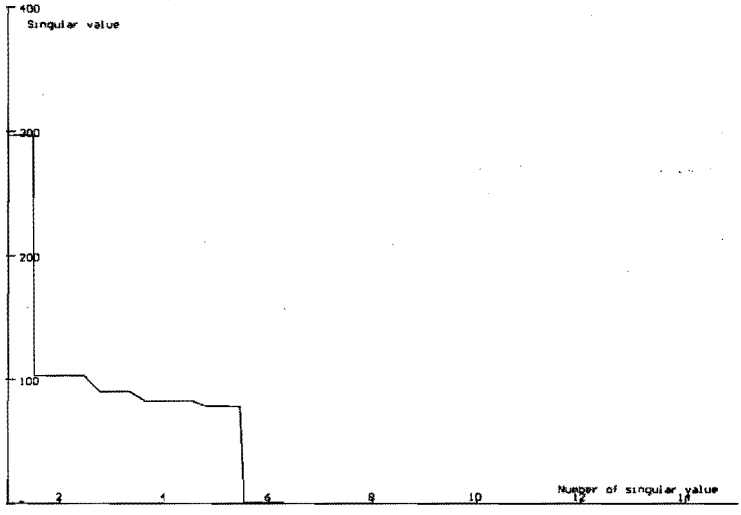

Figure 2.3: Singular values of the matrix equation from the tangential stress condition. Values used are $n_k = n_i = 15$, $n_{kc} = 6$, $n_{ic} = 3$ and $n_b = 6$.

the SVD approximation of $\underline{\underline{\tilde{C}}}$ of rank r and $\underline{\underline{B'}}$ the SVD approximation of $\underline{\underline{\tilde{B}}}$ of rank $n_{kc} \times n_{ic} - r$. The tangential stress condition is the driving force for Marangoni convection, so these equations are solved as accurate as possible.

Now is formed:

$$\begin{pmatrix} \underline{\underline{C'}} \\ \underline{\underline{B'}} \end{pmatrix} (d^T; -1)^T = 0 \tag{2.37}$$

with $\underline{\underline{C'}}$ of rank r and $\underline{\underline{B'}}$ of rank $(n_{kc} \times n_{ic} - r)$. Let $\underline{\underline{C^*}}$ be the matrix formed by the first $n_{kc} \times n_{ic}$ columns of $\underline{\underline{C'}}$ and $\underline{\underline{B^*}}$ the matrix formed by the first $n_{kc} \times n_{ic}$ columns of $\underline{\underline{B'}}$. Thus, $\underline{\underline{C'}} = (\underline{\underline{C^*}}; \underline{q^*})$ and $\underline{\underline{B'}} = (\underline{\underline{B^*}}; \underline{z^*})$. Then, the rank of $\begin{pmatrix} \underline{\underline{C^*}} \\ \underline{\underline{B^*}} \end{pmatrix}$ is $n_{kc} \times n_{ic}$ or less. In practice the rank will be $n_{kc} \times n_{ic}$ and $\begin{pmatrix} \underline{\underline{C^*}} \\ \underline{\underline{B^*}} \end{pmatrix}$ will have full rank. Now:

$$\begin{pmatrix} \underline{\underline{C^*}} \\ \underline{\underline{B^*}} \end{pmatrix} d = \begin{pmatrix} \underline{q^*} \\ \underline{z^*} \end{pmatrix} \tag{2.38}$$

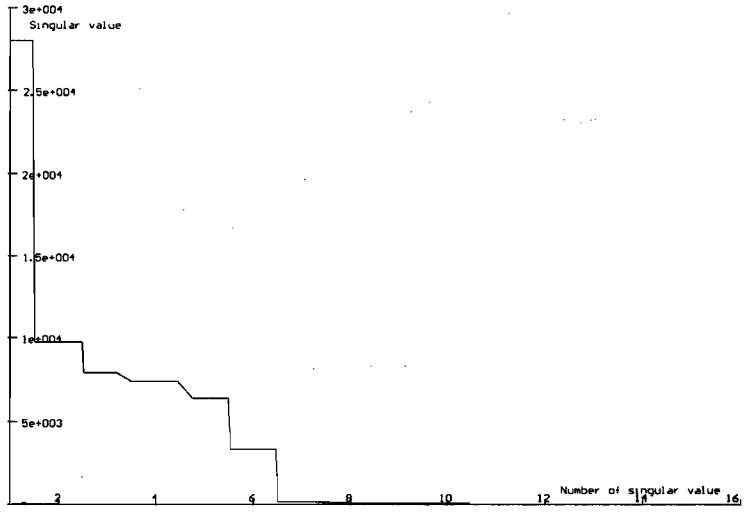

Figure 2.4: Singular values of the matrix equation resulting from the contour integrals. Values used are $n_k = n_i = 15$, $n_{kc} = 6$, $n_{ic} = 3$ and $n_b = 6$.

Eq. (2.38) has an exact solution d which is the solution of the normal equation:

$$(\underline{\underline{C^*}})^T \underline{\underline{C^*}} d + (\underline{\underline{B^*}})^T \underline{\underline{B^*}} d = (\underline{\underline{C^*}})^T \underline{q^*} + (\underline{\underline{B^*}})^T \underline{p^*} \tag{2.39}$$

Eq. (2.39) can be solved using the LU-decomposition. The advantage of this approach with known full rank matrices is that the $d_{i,k}$-values computed in this way meet almost exactly the tangential stress condition at the cost of a minimum of accuracy in the equations resulting from the contour integrals. Furthermore, the dimensions of the matrices $(\underline{\underline{C^*}})^T \underline{\underline{C^*}}$ and $(\underline{\underline{B^*}})^T \underline{\underline{B^*}}$ are small in comparison with the dimensions of the matrix $\underline{\underline{B}}$ and the calculation time is relatively short.

The solution vector contains the calculated $d_{i,k}$-coefficients. Then the velocity is known everywhere in the liquid layer at time t. The time-evolution of the velocity field is described by solving the governing equations as described above with the adapted SVD method for each time t. From the $d_{i,k}$-coefficient the b_m-coefficients are calculated, using Eq. (2.40), so the dynamic deformation of the interface is then also known.

2.3.5 Computation of interface deformation

Making use of the kinematic boundary condition, Eq. (2.15), either one of two methods for the description of the interface can be selected:

1. An analytical relation is found between the time derivative of the b_m-coefficients, db_m/dt, and the $d_{i,k}$-coefficients of the velocity expansion. This analytical relation gives db_m/dt-values dependent of an infinite orthogonal series of b_m-coefficients and a finite orthogonal series of $d_{i,k}$-coefficients:

$$\frac{db_m}{dt} = \sum_{l=1}^{n_{kc}} \sum_{k=0}^{n_{kc}-1} b_{k+l+1} \sum_{i=0}^{n_{ic}-1} \sum_{j=0}^{n_{kc}-1} \frac{d_{i,n_{kc}+j}}{i+2}$$

$$-\sum_{l=1}^{n_{kc}}\sum_{k=l-1}^{n_{kc}-1} b_{k-l+1}\sum_{i=0}^{n_{ic}-1}\sum_{j=0}^{n_{kc}-1}\frac{d_{i,n_{kc}+j}}{i+2} - \sum_{l=1}^{n_{kc}}\sum_{k=0}^{l-1} b_{l-k-1}\sum_{i=0}^{n_{ic}-1}\sum_{j=0}^{n_{kc}-1}\frac{d_{i,n_{kc}+j}}{i+2}$$
$$+\sum_{l=n_{kc}+1}^{\infty}\sum_{k=0}^{n_{kc}-1}(b_{k+l+1}-b_{l-k-1})\sum_{i=0}^{n_{ic}-1}\sum_{j=0}^{n_{kc}-1}\frac{d_{i,n_{kc}+j}}{i+2}\frac{\pi}{2l} \qquad (2.40)$$

Eq. (2.40) is an exact relation so it is given with an infinite number of b_m-coefficients. The infinite series is truncated at $3n_b$ terms to render it finite. Further db_m/dt-coefficients are usually too small to be significant. The corresponding $3n_b$ b_m-coefficients at the next time level are calculated with an Adams-Bashford integration method:

$$b_{m,t+\Delta t} = \frac{1}{2}\left(3\frac{db_{m,t}}{dt} - \frac{db_{m,t-\Delta t}}{dt}\right)\Delta t + b_{m,t} \qquad (2.41)$$

In the subsequent calculations, only n_b b_m-coefficients are used, since the interfacial height expansion uses this number of coefficients and it is accurate enough to describe the interfacial motion.

2. Using a continuous least-square fit by minimisation of g with $g = \int_0^1 \left(f - \hat{f}\right)^2 dx$ and f being the known position of the interface and $\hat{f}$ being the interface expansion, given in Eq. (2.20). f is determined using the kinematic boundary condition, Eq. (2.15), and an Adams-Bashford integration. Differentiating g with respect to x yields a system of linear equations for the unknown b_m-coefficients.

The deformation of the interface is determined by the set of coefficients b_m. In most test cases described in section 2.4 the second method is used.

The time evolution of the velocity field and the position of the interface are predicted by calculating the $d_{i,k}$-coefficients as described in section 2.3.4 and by calculating the b_m-coefficients for the next time level as described above.

2.4 Results

2.4.1 A test case with an analytical solution

Only very few analytical solutions of Marangoni convection problems can be found in the literature. In this section a special test case is constructed based on a Landau and Lifshitz [34] solution.

A heated thin liquid layer with steady motion.

A thin liquid layer is considered that rests on a horizontal plane solid surface that is non-uniformly heated. The temperature is a given function of the horizontal coordinate x. Because the layer is thin, its temperature is supposed to be independent of the vertical coordinate y, perpendicular to coordinate x. The spatially non-uniform, but timewise steady constant temperature field, corresponds to a surface tension gradient along the interface. A steady flow is then established.

The assumptions that are made to solve the analytical solution with the governing equations are given below, where differences with the assumptions underlying the computational method are indicated.

- Variation of pressure due to curvature of the surface is neglected. For the numerical solution this implies a simplification of each contour integral.

- Only the horizontal velocity component, u, and its derivatives are significant; the vertical velocity component, v, is negligible as compared to u. In the numerical solution, on the contrary, both components are included.
- The mass density, ρ, depends on x, but not on y. The dependence of ρ on x is prescribed and given below.
- The flow is steady. The numerical method computes time-dependent flows only and so a steady-flow solution should be obtained as time tends to infinity.
- At $x = 0$ symmetry is taken into account but at $x = 1$ the no-slip condition is not applied.
- $u = 0$ at $y = 0$, the no-slip condition along the bottom of the layer. The expansion of Eq. (2.16) automatically satisfies this constraint.
- At the interface, $y = h$, $\mu\ \partial u/\partial y = \partial\sigma/\partial x$, which implies a simplification of the tangential stress condition compared to the full one employed in the numerical method.

Mass density ρ^* is made dimensionless by division by ρ_0^*, so $\rho = \rho^*/\rho_0^*$. The gravitational constant g^* is 9.81 m/s^2. In the numerical method gravity must therefore be taken into account in the contour integrals. The Reynolds number, $Re = \rho_0^*\ u^*\ h_0^*/\mu$, based on the initial layer thickness, h_0^*, amounts typically to $Re = 3700$. With the above assumptions, the dimensionless interfacial height, $h = h^*/h_0^*$, with h^* the layer thickness, is governed by:

$$\frac{\rho}{3}\frac{\partial h^2}{\partial x} + \frac{h^2}{4}\frac{\partial \rho}{\partial x} = \frac{\Delta\sigma}{\rho_0^*\ g^*\ h_0^{*2}}\ S_x \tag{2.42}$$

as was analytically demonstrated by Landau and Lifshitz [34]. The constant $\Delta\sigma$ is a typical surface tension difference due to temperature differences (49.5×10^{-3} N/m) and the constant ρ_0^* is the mass density of water at 293 K (998 kg/m^3). The value of $\Delta\sigma$ is chosen similar as in section 2.2.

Because h is expanded in a Fourier series in the numerical method, see Eq. (2.20), $\partial h/\partial x$ is easily derived. It is convenient to expand both ρ and S_x in a similar fashion to be able to satisfy Eq. (2.42) exactly. The following expansions are selected:

$$\rho = \frac{1}{\left(\sum_{k=1}^{n_{kc}} b_k\ \cos(\pi k x)\right)^2} \tag{2.43}$$

$$S_x = -\frac{\rho_0^*\ g^*\ h_0^{*2}}{6\ \Delta\sigma^*}\frac{\sum_{k=1}^{n_{kc}} \pi\ k\ b_k\ \sin(\pi k x)}{\sum_{l=1}^{n_{kc}} b_l\ \cos(\pi l x)} \tag{2.44}$$

It is easily seen that with these choices of h, ρ, and S_x, Eq. (2.42) is satisfied exactly.

The dimensionless velocity component, u, as a function of h, ρ, and S_x follows analytically [34] from:

$$u(x,y) = \frac{\rho_0^*\ g^*\ h_0^{*2}}{\Delta\sigma}\left[\left(\frac{1}{2}\ y^2 - y\ h\right)\frac{\partial(\rho\ h)}{\partial x} + \left(\frac{1}{2}\ y\ h^2 - \frac{1}{6}\ y^3\right)\frac{\partial \rho}{\partial x}\right] + y\ S_x \tag{2.45}$$

By the choice of $\rho(x)$ and $S_x(x)$, i.e. Eqs. (2.43) and (2.44), Eq. (2.45) is satisfied for arbitrary n_{kc} by selecting:

$$\begin{aligned} u(x,y) = & -\frac{\rho_0^*\ g^*\ h_0^{*2}}{6\ \Delta\sigma}\sum_{k=0}^{n_{kc}-1} \pi\ (k+1)\ b_{k+1}\ \sin(\pi\ (k+1)\ x)\left(\frac{y}{h}\right) \\ & +\frac{\rho_0^*\ g^*\ h_0^{*2}}{2\ \Delta\sigma}\sum_{k=0}^{n_{kc}-1} \pi\ (k+1)\ b_{k+1}\ \sin(\pi\ (k+1)\ x)\left(\frac{y}{h}\right)^2 \\ & -\frac{\rho_0^*\ g^*\ h_0^{*2}}{3\ \Delta\sigma}\sum_{k=0}^{n_{kc}-1} \pi\ (k+1)\ b_{k+1}\ \sin(\pi\ (k+1)\ x)\left(\frac{y}{h}\right)^3 \end{aligned} \tag{2.46}$$

Note that this velocity field is in the form of the expansion used in the numerical method, Eq. (2.16). For each value of n_{kc} a representation of the exact solution is therefore feasible. The analytical solution for the $d_{i,k}$-coefficients is easily found by equating Eq. (2.16) to Eq. (2.46). This yields for $n_{ic} = 3$:

$$d_{i,k} = \frac{\rho_0^* \, g^* \, h_0^{*2} \, \pi}{6 \, \Delta\sigma} \begin{pmatrix} -b_1 & -2b_2 & \dots \\ 3b_1 & 6b_2 & \dots \\ -2b_1 & -4b_2 & \dots \end{pmatrix} \tag{2.47}$$

The number of rows is n_{ic} and the number of columns is $n_b = n_{kc}$, with n_b an arbitrary integer. The b_i-coefficients are the interface coefficients of Eq. (2.20) and are analytically calculated from the $d_{i,k}$-coefficient using Eq. (2.40).

Numerical values of $d_{i,k}$ have been obtained for $n_k = n_i = 100$, $n_{kc} = n_b = 5$, and $n_{ic} = 3$. The computed values of the ratios $d_{i,n_{kc}+k}/d_{i+1,n_{kc}+k}$ are exactly the values predicted by Eq. (2.47). The computed flow field is steady, as it should.

In Fig. 2.5 three plots are given of the computed velocity field for $n_b = 5$. Plot 1 gives the dimensionless and plot 2 the dimensional velocities in the scaled geometry. Plot 3 gives the dimensional velocities in a non-scaled geometry. A strong roll-cell is established in the dimensionless plot which suggests a large vertical velocity component. In the dimensional plot it is shown that there is only a small vertical velocity component. This is in agreement with the assumption that the vertical velocity component is relatively small compared to the horizontal velocity component. The interface is hardly deformed, as is assumed in the analytical solution.

The calculations are always performed in dimensionless coordinates (see plot 1) to maintain the accuracy.

2.4.2 Flow caused by prescribed surface tension histories

A geometry as described in section 2.2 is considered with initially the interface and liquid at rest. The following velocity expansion is selected:

$$u(x,y,t) = \sum_{i=0}^{n_l} \sum_{k=0}^{n_{kc}-1} d_{i,k} \sin(\pi(k+1)x) \left(\frac{y}{h}\right) e^{(\lambda_i(\frac{y}{h}-1))} + \sum_{i=n_l+1}^{n_{ic}-1} \sum_{k=0}^{n_{kc}-1} d_{i,k} \sin(\pi(k+1)x) \left(\frac{y}{h}\right)^{i+1} \tag{2.48}$$

with λ_i given positive constants. The exponential terms are introduced in order to satisfy the tangential stress condition in early stages when the flow is limited to a small region in the vicinity of the interface. Usually $n_l = 1$ or 2 suffices to describe this flow feature. Note that $u(x,0,t) = 0$ for all values of n_l, n_{kc} and n_{ic}. The interface is described with Eq. (2.20). Two surface tension distribution histories are prescribed:

1. The distribution shown in Fig. 2.6. This case represents the case that ethanol is absorbed in the water near $x = 0$ for some finite time.

2. This test case is a sudden increase of the surface tension gradient at a number of places along the interface.

The details are given in appendix C.

Table 2.1 lists the basic parameters used for the calculations. In all other tests to be described these parameters are the same unless noted otherwise. The first test case to be considered has been performed with the parameters of table 2.1 in a shallow cavity with $h_0^* = 0.5$ mm. The surface tension gradient of profile 1 is prescribed with S_x constant from $t = 0.35$ on, when the maximum of S_x is reached. In Fig. 2.7 plots are shown of the solutions at times $t = 0.05, 0.10, 0.20$, and 0.30. When

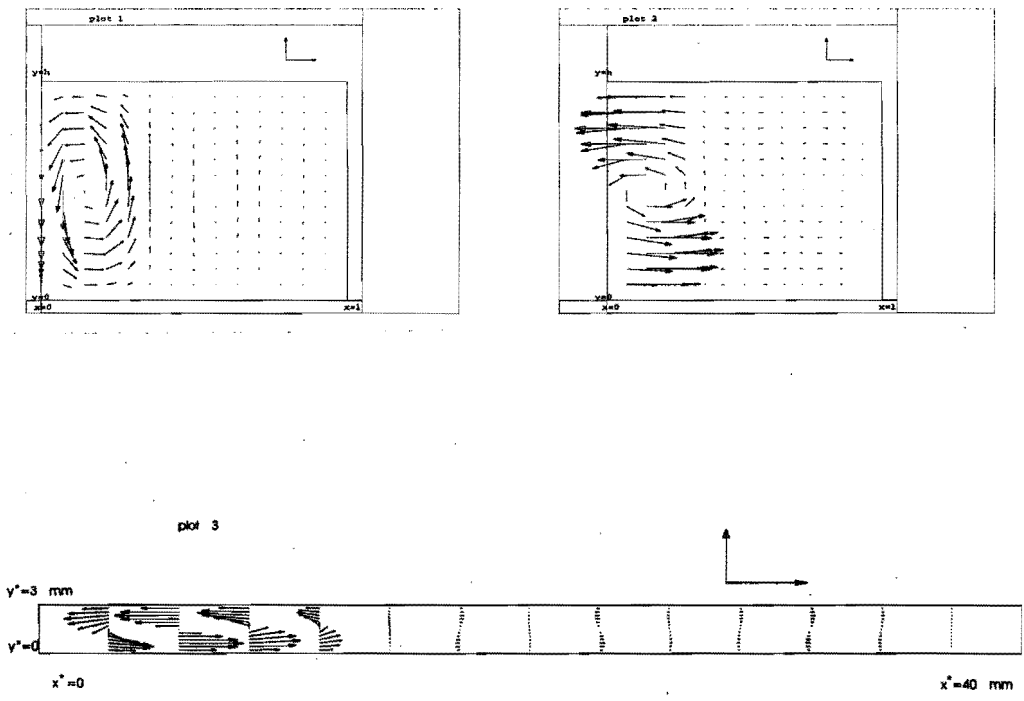

Figure 2.5: The dimensionless (plot 1) and dimensional (plot 2) velocity field in the heated thin water layer with steady motion governed by Eq. (2.46); $g^* = 9.81$ m/s^2. The reference arrow of the velocity component in x-direction has the value 1.85×10^{-4} m/s in plots 1 and 2, the reference arrow of the velocity component in y-direction has the value 1.40×10^{-5} m/s. The reference arrow of the velocity component in x-direction of plot 3 has the value 1.23×10^{-3} m/s, the one in y-direction has the value 9.33×10^{-5} m/s. The geometry in plot 3 is not scaled.

time increases the velocity increases and a larger part of the layer is set into motion. The tangential stress at the interface due to the gradient in the surface tension is the forcing term which through the momentum equation determines the flow field evolution. Momentum is generated at the interface and forced onto the lower layers. Liquid is being transported from left to right, so the interface near $x = 0$ sinks while near $x = 0.2$ it rises, as is shown in Fig. 2.11. This figure is discussed more fully below.

The $d_{i,k}$-coefficients corresponding to $\sin(\pi\ x)$, $\sin(2\ \pi\ x)$ and $\sin(3\ \pi\ x)$ largely determine the flow field. In an early stage, e.g. at $t = 0.20$, the $d_{i,2}$-terms are largest, e.g. $d_{3,2} = 2.7 \times 10^{-4}$. A shift is seen at later times, e.g. at $t = 0.60$, when the $d_{i,0}$-terms become largest. The contribution of the higher harmonics is then less important, f.e. $d_{3,8} = 6.4 \times 10^{-5}$ (relatively 24% of $d_{3,2}$). If the exponentials, the λ-terms, were omitted from the velocity expansion Eq. (2.48), accurate results could not be produced and the tangential stress condition is not well satisfied. The exponential functions describe the sharp gradient near the interface very well and account for the initial forcing of the liquid by the tangential stress induced by the gradient in the surface tension. For example, if the exponential function corresponding with λ_0 has a contribution in the component of the velocity in x-direction of

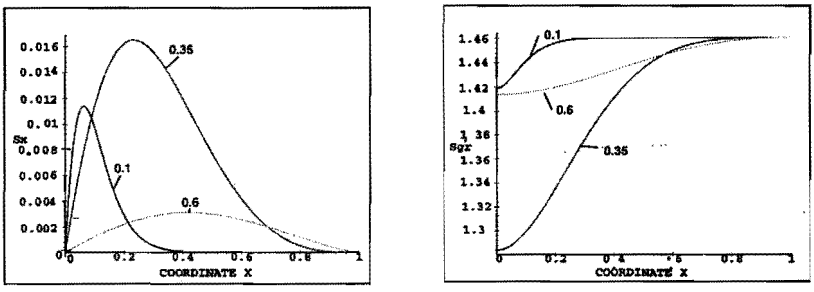

Figure 2.6: S_x and S_{gr} versus coordinate x at times $t = 0.10$ (line), $t = 0.35$ (dot-dashed) and $t = 0.60$ (dotted).

n_k	n_i	n_b	n_{kc}	n_{ic}	Δt	g	h_0^*	A	r	j	λ_0	λ_1	λ_2	μ [Pas]	#
100	100	12	10	30	0.01	0	0.5	$\frac{1}{89}$	n_{kc}	$n_{ic} \times n_{kc} - r$	100	10	3	1.002×10^{-3}	1

Table 2.1: Value of parameter set for test case 1. # means gradient profile history.

order 1 at the interface then the velocity at $c = 0.9$ is of order 10^{-4}. The gradient for the exponential function with λ_2 and λ_3 is less sharp: the velocity at $c = 0.9$ is of order 0.37 and 0.74, respectively. Unless the somewhat low value for the $d_{0,2}$-coefficient, e.g. $d_{0,2} = 7.5 \times 10^{-5}$ (relatively 28% of $d_{3,2}$), compared with those corresponding to the other exponentials, e.g. $d_{1,2} = 8.8 \times 10^{-5}$ (relatively 31% of $d_{3,2}$) and $d_{2,2} = 1.7 \times 10^{-4}$ (relatively 63% of $d_{3,2}$), only the harmonics corresponding to the λ_0-term have an essential contribution to the predicted flow field. The exponential terms corresponding to λ_1 and λ_2 have only a small contribution to the flow field. If λ_1 and λ_2 are chosen differently: $\lambda_0 = 100$, $\lambda_1 = 62$ and $\lambda_2 = 34$, the same results as before are obtained. These results show also that the larger the power of the polynomial function y/h, the smaller the value of the corresponding $d_{i,k}$-coefficient, e.g. $d_{8,2} = 1.3 \times 10^{-4}$ (relatively 48% of $d_{3,2}$). The expansion converges quite rapidly, as it should.

time	$\mu \frac{\partial u}{\partial y}$	S_x
0.01	8.0×10^{-5}	3.1×10^{-5}
0.02	5.9×10^{-4}	8.7×10^{-4}
0.05	6.3×10^{-3}	9.5×10^{-3}
0.10	2.0×10^{-2}	1.0×10^{-2}

Table 2.2: The leading term of the tangential stress compared with the prescribed surface tension gradient, S_x, at the interface at various times t.

To show the evolution of the velocity in time better, Fig. 2.8 presents the dimensionless velocity components u and v as a function of the vertical distance of the liquid for test case 1 at $x = 2/26$ for various times t. Fig. 2.9 shows the dimensional velocity field for test case 1 at $t = 0.10$ and $t = 0.40$. These plots show that the actual horizontal velocity component is larger than the vertical velocity

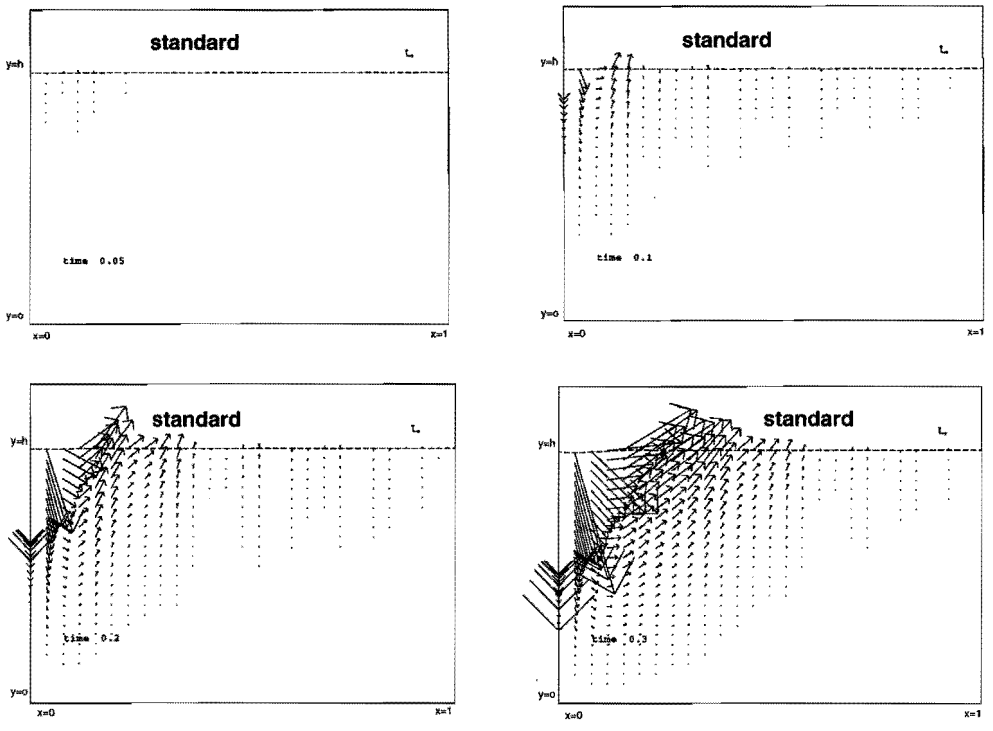

Figure 2.7: The velocity field for test case 1 (see table 2.1) at various times. Reference arrow of the velocity component in x-direction corresponds to 1.03 mm/s. Reference arrow of the velocity component in y-direction corresponds to 0.017 mm/s.

component, $u^* = 0.618\ u$ m/s while $v^* = 7.72 \times 10^{-3}\ v$ m/s. To get a view on the flow inside the thin layer, Fig. 2.10 shows the dimensional velocity in the vessel in the physical domain. This plot shows that mainly flow in x-direction is established in a thin liquid layer next to the free surface.

Quantitatively, table 2.2 shows the relation between the leading term of the tangential stress, i.e. $\tau = \mu\ \partial u/\partial y$, and the prescribed surface tension gradient, S_x, at the interface at $x = 1/26$ for small times t. It shows that the order of magnitude is correct although the absolute values differ. The reason is obvious. The diffusion term $\partial u/\partial y$ is directly proportional to the driving force S_x. The difference in absolute value is caused since $\partial v/\partial x$ and $\partial v/\partial y$ are shown in Fig. 2.7 to be in play in the tangential stress condition Eq. (2.11).

To compare the results of test case 1 quantitatively with those from the literature, typical values of the driving forces for Marangoni convection and the induced maximum velocity, u_{max}, are shown in table 2.3. Its values are based on numerical results [9], but mainly on experiments [12][29][35][36][37][38][39]. It appears that the order of magnitude of the generated velocity of test case 1 is in agreement with those found in the literature for corresponding driving forces. Moreover, for the numerical results of Lan and Sindu Kou [9] and the one of this chapter the ratio of $(u_{max})_{Lan\ and\ Sindu\ Kou}/(u_{max})_{this\ chapter}$ is approximately in agreement with the ratio of the driving forces $(\partial\sigma/\partial s)_{Lan\ and\ Sindu\ Kou}/(\partial\sigma/\partial s)_{this\ chapter}$. Small differences exist since different liquids are involved. Comparison of results from the experiments

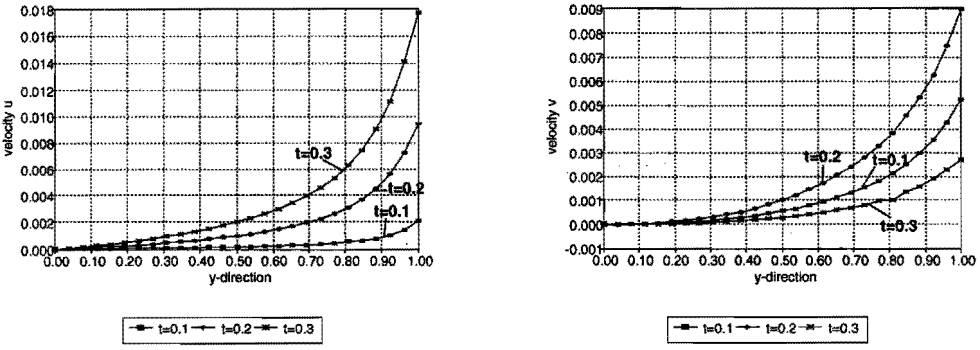

Figure 2.8: The velocities u and v as a function of the vertical distance of the liquid for test case 1 (see table 2.1) at $x = 2/26$ for various times t.

ref.	$\frac{\partial T}{\partial x}$ [°C/m]	$\frac{\partial \sigma}{\partial x}$ [N/m^2]	u_{max} [mm/s]	fluid	μ [Pas]
[9] *	580	0.58×10^{-2}	6.35	$NaNO_3$	2.82×10^{-3}
this ch. *	134	1.98×10^{-2}	13.2	water	1.002×10^{-3}
[12]	0.01M. sol.	-	12	aqueous sol. $CoCl_2$	$\pm 1.002 \times 10^{-3}$
[29]	10	-	3.0	aqueous sol. n-hept.	$\pm 1.002 \times 10^{-3}$
[35]	666	-	2.0	n-heptanol	7.0×10^{-3}
[38]	360	-	0.145	aqueous sol. 87% glyc.	$\pm 1.002 \times 10^{-3}$
ch. 4 & [39]	170	1.7×10^{-2}	1.76	n-par. $C_{10} - C_{13}$	1.43×10^{-3}
ch. 7 *	160	1.6×10^{-2}	≈ 2.0	n-par. $C_{10} - C_{13}$	1.43×10^{-3}

Table 2.3: Survey of typical Marangoni convection results from the literature. * = numerical result, M. sol = molar solution and ch = chapter.

as described in chapter 4 with results of dedicated numerical simulations, see chapter 7, show good agreement. Therefore it can be concluded that realistic results are obtained with the present computational method.

Parameter variation

The distribution of the collocation points

The number of collocation points determines the number of contour integrals of the method. An optimum must be found so that enough points are used to get accurate results while simultaneously the calculation time is acceptable. In test case 2 the number of collocation points is halved in both directions $n_k = n_i = 50$. Similar result were found as for test case 1. An appropriate number of collocation points is taken to be $n_k = n_i = 100$, since computation time is acceptable, approximately one hour per timestep of approximately 10800 [Mflop] on a SGI INDY MIPS R4400 processor at 200 [Mhz] with 3 [Mflops], and since the other parameters of table 2.1 can be varied without necessitating

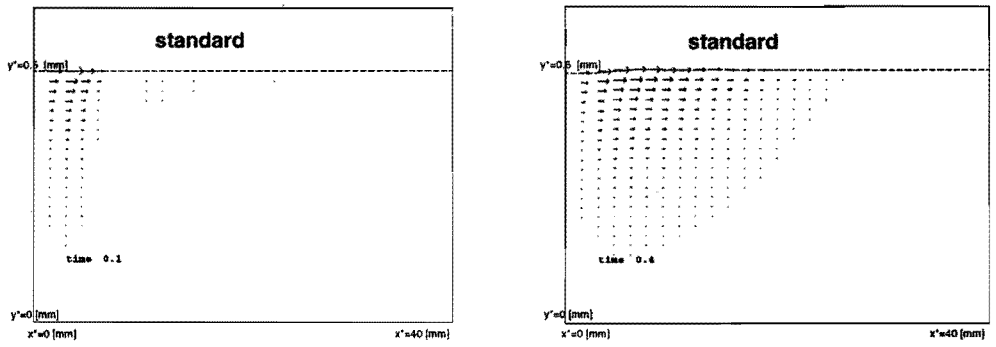

Figure 2.9: The dimensional velocity field for test case 1 (see table 2.1) with scaled configuration at time $t = 0.10$ and time $t = 0.40$ (velocities multiplied by factor 0.1).

an adaptation of n_k and n_i. Calculations are done using double-precision arithmetic according IEEE-754 standard.

The number of coefficients in the expansion of the velocity

An exact solution would in principle be possible if the number of orthogonal functions could be taken infinite and if the numerical error per coefficient would not depend on this number. In the method n_{kc}, n_{ic} and n_b have been varied to examine the dependence of the solution on these parameters.

Fig. 2.12 shows results for similar situation as test case 1 ($n_{ic} = 30$, see Fig. 2.7), but with $n_{ic} = 10$ (test case 3) and $n_{ic} = 15$ (test case 4, see table 2.6). The flow pattern is similar in all three situations considered. The velocity at the interface increases with increasing n_{ic}. The increase of n_{ic} from 15 to 30 has hardly any effect and increasing n_{ic} above 30 is not necessary. The choice of $n_{ic} = 30$ is therefore appropriate.

For n_{kc} it suffices to choose 10 for a description of the velocity field, since at $n_{kc} = 12$ (test case 5 see table 2.6) similar results are obtained, see Fig. 2.13.

It is seen that the interface behaves according to the highest harmonics of the velocity expansion since the b_m-coefficients of the interface are analytically coupled to the $d_{i,k}$-coefficients, see Eq. (2.40). With $n_{kc} = 10$ the mode of periodicity is 5, see Fig. 2.11, at $n_{kc} = 12$ the mode is 6, see Fig. 2.14. This is easily explained, since the number n_b is directly coupled to n_{kc} via the kinematic boundary condition, Eq. (2.15). For $n_b > n_{kc}$ only n_{kc}-terms of the interface are effectively used and similar results as for $n_{kc} = n_b$ are obtained, see table 2.4, in which the n_b-coefficients are given for case 1 and 6, with $n_{kc} = 10$ and $n_b = 12$ and 15, respectively. Comparison shows that increasing n_b above $n_{kc} = 10$ is of no use since the coefficients with index exceeding n_{kc} are very small compared to the first n_{kc}-coefficient. If $n_b < n_{kc}$ the interface behaves according to the value of n_b. The best choice is $n_b \geq n_{kc}$.

Aspect ratio variation

The aspect ratio, $A = h_0^*/L$, is varied from 1/80 (standard, test case 1, with $h_0^* = 0.5$ mm), 3/80 (test case 7, with $h_0^* = 1.5$ mm) and 3/40 (test case 8, with $h_0^* = 3.0$ mm). $L = 0.04$ m and also the driving force is equal in all three cases. The other parameters are given in table 2.1. For $t = 0.40$ results are

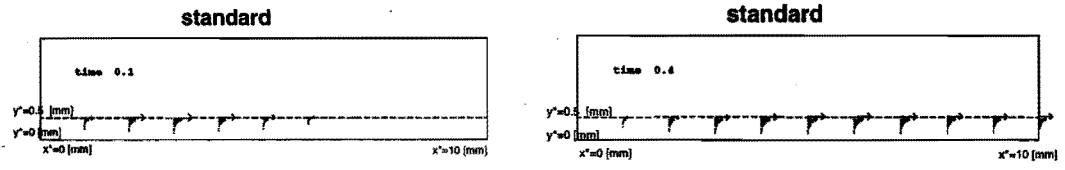

Figure 2.10: The configuration in the physical domain with the dimensional velocity field for ($0 \leq x \leq 0.25$) for test case 1, see table 2.6 at time $t = 0.10$ (velocities multiplied by factor 0.25) and time $t = 0.40$ (velocities multiplied by factor 0.025).

test case	n_0	n_1 $\times 10^{-5}$	n_2 $\times 10^{-4}$	n_9 $\times 10^{-4}$	n_{10} $\times 10^{-4}$	n_{11} $\times 10^{-7}$	n_{12} $\times 10^{-7}$	n_{13} $\times 10^{-7}$	n_{14} $\times 10^{-7}$	n_{15} $\times 10^{-7}$
1	1.00	−3.94	−1.28	−2.74	−2.02	3.29	3.37	–	–	–
6	1.00	−3.94	−1.28	−2.74	−2.02	3.29	3.37	3.11	2.68	2.18

Table 2.4: the n_b-coefficients for test cases 1 and 6, with $n_b = 12$ and $n_b = 15$, respectively and $n_{kc} = 10$.

compared with each other in Fig. 2.15. Since $t^* \propto 1/h_0^*$, $u^* \propto h_0^*$ and $v^* \propto h_0^{*2}$ for thicker layers in the dimensionless plots, the lower layers have a lower x-component of the velocity and the velocity component in y-direction is smaller. Fig. 2.16 gives for comparison at the same dimensional time $t^* = 0.013$ s the dimensional velocities in the scaled cavity. The second column shows the dimensional velocities at the same time in physical space. Spreading of momentum into the lower liquid layers is the same in all cases. The driving forces at the interface are the same which means that velocity gradients $\partial u/\partial y$ in the liquid layers are about equal, as indicated by the tangential stress condition Eq. (2.11). Small differences in these cases are due to the influence of the no-slip condition at the bottom wall. Its effect is more pronounced for more shallow layers.

It is interesting to observe the velocity field and interface deformation at later times, e.g. $t = 4.9$ as shown in Fig. 2.17. A roll-cell has been developed at the same position underneath the surface. This is in agreement with results from literature where roll-cells are often predicted [11][24][31][32] for low-viscosity liquids in thin layers. For test case 1, $h_0^* = 0.5$ mm, the layer is too thin for a roll-cell to develop. Note also in Fig. 2.17 that the interface deformation for $h_0^* = 1.5$ mm decreases near $x = 0$ and increases near $x = 0.4$.

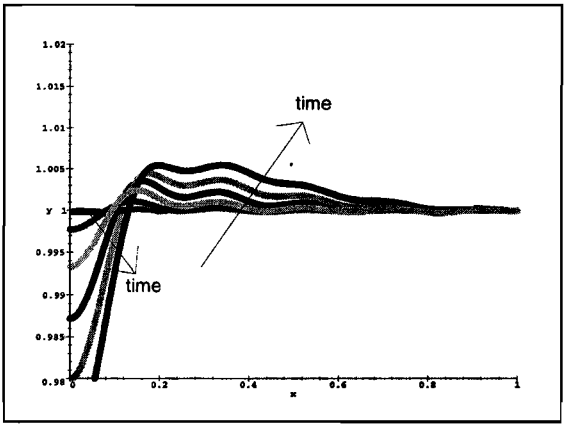

Figure 2.11: The interfacial height computed for test case 1 (see table 2.1) at $t = 0$, 0.10, 0.20, 0.30, 0.40, 0.50 and 0.60.

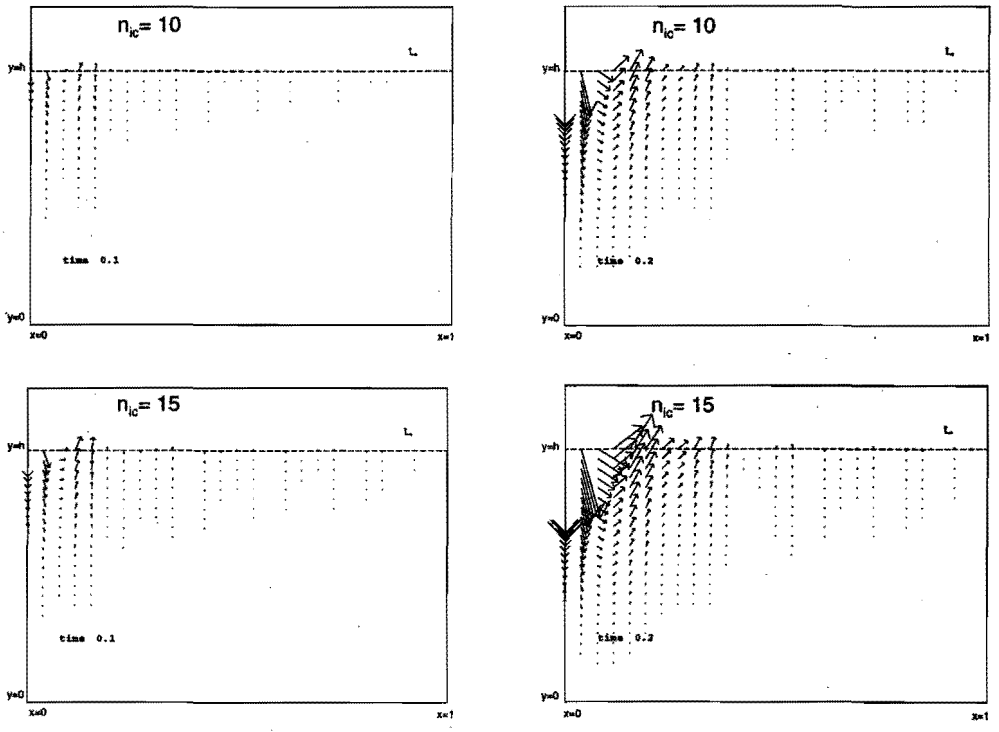

Figure 2.12: The velocity field for $n_{ic} = 10$, above (test case 3), and 15, below (test case 4, see table 2.6), at times $t = 0.10$ and 0.20. Reference arrow of the velocity component in x-direction corresponds to 1.03 mm/s. Reference arrow of the velocity component in y-direction corresponds to 0.017 mm/s.

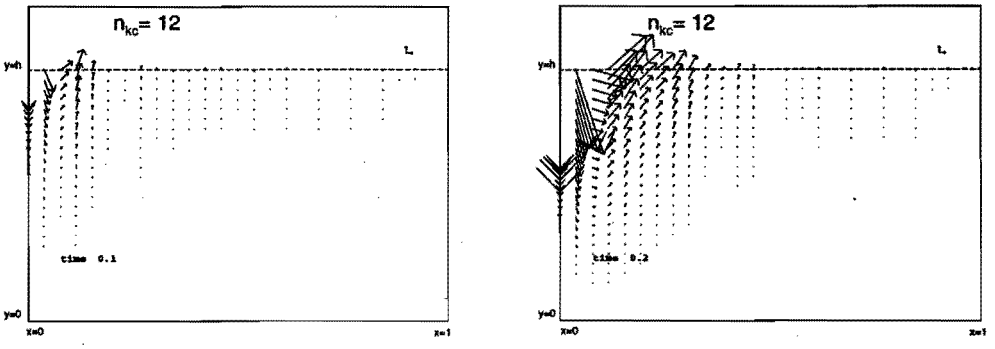

Figure 2.13: The velocity field for $n_{kc} = 12$ and $n_{ic} = 30$ (test case 5, see table 2.6) at times $t = 0.10$ and 0.20. Reference arrow of the velocity component in x-direction corresponds to 1.03 mm/s. Reference arrow of the velocity component in y-direction corresponds to 0.017 mm/s.

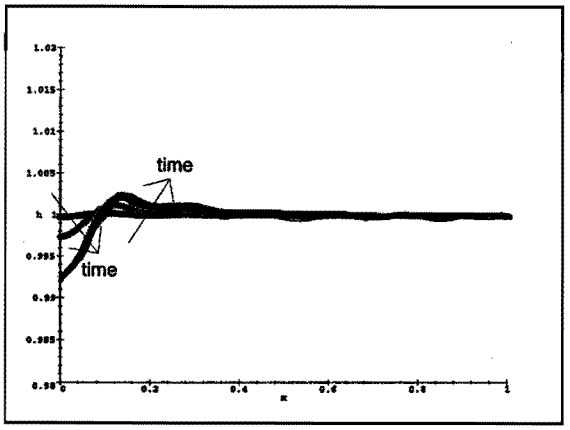

Figure 2.14: The interfacial height computed for test case 5 (see table 2.6) at $t = 0$, 0.10, 0.20 and 0.30.

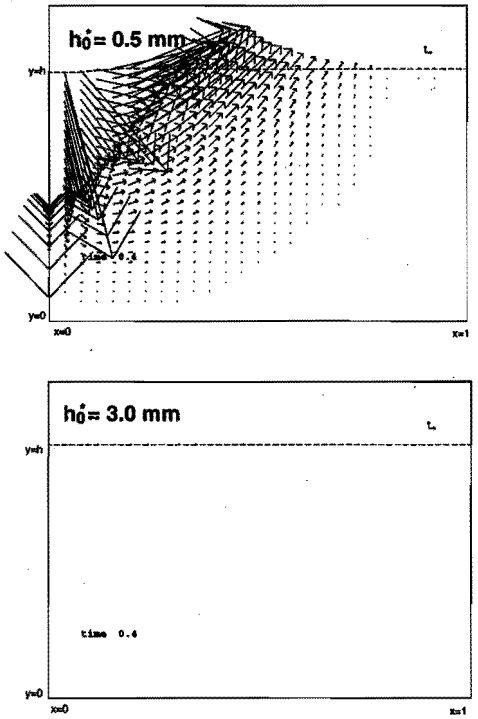

Figure 2.15: The velocity field for test cases 1, 7 and 8 (see table 2.6) at time $t = 0.40$. Reference arrow of the velocity component in x-direction corresponds to 1.03 mm/s. Reference arrow of the velocity component in y-direction corresponds to 0.017 mm/s.

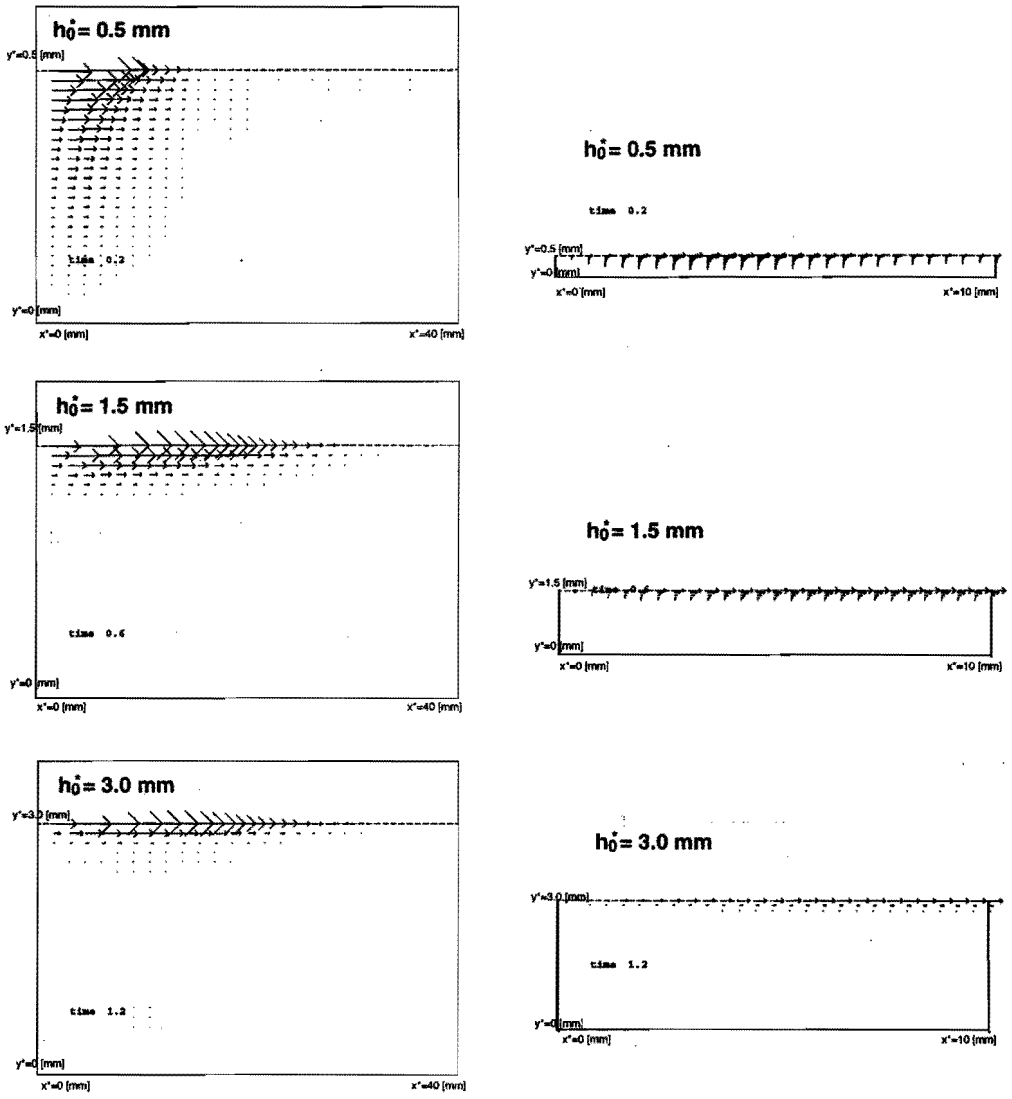

Figure 2.16: The dimensional velocity field in the scaled configuration ($0 \leq x \leq 1.0$, velocities not multiplied) and in configuration in physical space ($0 \leq x \leq 0.25$, velocities multiplied with factor 0.2) for test cases 1, 7 and 8, at the same dimensional time $t^* = 0.013$ s.

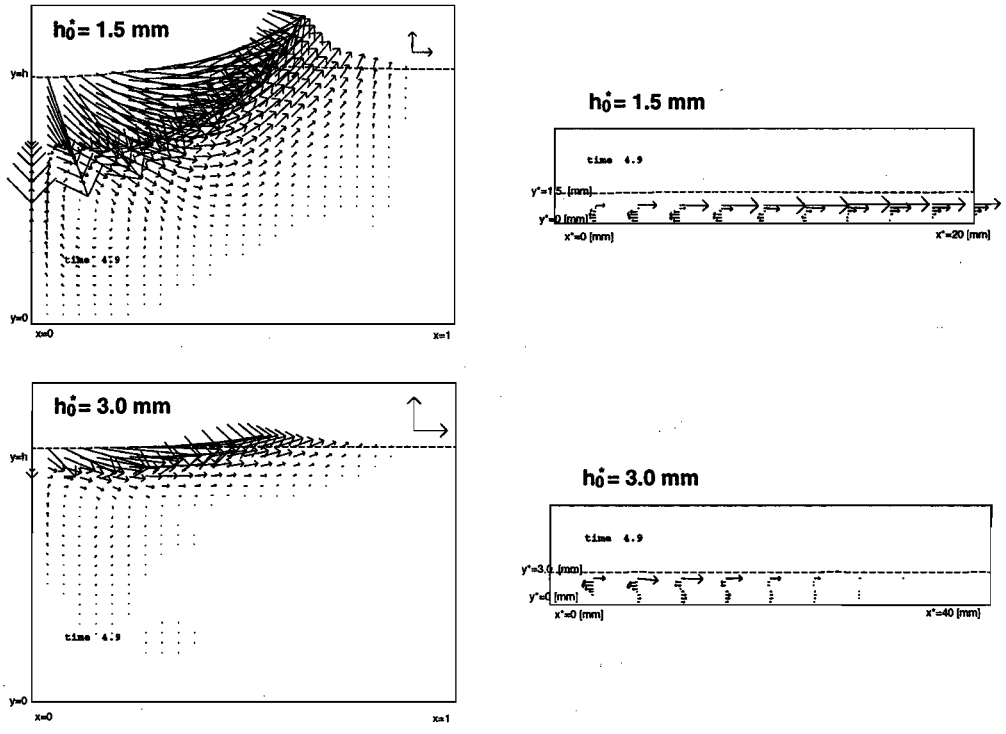

Figure 2.17: The velocity field with interfaces of the test cases 7 and 8 (see table 2.6) of Fig. 2.15 and Fig. 2.16 at time $t = 4.9$ in dimensionless presentation and in physical domain. Reference arrow of the velocity component in x-direction corresponds to 1.03 mm/s. Reference arrow of the velocity component in y-direction corresponds to 0.017 mm/s. The configuration in physical domain is for $h_0^* = 1.5$ mm shown for $0 \leq x \leq 0.50$, velocities are multiplied with a factor 0.5, for $h_0^* = 3.0$ mm it is shown for the whole cavity without multiplication. For clarity, the velocities near the interface are not shown in the plots in the physical domain.

Viscosity variation

The test cases in this section have been for low-viscosity liquids (water). Now a 85% (weight percentages) glycerol in water solution is considered. The viscosity at 20°C is $\mu \approx 0.1002$ Pas [40]. In this test only one damping coefficient ($\lambda_0 = 100$) and three terms of the polynomial expansion appeared to be necessary. This is because for the same driving force the diffusion of momentum to deeper layers results in smaller velocity gradients for the more viscous fluids. Dimensionless plots of results of test case 9, see table 2.6 are shown in Fig. 2.18 at dimensionless times $t = 0.05$, 0.10, 0.35 and 10.0. Viscous damping is larger in the layer with high viscosity, so diffusion into the layer is not as deep. Comparison with Fig. 2.7 confirms this since diffusion takes more time and the dimensionless velocities are much smaller than in test case 1. With increasing time the energy dissipated in the fluid increases and the contour integrals become relatively more important. Since $u^* \propto 1/\mu$ and $v^* \propto 1/\mu$,

the dimensional velocities become even smaller at higher viscosity than at lower values. This result shows that liquids with higher viscosity are harder to set into motion than those with smaller viscosity.

In Fig. 2.19 plots for the same situation but with the surface tension profile 2, test case 10, see table 2.6, are shown for times $t = 0.01$, 0.02, 0.05 and 0.10. The profile stays at its maximum from $t = 0.20$ on. The difference between the surface tension profiles is that in the latter case more energy is put into the fluid per time interval, which results in a larger velocity near the interface and in a larger diffusion of momentum into the layer.

Dimensional result, see Fig. 2.20, at $t = 0.1$ for the test cases with higher viscosity and with different surface tension profiles, test case 9 and 10 (see table 2.6) respectively, show that the velocity is primarily in x-direction and the component of the velocity in y-direction is very small.

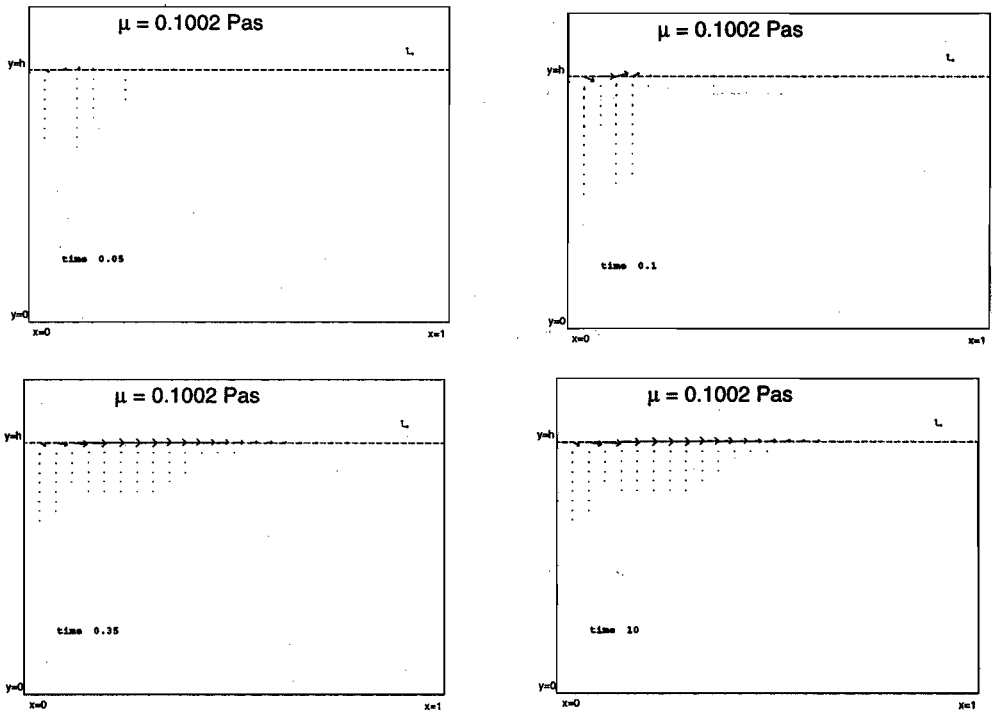

Figure 2.18: The velocity field for liquids with higher viscosity (test case 9 see table 2.6) at times $t = 0.05, 0.10, 0.35$ and 10.0. Reference arrow of the velocity component in x-direction corresponds to 6.15×10^{-2} mm/s. Reference arrow of the velocity component in y-direction corresponds to 6.15×10^{-3} mm/s.

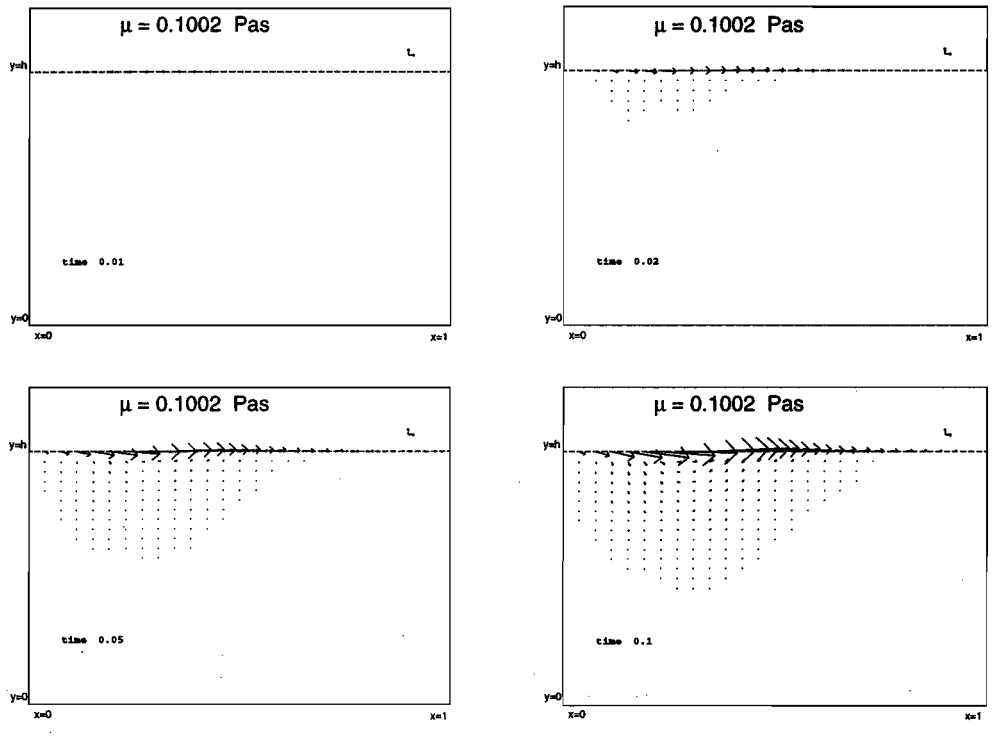

Figure 2.19: The velocity field for liquids with higher viscosity with surface tension profile 2 (test case 10 see table 2.6) at times $t = 0.01$, 0.02, 0.05 and 0.10. The reference arrow of the velocity component in x-direction corresponds to 6.15×10^{-2} mm/s and the reference arrow of the velocity component in y-direction corresponds to 6.15×10^{-3} mm/s.

Damping

The viscous damping of the motion is tested with surface tension distribution 1, viscosity $\mu = 0.1002$ Pas, $A = 3/40$, $n_k = n_i = 100$, $n_{kc} = 10$, $n_{ic} = 4$ and $n_b = 12$, see test case 11 of table 2.6. One damping coefficient ($\lambda_0 = 100$) and three terms of the polynomial expansion are used. The surface tension increases until $t = 0.35$ and subsequently decreases from then on to zero at $t = 0.72$ and remains zero afterwards. Results are shown in Fig. 2.21 at times $t = 0.35, 0.50, 0.70$ and $t = 1.0$. At $t = 0.35$ the maximum velocity is reached. After that time velocities in the fluid and at the interface vanish due to viscous damping in the fluid, as expected.

The effect of viscous damping has also been analyzed in absence of interfacial stresses. The configuration used is again the one of Fig. 2.1, with aspect ratio $A = 3/40$, viscosity $\mu = 1.002 \times 10^{-3}$ Pas, $g = 0$, $n_k = n_i = 50$, $n_{kc} = 6$, $n_{ic} = 3$, $n_b = 20$, and the dimensionless timestep $\Delta t = 0.1$, which corresponds to $0.108 \times 10^{-2} s$, see test case 12 of table 2.6. Only a small number of coefficients suffices. Exponentials are not used since a boundary layer does not develop in this case. The height is kept constant, i.e. $h = 1.0$ at all times, i.e. $\frac{\partial h}{\partial x} = 0$; $\frac{\partial^2 h}{\partial x^2} = 0$; $\frac{\partial h}{\partial t} = 0$. The kinematic boundary

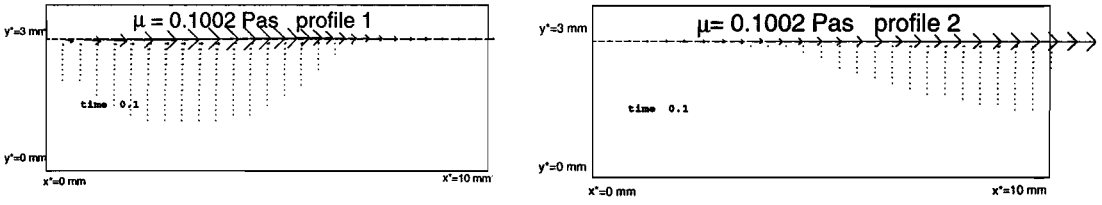

Figure 2.20: Velocity field in the physical domain for test cases with higher viscosity and with different surface tension profiles, test case 9 and 10 (see table 2.6) respectively, for $0 \leq x \leq 0.25$ at time $t = 0.10$. For test case 9 the velocities are amplified $4\times$, for test case 10, $0.8\times$.

condition, Eq. (2.15) yields $v = 0$ at the interface. Only the $d_{0,0}$-coefficient at $t = 0$ is given a value: 0.05. In Fig. 2.22 plots of dimensionless velocities are shown. The initial liquid motion is seen to subdue in time due to viscous damping. The evolution of the kinetic energy, E_{kin}, defined as the sum of $u^2 + v^2$ at all collocation points, is presented in table 2.5. It is concluded that the method takes viscous damping well into account.

time t	kinetic energy E_{kin}
0.1	2.38×10^{-2}
0.5	1.76×10^{-3}
1.0	6.39×10^{-5}
2.0	8.87×10^{-8}
4.0	1.97×10^{-13}
50.0	5.59×10^{-68}

Table 2.5: Kinetic energy at time t with excited velocity at $t = 0.0$, realized by giving $d_{0,0}$-coefficient the value 0.05, $n_k = n_i = 50$, $n_{kc} = 8$, $n_{ic} = 5$, $n_b = 20$, and $\Delta t = 0.1$.

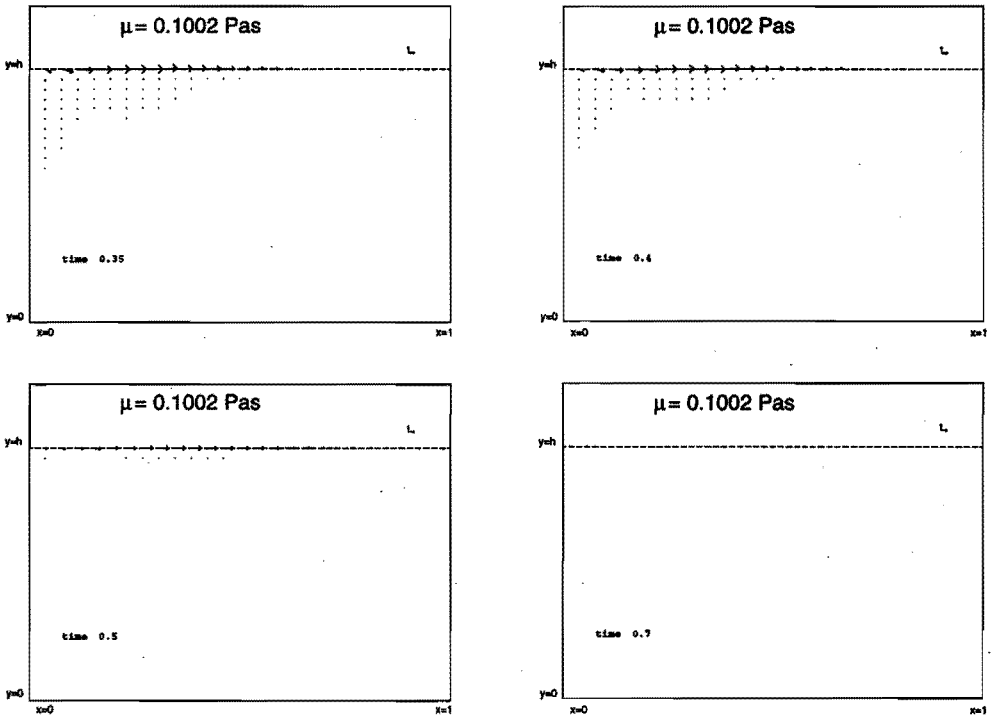

Figure 2.21: The velocity field of test case with surface tension profile 1 which decreases from $t = 0.35$ to zero at $t = 0.72$ and stays zero afterwards and viscosity $\mu = 0.1002$ Pas, (see test case 11 of table 2.6) at times $t = 0.35$, 0.40, 0.50, and 0.70. Reference arrow of the velocity component in x-direction corresponds to 6.15×10^{-2} mm/s. Reference arrow of the velocity component in y-direction corresponds to 6.15×10^{-3} mm/s.

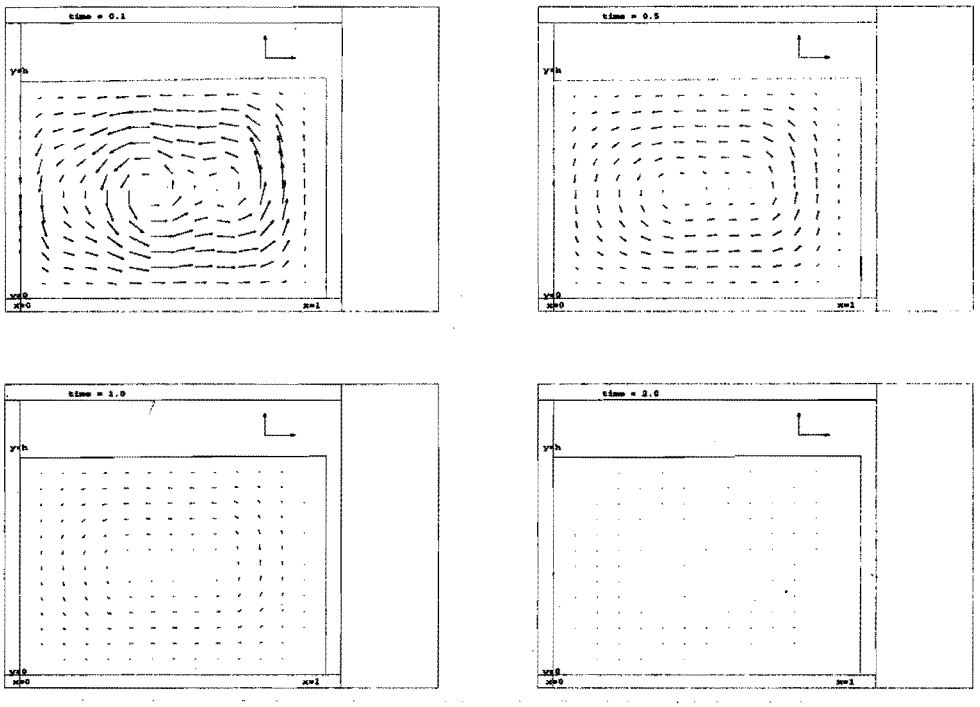

Figure 2.22: Time evolution of liquid motion due to viscous damping, with h is kept 1.0 and $g = 0$ (test case 12 of table 2.6). The reference arrow of the velocity component in x-direction has value 1.9×10^{-2} m/s, the reference arrow of the velocity component in y-direction has value 1.4×10^{-3} m/s.

2.5 Conclusions

In this chapter a computational method for two-dimensional flow is described which predicts the time evolution of the velocity field and the interfacial motion in a thin liquid layer. The method is based on the spectral collocation technique with a grid adapting to the moving free interface. Explicit time integration is used and iterations are not employed. The algorithm takes special care of the interface tangential stress condition, which is solved simultaneously with the contour-integrated Navier-Stokes equations. An adapted SVD-treatment is employed in the approach which balances the weight of the contour integrals and the tangential stress condition. One "spectral element" is used with a single velocity expansion so that coupling problems at element boundaries are avoided and the main emphasis is on satisfying the boundary conditions at the interface. In future the method can be extended with a segmentation of the physical domain with for each sub-segment a suitable expansion [26]. The kinematic boundary condition couples the evolution of the velocity field to the interface behaviour using series of orthogonal functions and an Adams-Bashford integration technique. Since the solution is based on truncated expansions, the accuracy of the solution is directly controlled.

The method is applied on two test cases: an analytical test case and a constructed one. The

case	n_k	n_i	n_b	n_{kc}	n_{ic}	h_0^*	A	λ	μ	#
2	50	50								
3			12	10	10					
4			12	10	15					
5			12	12	30					
6			15	10	30					
7						1.5	3/80			
8						3.0	3/40			
9			12	10	4	3.0	3/40	100	0.1002	
10			12	10	4	3.0	3/40	–	0.1002	2
11			12	10	4	3.0	3/40	100		with damping
12	50	50	20	6	3	3.0	3/40	–		with damping

Table 2.6: Parameter changes of test cases 2 through 12. See table 2.1 for the other parameters. Only variations with respect to table 2.1 are indicated. # means gradient profile history.

analytical one is a stationary, heated thin layer in steady motion, for which analytical solutions are available. The computational method can generate these solutions and is found to precisely predict the expansion coefficients. The other test case consists of prescribed surface tension histories which are analytically derived.

From these test cases it is concluded that the velocity expansion converges quite rapidly and that the tangential stress condition at the interface is well satisfied. In the physical domain, large velocities in horizontal direction are established and the vertical velocity component seems to be negligible.

Several tests are performed.

- Variation of the discretization parameters has been investigated. In general an equidistant 100×100 collocation point distribution, with 10 coefficients in x-direction, 30 coefficients in y-direction for the velocity expansion and 12 coefficients for the interface expansion are adequate to obtain reliable results. For some specific test cases other values can be used.

- Variation of the viscosity shows that liquids with higher viscosity are more difficult to set into motion that those with lower viscosity.

- Viscous damping test cases show that, when the driving force decreases or is absent, the velocity in the liquid subdues quickly.

- The aspect ratio has been varied in order to investigate the propagation of momentum into the bulk of the liquid and to obtain results for layers of practical interest.

The results of various test cases showed that the present computational method produces results comparable to results from similar investigations in the literature, both numerically and experimentally.

It is concluded that the new method accurately predicts thermocapillary two-dimensional Marangoni convection in cavities.

Chapter 3

Alternative expansions

3.1 Introduction

The method of chapter 2 can be used in combination with various boundary conditions. Various boundary conditions can be satisfied employing an alternative velocity expansion that is tailored to these conditions. The main objectives of this chapter are:

- To examine the robustness of the solution algorithm. In particular, whether it may accommodate different functions in the expansion for the velocity field and the one for the interface.
- To compare predictions for various boundary conditions and experiments.

The initial test configuration is the one of Fig. 2.1, i.e. a cross-section of a rectangular cavity with a liquid layer at the bottom. The velocity field in general form is expressed as:

$$u(x,y,t) = \sum_{i=0}^{n_l} \sum_{k=0}^{n_{kc}-1} d_{i,k}(t) f_k(x) \frac{y}{h(x)} e^{\lambda_i \left(\frac{y}{h(x)}-1\right)} + \sum_{i=n_l+1}^{n_{ic}-1} \sum_{k=0}^{n_{kc}-1} d_{i,k}(t) f_k(x) \left(\frac{y}{h(x)}\right)^{i+1} \tag{3.1}$$

with λ_i non-negative constants. Choosing $f_k(x) = \sin(\pi(k+1)x)$ and $h(x,t) = 1 + \sum_{m=1}^{n_b} b_m \cos(\pi m x)$ results in the functions of chapter 2. The functions in expansion 3.1 span the whole domain, i.e. only one single element in each direction represents the entire flow area.

In section 3.2 three alternative expansions $f_k(x)$ are presented, each tailored to satisfy specific boundary conditions. More details about these expansions are described by Pijnappel et al. [33]. Tests and results are evaluated in section 3.3. In section 3.4 concluding remarks are presented.

3.2 Alternative expansions

3.2.1 Extra linear term

In the method of chapter 2 emphasis was on the requirement $v = 0$ at $x = 1$ which is not automatically satisfied by the choice of the functions in the expansion alone. Discarding the solid boundary at $x = 1$ enables to have $u \neq 0$ there. An extra term in the x-dependent part of the velocity expansion accounts for this situation:

$$\begin{aligned} u(x,y,t) = & \sum_{i=0}^{n_l} \left(\sum_{k=0}^{n_{kc}-2} d_{i,k}(t) \sin(\pi(k+1)x) + d_{i,n_{kc}-1}(t) x \right) \frac{y}{h(x)} e^{\lambda_i \left(\frac{y}{h(x)}-1\right)} \\ & + \sum_{i=n_l+1}^{n_{ic}-1} \left(\sum_{k=0}^{n_{kc}-2} d_{i,k}(t) \sin(\pi(k+1)x) + d_{i,n_{kc}-1}(t) x \right) \left(\frac{y}{h(x)}\right)^{i+1} \end{aligned} \tag{3.2}$$

A suitable expansion for the position of the interface which satisfies symmetry at $x = 0$ and matches the right-hand side and left-hand side of the kinematic boundary condition Eq. (2.15), see appendix D, is:

$$h(x,t) = \sum_{l=1}^{\infty} \sum_{m=0}^{\infty} \tau_{l,m} x^l \mathrm{sn}(l,m) \tag{3.3}$$

with

$$\begin{aligned} \mathrm{sn}(l,m) &= \cos(\pi m x) \quad \text{if l is even} \\ \mathrm{sn}(l,m) &= \sin(\pi m x) \quad \text{if l is odd} \end{aligned} \tag{3.4}$$

3.2.2 Chebyshev polynomials

Consider the following set of boundary conditions:

1. The flow is symmetrical about $x = 0$, i.e. the x-component of the velocity is anti-symmetrical so that $u(-x,y,t) = -u(x,y,t)$
2. No-slip at the bottom, i.e. $u(x,y,t) = 0$, $v(x,y,t) = 0$ at $y = 0$

Odd Chebyshev polynomials:

$$T_{2k+1}(x) \quad (k \in N) \tag{3.5}$$

satisfy these conditions so they could be used instead of $f_k(x)$ in Eq. (3.1). In Fig. 3.1 the first 6 Chebyshev polynomials are shown. They are defined by $T_k(x) = \cos(k \arccos x)$ in the domain

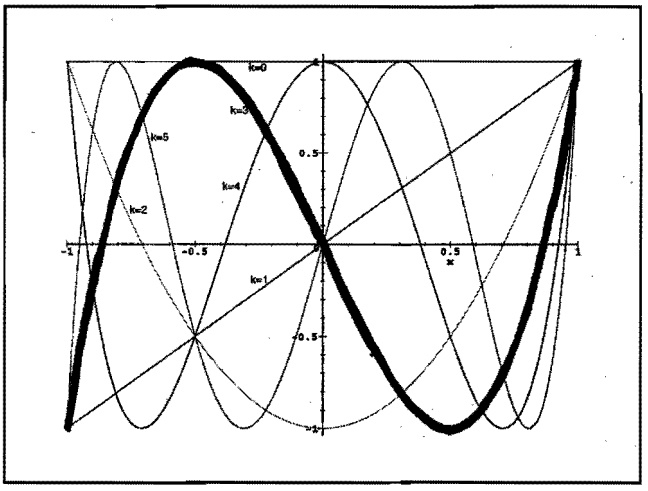

Figure 3.1: Chebyshev polynomials $T_k(x) = \cos(k \arccos x)$ on the domain $-1 \leq x \leq 1$.

$-1 \leq x \leq 1$. $T_0(x) = 1$, $T_1(x) = x$ and $T_2(x) = 2x^2 - 1$. The recursion relation used to calculate $T_k(x)$ for $k \geq 2$, is: $T_{n+1}(x) = 2xT_n(x) - T_{n-1}(x)$.

All zeros of a Chebyshev polynomial and all its extremes are in the interval of interest, $-1 \leq x \leq 1$, and all extremes are equal to 1 or -1. This oscillation between extreme values of equal magnitude is known as the equal-ripple property which ensures that the interpolation error is evenly spread over the entire interval.

For the interface description only symmetry at $x = 0$ has to be satisfied. To match the right-hand side and left-hand side of the kinematic boundary condition, Eq. (2.15), the appropriate choice in terms of Chebyshev polynomials, $T_m(x)$, is:

$$h(x,t) = \sum_{m=0}^{n_b} b_m T_{2m}(x) \tag{3.6}$$

3.2.3 "Chandrasekhar" polynomials

Consider the following boundary conditions:

1. Symmetry around $x = 0$, i.e. u(-x,y,t) = -u(x,y,t)
2. No-slip at the bottom, i.e. $u(x,0,t) = 0$, $v(x,0,t) = 0$ at $y = 0$ for $x \in [0,1]$
3. No-slip at $x = 1$, i.e. $u(1,y,t) = 0$, $v(1,y,t) = 0$ at $x = 1$

For the function $f_k(x)$ this yields:

1. $f_k(-x) = -f_k(x)$, derived from anti-symmetry of the x-component of the velocity at $x = 0$
2. $f_k(1) = 0$, derived from $u(1,y,t) = 0$ at $x = 1$
3. $\partial f_k/\partial x(1) = 0$, derived from $v(1,y,t) = 0$ at $x = 1$

To obtain symmetry at $x = 0$ for the interface h, so h(-x) = h(x), the $d_{i,k}$-coefficients of Eq. (3.2) can be chosen $d_{0,k} = 1$ and $d_{i,k} = 0$ for $i \neq 0$ or $k \neq l$. This gives a basic function set for $l \leq 0$ and for $i \leq 0$.

The reverse is also true; if a function $f_k(x)$ satisfies the above mentioned three conditions, then u is odd in x and u satisfies the no-slip condition at $x = 1$. For the construction of such a function $f_k(x)$ the solution of the following characteristic value problem is used:

$$\frac{d^4y}{dx^4} = \alpha^4 y \tag{3.7}$$

Here α^4 is used rather than α which will be shown to be more suitable for the present purpose. The boundary conditions are:

$$y(-1) = 0\,;\, y(1) = 0\,;\, \frac{dy}{dx}(-1) = 0\,;\, \frac{dy}{dx}(1) = 0 \tag{3.8}$$

and y is an odd function of x. Let α_k denote a characteristic value and let y_k $(= f_k(x))$ be the proper solution belonging to it. Then, multiplying Eq. (3.7) for y_k by y_n (belonging to α_n) and integrating over the range of x, one obtains:

$$\alpha_k^4 \int_{-1}^{1} y_k y_n dx = \int_{-1}^{1} y_n \frac{d^4 y_k}{dx^4} dx \tag{3.9}$$

Integrating twice by parts, turns the right-hand side of Eq. (3.9) into:

$$\int_{-1}^{1} \frac{d^2 y_n}{dx^2} \frac{d^2 y_k}{dx^2} dx \tag{3.10}$$

The boundary term vanishes (both times) due to the boundary conditions on y_n. From the symmetry in n and k of the integral on the right-hand side of Eq. (3.10), it follows that:

$$(\alpha_k^4 - \alpha_n^4) \int_{-1}^{1} y_k y_n dx = 0 \tag{3.11}$$

Hence, for $k \neq n$

$$\int_{-1}^{1} y_k y_n dx = 0 \tag{3.12}$$

The solutions y_k, therefore, form an orthogonal set. It can be shown that this set is complete, i.e. every continuous function in the interval $(-1, 1)$ and its first derivative with respect to x vanishing at the endpoints of the interval, is an infinite linear combination of the elements of the set $\{y_n, n > 0\}$. The solution of Eq. (3.7):

$$f_k(x) = \frac{\sinh(\alpha_k x)}{\sinh(\alpha_k)} - \frac{\sin(\alpha_k x)}{\sin(\alpha_k)} \tag{3.13}$$

which satisfies condition 1 and 2. Condition 3 is fulfilled by the choice that each α_k, $k \in N$, is a root of the characteristic equation, derived from $df_k/dx(1) = 0$:

$$\coth(\alpha_k) - \cot(\alpha_k) = 0 \tag{3.14}$$

The asymptotic formula

$$\alpha_k \sim (k + \frac{1}{4})\pi, \quad \text{k} > 4 \tag{3.15}$$

gives the roots, $\alpha_1 = 3.92660231$, $\alpha_2 = 7.06858274$, $\alpha_3 = 10.21017612$ and $\alpha_4 = 13.35176878$. Note that if in Eq. 3.7 α was used instead of α^4 that in Eq. 3.13 $\alpha_k{}^{1/4}$ would appear.

The expansion for the height function, h(x,t), has to satisfy $h(-x,t) = h(x,t)$ and $\partial h/\partial x(1,t) = 0$ ($v = 0$ at $x = 1$). Therefore the interface expansion is chosen as follows:

$$h_m(x) = 1 + \sum_{m=1}^{n_b} b_m \left(\frac{\cosh(\mu_m x)}{\cosh(\mu_m)} - \frac{\cos(\mu_m x)}{\cos(\mu_m)} \right)$$

with the roots μ_m, $m \in N$, derived from $\partial h/\partial x(1,t) = 0$, of the equation:

$$\tanh(\mu_m) + \tan(\mu_m) = 0 \tag{3.16}$$

The asymptotic formula

$$\mu_m \sim (m - \frac{1}{4})\pi, \quad \text{m} > 4 \tag{3.17}$$

gives the roots, $\mu_1 = 2.36502037$, $\mu_2 = 5.49780392$, $\mu_3 = 8.63937983$ and $\mu_4 = 11.78097245$.

In appendix D analytical relations for db/dt based on the kinematic boundary condition are presented for the expansion with the extra linear term and the one with the Chebyshev polynomials. The analytical relations are exact, although numerically they are evaluated with finite accuracy. The kinematic boundary condition cannot be solved analytically for the Chandrasekhar polynomials since the left-hand side and right-hand side are two non-combining groups. To generalize the solution of the db/dt-coefficients as an alternative a least-square method is applied, as described in section 2.3.5.

n_k	n_i	n_b	n_{kc}	n_{ic}	Δt	g	h_0^*	A	r	j	λ_0	λ_1	λ_2	μ [Pas]	#
100	100	12	10	10	0.01	0	0.5	$\frac{1}{80}$	n_{kc}	$n_{ic} \times n_{kc} - r$	100	10	3	1.002×10^{-3}	1

Table 3.1: Values of parameter set. # means gradient profile history.

3.3 Tests and results

The expansions presented in chapter 2 and the ones presented in this section are compared in a test with the parameter values given in table 3.1. The surface tension gradient history of Eq. (C.1) is prescribed. All used alternative velocity expansions contain three exponential functions to ensure that the noise signal as compared to the significant signal is small since there is a sharp transition in singular value from significant to noise related ones, see section 2.3.4. In Fig. 3.2 the velocity and interface are shown for the three alternative expansions, at time $t = 0.10$ and 0.20. For the standard expansions, see Fig. 2.13, chapter 2. The flow patterns are nearly the same for each of the three expansions, which proves that the method does not depend very much on the chosen expansions. The magnitude of the velocity predicted by the standard velocity expansion of chapter 2 is smaller than the one predicted by the other methods. The reason is obvious: too few coefficients are taken into account since with $n_{ic} = 30$ the velocities have equal values, see Fig. 2.7. The Chebyshev polynomials have derivatives exceeding zero at $x = 1$, resulting in errors at that location. The "Chandrasekhar" expansions and the one based on the expansions with extra linear term produce nearly equal results. Evidently, the solid boundary at $x = 1$ has little influence on the selected surface tension gradient profile. This is easy to understand since induced velocities near $x = 1$ have to be small and hardly affect the flow field near $x = 0$. Furthermore, expansions based on symmetrical or antisymmetrical elementary functions, yield identical results.

Results of the method with the Chebyshev polynomials are compared with results of the method with the standard expansions for a deeper cavity, with $h_0^* = 6.0$ mm and $L = 40.0$ mm ($A = 0.15$) and are presented in Fig. 3.3. Other parameters are chosen as in table 3.1.

The error at $x = 1$ in the method with the Chebyshev polynomials is for the deeper cavity smaller than for a thinner layer. The reason is the following. Velocities are less diffused by momentum exchange due to viscosity which is in agreement with the tests with the three aspect ratios described in chapter 2. Errors near $x = 1$ are therefore smaller. The velocities in Fig.3.3 are small compared to the ones in Fig. 3.2. The reason is twofold. Since the absolute time is proportional to the inverse of the interfacial height, $t^* \propto 1/h_0^*$, only a short time has past for thicker layers as compared to the case of thinner layers and the fluid is not yet accelerated much. Furthermore, the dimensional velocity is proportional to h_0^*, $u^* \propto h_0^*$ and $v^* \propto h_0^{*2}$, so in dimensional plots for a thick layer the velocities will become larger than for a thinner layer.

Another test is carried out to investigate the difference in the solution due to imposing a condition at $x = 1$. The results of the method with the standard expansions and the results of the method with extra linear term are compared for a cavity with $L = H = 0.5$ ($A = 1.0$). The results are shown in Fig. 3.4. Although the no-slip condition $v = 0$ at $x = 1$ in the standard expansions is used, small velocities still exist near $x = 1$. Apparently, the mere adding of the extra no-slip condition via extra equations in the solving routine (SVD) is insufficient for satisfying the no-slip condition precisely. The reason is the use of the SVD algorithm, see chapter 2 and appendix B. The expansions with extra linear term contains larger velocities near $x = 1$ as expected because of the absence of the no-slip velocity at $x = 1$.

3.4 Conclusions

The method gives similar results for the velocity field and interfacial height for versions of the method with different expansion functions. Each version accommodates a specific set of boundary conditions best. More accurate numerical predictions can therefore be done by selecting the appropriate set of basic expansion functions. Some specific tests have been performed to highlight the differences of the different expansion functions. The solution algorithm is found to be robust with respect to the choice of the expansion functions, i.e. it functions well for various expansions.

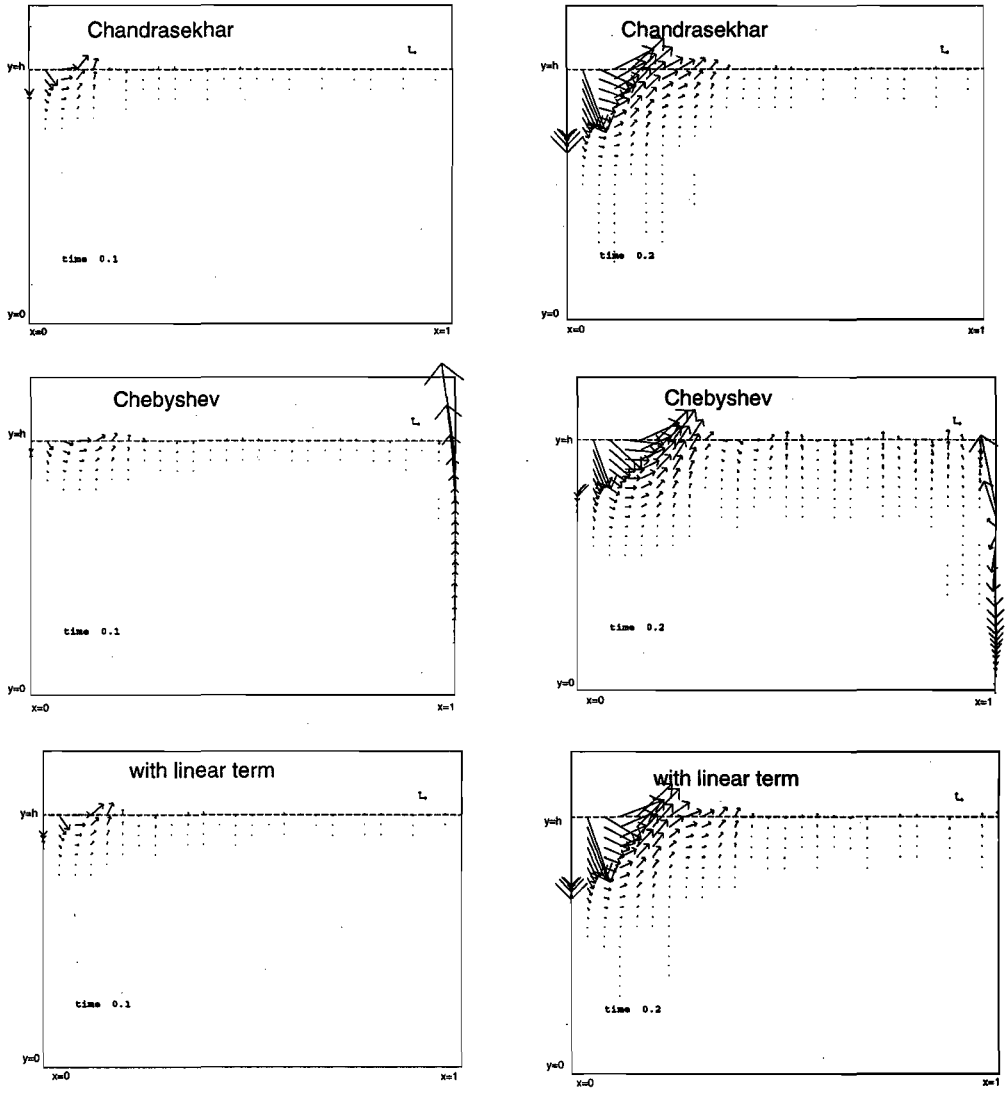

Figure 3.2: The velocity field for the "Chandrasekhar" expansions (top), Chebyshev polynomials (centre) and standard expansions with extra linear term (bottom) at time $t = 0.10$ and 0.20, with $n_{kc} = n_{ic} = 10$, see table 3.1. Reference arrow of the velocity component in x-direction corresponds to 1.03 mm/s. Reference arrow of the velocity component in y-direction corresponds to 0.017 mm/s.

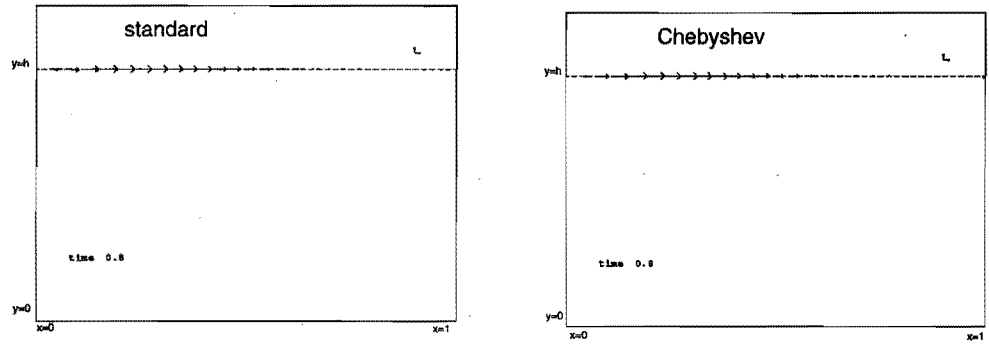

Figure 3.3: The velocity field for the standard expansions and the Chebyshev polynomials at time $t = 0.80$, with $h_0^* = 6$ mm, $L = 40$ mm ($A = 0.15$), see table 3.1. Reference arrow of the velocity component in x-direction corresponds to 12.3 mm/s. Reference arrow of the velocity component in y-direction corresponds to 2.46 mm/s.

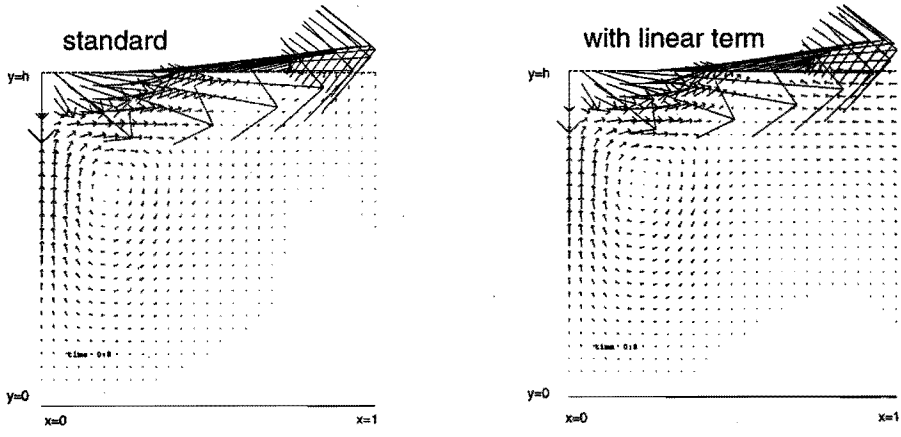

Figure 3.4: The velocity field for the standard expansions and expansions with extra linear term for the velocity at time $t = 0.80$, with $h_0^* = L = 0.5$ mm ($A = 1.0$). For other parameters see table 3.1. Reference arrow of the velocity component in x-direction corresponds to 1.66 mm/s. Reference arrow of the velocity component in y-direction corresponds to 2.21 mm/s.

Chapter 4

Experiments with a liquid layer heated from above

4.1 Introduction

The method of section 2 is validated by experiments. The main aims are:

- to accurately measure the temperature gradient along the interface
- to visualize the generated flows.

The temperature differences along an interface are a measure for the surface tension gradient which is the driving force for thermocapillary convection. The same configuration as the one of section 2 is considered: a liquid layer in a cavity. A temperature gradient is established by radiation from a thin, straight canthal wire, located above the cavity, see Fig. 4.1 and [39]. In this thesis emphasis lies on the study of thermocapillary convection at 1-g. Buoyancy effects are minimized in the experiments by the way the liquid is heated and by using a set-up with relatively small dimensions and with relatively large gradient $\partial\sigma/\partial s$, s being the coordinate along the interface.

Previous work

Szymczyk et al. [41][37] studied thermocapillary and buoyancy convection at 1-g for cases where they are strongly coupled. Visualisation experiments were performed in a rotating cylindrical glass-cell with a vertical fluid-gas zone heated from above and cooled from below [41]. Two buoyancy related forces were established, one due to variation in density and one due to centrifugal forces; a thermocapillary force was caused by the non-uniform temperature field at the interface. They showed that the influence of the surface tension and the centrifugal forces on convection is significant, and that density differences are of minor importance. Four flow patterns were found as a function of the Marangoni number, Ma, and the rotational speed. The Marangoni number is defined by $Ma = ((\partial\sigma/\partial T)\ \Delta T\ L)\,/\,(\rho\ \nu\ \kappa)$, with L a characteristic dimension, ρ the mass density, ΔT a characteristic temperature difference, T the liquid temperature, ν the kinematic viscosity and κ the thermal diffusivity defined by $K = \lambda/(\rho c)$ with λ the heat conductivity and c the heat capacity. The onset of thermocapillary convection was found to be independent of the centrifugal force. In another experiment, consisting of a transparent cube with a cylindrical bore hole, non-horizontal isotherms in the fluid were measured by using liquid crystals tracers. Non-horizontal isotherms are due to lateral cooling and the Marangoni convection which distort the given temperature field. Therefore secondary buoyancy convection was caused [37]. Szymczyk et al. concluded that even the smallest horizontal

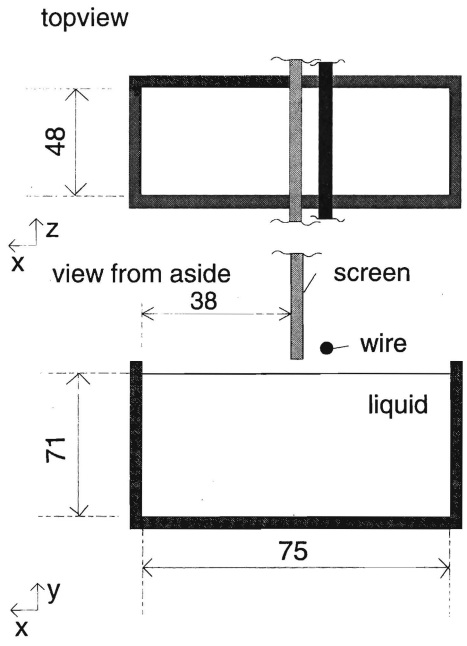

Figure 4.1: Schematic of configuration: thin liquid layer heated from above. dimensions in mm

temperature gradient causes buoyancy driven convection and that it is not possible to observe pure Marangoni convection with this set-up in the gravitational field at 1-g.

In thin layers with heated wall(s) it is possible to observe an almost pure Marangoni convection in the gravitational field at 1-g. Schwabe et al. [36] observed Marangoni-Bénard roll-cells in a 5.0 mm thick liquid layer of silicone oil under a 5.0 mm thick He-gas-gap heated from below. They found that at 1-g the main contribution to the onset of convection in such thin layers stems from the Marangoni effect.

Zhang et al. [27] investigated thermal convection by laser shadowgraphy in minute drops on an inclined plate with a temperature gradient. The observation of the flow patterns in a stationary drop revealed the action of both surface tension and buoyancy forces that led to four distinct flow regimes in the drop. Droplets on a horizontal plate show different internal flow patterns: Marangoni flows consisting of a ring of small two-dimensional roll-cells near the foot of the droplet and larger buoyancy flows above this ring that transport heat from the warm to the cold side.

Under reduced gravity, experiments were performed to investigate surface tension driven convection only [4][11][28]. To achieve reduced gravity, many experiments were performed in drop towers [4][28], during parabolic flights of aircraft and during sounding rocket flights [11] or in space [2][5][7][10]. Some interesting experiments are the following. They are discussed here since comparison with our own experiments can be made.

Schwabe et al. [36] performed experiments at microgravity conditions to study pure Marangoni convection. Ostrach et al. [28] visualized fluid motion induced by a surface tension gradient on the free surface of a liquid in a cylindrical container in both reduced gravity (in drop tower) and at 1-g conditions. They measured the temperature difference at the interface with probes. The ratio of surface tension gradient forces to buoyancy forces was found to be of the order of 10^4 at reduced gravity conditions and 0.13 at 1-g. Maximum velocity at the interface, v_{max}, was 3.0 and 1.8 cm/s at

reduced and at 1-g conditions respectively, so v_{max} on earth is smaller than v_{max} under microgravity conditions. Buoyancy convection in a direction opposite to that of Marangoni induced flows could be realized in this experiment.

Petri et al. [4] investigated steady and unsteady flow behaviour of thermally induced flow in a liquid sphere during experiments in a drop tower.

Hoefsloot [11] performed Marangoni flow experiments during rocket flights and parabolic flights. In the first, the mass transfer induced destillocapillary convection around an air bubble was investigated in containers of a cylindrical shape, filled with a 3% acetone in water solution, see Fig. 4.2. The

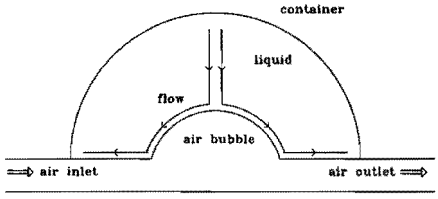

Figure 4.2: Destillocapillary convection around an air bubble.

acetone transitions from the liquid to the gas phase. To prevent the bubble from becoming saturated the bubble was ventilated. The experiments prove that Marangoni convection can be divided into two classes:

- geometrically induced convection (macroscale convection) if the mass transfer across the interface varies gradually
- convection caused by local hydrodynamic instabilities (microscale convection), e.g. in a liquid with initially a uniform solvent concentration surrounding a spherical gas bubble.

This difference is related to the onset of the convection and not to the final state. It turned out that the flow pattern in the liquid depends on the flow rate of the air through the bubble and the size of the bubble.

In parabolic flights, experiments were carried out in several V-shaped containers to investigate the influence of the shape of the gas/liquid interface on the onset of Marangoni convection. It was found that the shape of the interface governs the type of convection. If due to the shape a concentration gradient is not established along the interface, small roll cells will develop, i.e. micro-convection will occur. If a macroscopic gradient along the interface is caused, macro-convection is established. The micro-convection cells did not grow whereas the macroscopic cells did.

From this short review it can be concluded that Marangoni convection can be investigated at 1-g as well as at microgravity conditions, although on earth buoyancy forces can also play a role. Therefore an estimation of the latter in 1-g experiments must be made to show the significance of the Marangoni effect.

In the present experiment the inhomogeneous irradiation establishes a temperature gradient at the liquid interface. This temperature gradient causes a surface tension gradient which gives rise to thermocapillary driven convection. The Marangoni number, as defined before, characterizes this type of flow. A typical value of Ma in the experiment is 1.6×10^5. Here $\partial\sigma/\partial T = 0.1\times10^{-3}$ N/(mK), $\Delta T =$ 5 K, $L = 38\times10^{-3}$ m, $\rho = 752$ kg/m^3, $\nu = 1.9\times10^{-6}$ m^2/s, $\lambda = 0.14$ W/(mK), $c = 2.22\times10^3$J/(kgK) and $\kappa = 8\times10^{-8}$ m^2/s. A density gradient, approximately perpendicular to the interface, may cause

gravity to be active. So-called buoyancy driven convection develops at 1-g conditions if the lowest temperatures occur at the highest positions. Because the layer is heated from above the hottest part is on top. In the liquid layer heated from above buoyancy convection can therefore only be realized if a horizontal temperature gradient is established in the layer below the interface. This would lead to so-called secondary buoyancy convection [37]. The dimensionless parameter characterizing the gravitational convection is the Grashof number, $Gr = (\beta\ g\ \Delta T\ L^3)\ /\nu^2$, with g the gravitation acceleration and β the fluid volumetric expansion coefficient. An estimate of Gr for the conditions of the experiments cannot be made since the hottest fluid is on top. The relative significance of thermocapillary to buoyancy convection is given by the quotient: $((\partial\sigma/\partial T)\ \nu)\ /\ (\rho\ g\ L^2\ \kappa\ \beta)$. This shows that thermocapillary driven flows can best be investigated in microgravity or on earth in small-scale configurations, such as in capillaries, thin films [24], droplets [27] or bubbles. Large values of $\partial\sigma/\partial T$ promote the Marangoni effect. [1]

In section 4.2 the test rig and equipment are described. Results are presented in section 4.3. In section 4.3.3 the relative importance of buoyancy convection compared to Marangoni convection will be estimated showing the dominance of the latter.

4.2 Test rig

4.2.1 Experimental set-up

A schematic of the test rig is shown in Fig. 4.3. The test liquid is n-paraffin $C_{10} - C_{13}$ with mass density $\rho = 752$ kg/m^3 and dynamic viscosity $\mu = 1.43 \times 10^{-3}$ N s/m^2. The rectangular cavity has inside dimensions $L \times W \times H$, $75 \times 48 \times 71$ mm^3. It is made out of laboratory glass and seamless. The test cavity is placed within a basin filled with water that serves as a heat buffer and that is heated to a specific initial temperature. The water can be stirred by the mixer. A $\pm$ 2 mm thick canthal heating wire is positioned along the symmetry-axis of the cavity perpendicular to the xy-plane shown in Fig. 4.3. The heating wire radiates when a voltage of the order of 6 V and a direct current of the order of 4 A is supplied to the wire. Perpendicular to the wire a temperature gradient along the interface is established which is measured with an infrared camera "AGA thermovision 680" with an 8° camera lens (part no. 556 191 215) and a spacing ring (part no. 556 190 768), to be described in section 4.2.2. The total distance from camera via mirror to the interface is approximately 30 cm. The penetration depth of infrared light in n-paraffin is of the order of 0.92 mm, derived from [42], implying that effectively the temperature of the interface is being measured. To facilitate the use of the camera observations are made via a gold covered mirror. Gold reflects $\pm$ 97 % of the infrared radiation in the middle infrared spectrum which is the working domain of the detector. Radiation that would go directly from the canthal wire to the thermograph would blur the measurements. This radiation is shielded by placing a vertical metal screen close to the canthal wire (see Fig. 4.3). This does not affect symmetry of the temperature distribution along the interface since tests with screens on both sides of the heating wire yield results similar to the ones with only one screen. The infrared camera is linked to a computer via an analog-digital converter in order to digitize the images.

To visualize the liquid flow, silver-coated glass microballoons with matched density are used, which were already applied under microgravity conditions by Hoefsloot [11]. It is important that these particles do not sink under influence of gravity. A video camera, Canon UC2 Hi 8 mm, is used to trace light reflected by these particles. The camera is focussed on a single cross-section in a xy-plane. Via a 2 mm slit in front of the cavity, a slide projector illuminates this cross-section of the cavity.

[1] The quotient can also be written as $((\partial\sigma/\partial T)\ \nu)\ /\ (Bo\ \kappa\ \sigma\ \beta)$ in which the Bond number, defined by $Bo = (\rho\ g\ L^2)\ /\sigma$ indicates the relative importance of gravitation and surface tension. However, the quotient of thermocapillary to buoyancy convection is independent of the absolute value of σ.

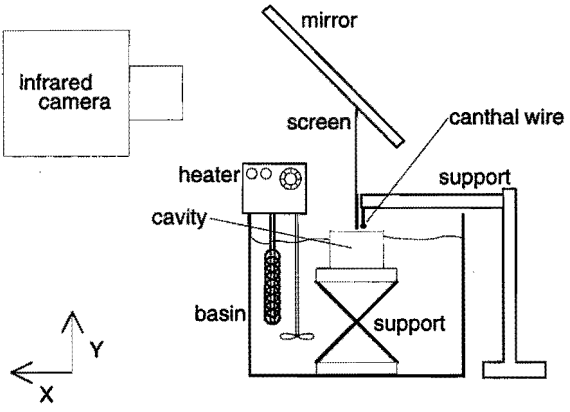

Figure 4.3: Schematic of test rig.

4.2.2 Temperature profile measurements

Measuring temperature profiles of interfaces can be performed by intruding the fluid or by optical methods. Examples of the first are hot wire techniques, thermocouples, thermometers and Pt-100 elements. Disadvantages of these methods are that the measurements disturb the flow and that the measurements are only pointwise. Furthermore, positioning of a probe at an interface is hard. Optical methods do not have these disadvantages. They do not affect the flow and give information over the temperature field. Focussing on the surface is easy. Four classes can be distinguished for this method:

- deflectometry
- interferometry
- reflectometry
- total or spectral radiation methods

It is beyond the scope of this thesis to describe them all in detail, so only their main characteristics are highlighted.

Deflectometry is the technique in which refraction of light due to a gradient in the temperature field is visualized. Examples are the Schlierenmethod and Shadowgraphy. Interferometry is characterized by interference of monochromatic beams which have travelled different paths. The difference in resulting fringes is a measure for the temperature field. Examples are Mach-Zehnder, see [18], and holographic interferometry. Reflectometry is based on the selective reflection property of Thermosensitive Liquid Crystals (TLCs). Properties as birefringence (or double refractive when the propagation velocity of light in the material is dependent on the polarization of light), optical activity (when light experiences a continuous rotation if it propagates along the optical axis of a material) and angle dependency (when at different viewing angles the reflected light corresponds to different angles of incidence and thus to different wavelength) of TLCs must be considered as a light beam reaches them, see [43]. Total or spectral radiation methods register electromagnetic energy radiated by an object, which is a measure for its temperature. Examples are infrared-scanners and pyrolasers. For measuring the temperature at opaque surfaces these techniques are appropriate. An infrared camera is a converter that absorbs IR energy and converts it to a signal, usually an electrical voltage or current. There are two principal types: Thermal detectors and photon detectors. Thermal detectors have been conceived on the notion of the temperature rise produced in an absorbing receiver, such as the pyroelectric detector. The output signal remains practically constant over a wide range of wavelengths for these

detectors. A drawback is their comparatively slow response to radiation variations, due to the thermal processes involved. Photon detectors are more sensitive and have a much shorter response time than thermal detectors (shorter than a microsecond). All photon detectors are composed of semiconductor material, in which the release or transfer of charge carriers (e.g. electrons) is directly associated with photon absorption. Drawbacks are that they also have a limited spectral response and that they require cooling for optimum sensitivity. The energy of the photon E in Joules is inversely proportional to the wavelength λ associated with it, i.e.:

$$E = \frac{h\,c}{\lambda} \tag{4.1}$$

with c the light velocity, 3.0×10^8 m/s and h Planck's constant, 6.6×10^{-34} J/s. The disappearance of photoelectric activity of wavelength longer than the "cut-off" wavelength indicates the energy of the photons to be insufficient to set electrons free. That is, the photons must exceed the so-called "forbidden energy gap" in the semiconductor material. In general, the width of the forbidden energy gap decreases by cooling, so that the cut-off wavelength is decreased when the detector is cooled. Two types of photon detectors are of interest: photoconductive and photovoltaic detectors. In both detectors the gap is determined by the nature of the material itself. The effect of photon absorption is to increase the detector's conductivity. In photovoltaic detectors the charge carriers are swept away by the electric field in a p-n junction, thereby directly producing a voltage instead of a change in conductivity. In appendix E the infrared-camera is described in more detail since it is used in the experiments described in this thesis.

Accuracy

Prior to the experiment, the camera is focussed on the interface and distances are calibrated on the images. This is done using a thin metal wire in a liquid nitrogen bath. This cold wire produces a very sharp thermal image. The image coordinates of the edges of the cavity are then determined by pointing out the boundaries of the cavity with the cold wire. Once the camera has been set up correctly, it was not repositioned or refocused.

The sensitivity of the camera corresponds to the full measuring interval (bandwidth). The sensitivity interval is divided in 256 steps, so-called intensity-values, numbered from 0 to 255. These values are registered by a computer. It is obvious that measuring a small interval results in a high resolution since each of the 256 steps covers a larger temperature range if a larger measuring interval is used. The absolute position of this interval can be altered using the "Picture-Black-Level"-setting on the camera. This level must be exactly in the right position otherwise the measurements can only use a part of the total range of the intensity values from 0 or 255. Once the calibrations are made the PBL-setting may not be altered for the actual experiments. Each image contains 120 pixels in x-direction and 128 pixels in z-direction

Calibration

Calibration is necessary to be able to link the intensity-values to the absolute temperature. For this a calibrated Pt-100 temperature gauge has been placed in the liquid close to the interface. The Pt-100 element is calibrated against a calibrated thermometer with an accuracy of 0.1 $^\circ C$. The water basin is heated up slowly by stirring the mixer, which in turn heats up the liquid in the cavity gradually. At different well-established temperatures, data from both the infrared camera and the Pt-100 element are collected. The Pt-100 element measures locally. To increase the accuracy the infrared camera averages the intensity-values over a square of 8×8 points positioned over the part of the interface where the Pt-100 element where is measures the temperature. The intensity-values from the infrared

camera are in this way related to the actual temperature as recorded by the temperature gauge. A third-order polynomial is used to describe the relation between the intensity-values of the camera and temperature. This polynomial is used in the software to analyze the data.

Measuring procedure

For each experiment, the basin is filled with water. N-paraffin $C_{10} - C_{13}$ is put in the cavity and the tracers are added. The infrared camera is focussed at the interface. The video camera is focused at a cross-section perpendicular to the z-axis in the centre of the cavity, see Fig. 4.3. The water in the basin is stirred by means of a mixer. An experiment is started by turning up the voltage over the canthal wire to the required level. At the same time the computer program is started and thermal images are recorded and the video camera is started. The video images contain the time during recording. Since the time between two successive images of the infrared camera is known, results from the computer and the video are easily matched. Each measurement lasts at least three minutes.

4.2.3 Velocity measurements

The velocity pattern in the liquid is visualized from aside using the suspended silvercoated microballoons with matched density and the video-camera, see section 4.2.1. The camera is adjusted on manual with shutter time 2 ms and is manually focussed on the middle section of the cavity. The velocity of the particles is determined from video images on a television screen and is because of the smallness of the tracers a direct measure of the velocity of the liquid. Only velocities near the interface are measured since the driving force is most active there. Velocities are determined along two x-paths not too close to the wire at times when at $z = 60$ (in midplane of cavity where the light sheet is present) nearly constant velocities are established, so $u = \Delta x/\Delta t$. The time interval is determined with a stopwatch. This procedure is preferred above counting images to estimate the time, since the accuracy is similar (it is hard to detect the exact image at which particles pass a line) and it is less time consuming.

4.2.4 Surface tension measurements

Several methods are available for measuring the surface tension as a function of the temperature. In general they can be divided in two groups:

- methods using the interface
- methods using the bulk of the fluid

Examples of the first are the Wilhelmy plate and the du Noüy ring. These techniques are sensitive to contamination of the interface and adjustment at different temperatures is difficult. The maximum-bubble-pressure method belongs to the second group. Contamination has little effect since the bulk is less affected by contamination and since the interface of the bubble is renewed every few seconds. Furthermore, the temperature of the bulk fluid is easier to control than that of the interface, so it is better suited for our purposes. In appendix F the Sensadyne 6000 surface tension meter which is based on this method and used in our experiments is described .

The surface tension must be determined at a number of temperatures. Therefore the temperature of the liquid is controlled by a water bath and measured with a temperature probe with accuracy of 0.1 °C. The apparatus is calibrated by using two standard liquids for which at a set of temperatures the exact values of the surface tension of the liquid/air interface are known from literature: ethanol and water. At this same set of temperatures the surface tension of n-paraffin $C_{10} - C_{13}/air$ is measured. The surface tension of n-paraffin $C_{10} - C_{13}/air$ at an arbitrary temperature is determined

by linear inter/extrapolation of the measured values. The relation between the surface tension and the temperature for n-paraffin $C_{10} - C_{13}$ measured at 7 different temperatures is given with a 95% accuracy interval by: $\sigma = (27.1 \pm 0.2) - (0.098 \pm 0.005)\, T$, with σ in mN/m and T in °C. $\partial\sigma/\partial T$ is negative which means that the surface driving forces generate motion from the hot to cold positions.

4.3 Results

The test rig described in section 4.2 is used for the experiments. For different experiments the results are analyzed. Specifications of each experiment are given in table 4.1.

exp. nr.	code	voltage [V]	bandwidth [°C]	initial temp [°C]
1	0707951	40	13.2	30
2	1007951	30	16.2	30
3	1407955	40	10.4	30 ± 1
4	1407956	40	10.4	30 ± 1

Table 4.1: Specifications of analyzed experiments. Bandwidth is the measuring interval which can be detected by the camera.

In section 4.3.1 the temperature gradient is described and in section 4.3.2 the corresponding velocity field is presented. These results will be analyzed in section 4.3.3

4.3.1 Temperature gradient

At $t = 0$ the fluid has a uniform temperature and the heating starts. The position of the screen is at $x = 0$, the position of the wire is at $x = -8$ mm and the centre of the cavity in z-direction corresponds with $z = 0$. The influence of the heating wire spreads over the entire cavity as time progresses. A typical interface temperature profile at various z-locations of measurement 3 at $t = 65$ s, is shown in Fig. 4.4. The cavity is visible as a rectangle in the middle of Fig.4.4. The lighter the grade of grey, the higher the temperature. The large dark area around the cavity is the relatively cool basin with its surface unheated by the canthal wire. The lighter shades of grey near the bottom of the picture represent the screen. The canthal wire is located in the area covered by the screen.

Fig. 4.5 shows typical temperature gradient histories at $z = 0$ for $0 < x < 38$ mm. It has been found that during the first 90 s the temperature gradient is almost constant, implying a nearly stationary profile. This holds for all cross-sections perpendicular to the heating wire not in close proximity to the walls of the cavity, as shown clearly in Fig. 4.4. Close to the wire, a gradient is difficult to measure since the screen is positioned there. The wire radiates symmetrically which implies that just below the wire the gradient $\Delta\sigma/\Delta x$ must be zero. Since Marangoni convection is dominant during the first period of time attention is paid to the first 90 s of the experiments. Fig. 4.6 shows temperatures profiles along the x-coordinate for several values of z at $t = 65$ s for this experiment. Fig. 4.6 gives intensity-values and the corresponding temperature in °C along the vertical axis. It shows that the temperature over the length of the cavity between $x = 2$ and $x = 28$ mm varies almost linearly. Moreover, both Figs. 4.4 and 4.6 show that temperature profiles are the same at different z-values. Between $x = 28$ and $x = 38$ mm, the liquid is still at the initial temperature at $t = 65$ s, although in due time the temperature will increase also there. The temperature gradient in x-direction is determined in the plane $z = 0$ and parallel to the x-coordinate, since this is the plane in which the flow pattern is visualized.

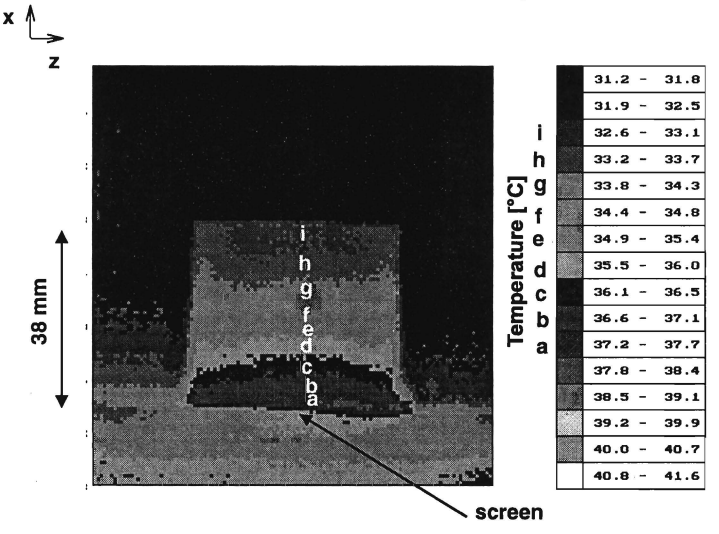

Figure 4.4: A typical temperature distribution on the interface for experiment 3 at $t = 65$ s.

The Pt-100 element used for the calibration has an accuracy of 0.1°C. The calibration function between the temperature (T in °C) and intensity value (H) for this experiment is:

$$T = 31.204 + 0.046\ H - 1.087 \times 10^{-4}\ H^2 + 3.476 \times 10^{-7}\ H^3 \tag{4.2}$$

The largest error made by this function is 0.15 °C. The temperature within a bandwidth of 10 °C can be measured with an accuracy of $10/256 = 0.04$ °C. The total error in measuring the temperature is the sum of the three errors $(0.1 + 0.15 + 0.04)$ and is of order 0.29 °C. The part of the cavity over which the temperature gradient is determined is 38 mm in size corresponding with 55 coordinate intervals in x-direction (105-50, see Figs. 4.6 and 4.4), so each interval measures 0.7 mm. The largest error in the determination of the location z is of the same order, thus 0.7 mm. These errors are determined using the distance calibrations and without changing the position of the camera and without refocusing for the actual experiments. Using the calibration fit, Eq. (4.2), the temperatures at $x = 2$ and 28 are calculated as $T = 38.2$ and 33.8 °C, respectively, so $\Delta T = 4.4 \pm 0.29$ °C. From this it follows that $\partial T/\partial x = 0.16 \pm 0.01$ °C/mm at this time of $t = 65$ s. The error is determined from the relative errors in both the temperature (6.59%) and the distance (1.82%) as: $\sqrt{(6.59)^2 + (1.82)^2} \approx 7\%$.

The temperature gradient is determined for all experiments at various times and various locations of the interface whenever a linear gradient is established, as shown in Fig. 4.6. In appendix H these results are presented. The average temperature gradient measured during the first 90 s for each experiment is given in table 4.2.

Differences in the experiments can be due to variations in adjusting parameters and initial conditions. The former since the Picture Black Level is varied between each experiment and the wire might not have been positioned exactly at the same position with respect to the liquid for each experiment. The latter since the temperature of the liquid and the ambient temperature might be slightly different for each experiment.

Thus, for all coordinates z not in close proximity of the wall (see Fig. 4.6) and for $2 < x < 28$ mm (the linear part) the constant temperature gradient $\Delta T/\Delta x = 0.18 \pm 0.01$ °C/mm during the first 90 s of experiment 3. Only this gradient is of interest since the corresponding velocity is almost steady in this area.

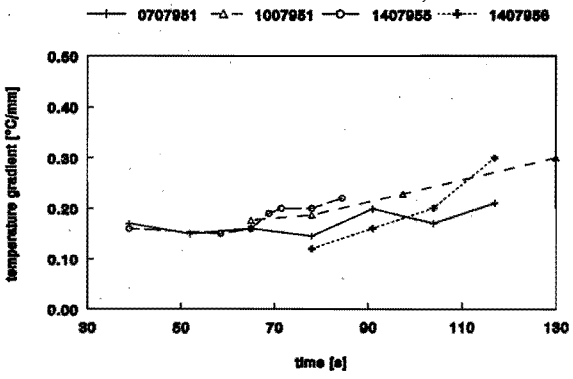

Figure 4.5: Typical temperature gradient histories at $z = 0$ for various values of x. Errors in experiments 0707951, 1407955 and 1407956 are $\pm$ 0.01 °C and in experiment 1007951: $\pm$ 0.03 °C.

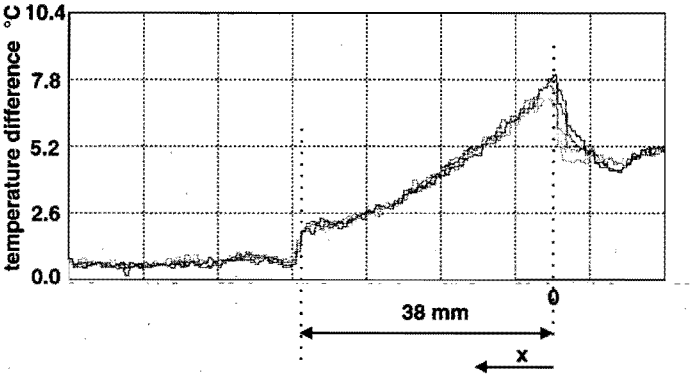

Figure 4.6: Intensity-values and temperature difference against distance x at $t = 65$ s for several cross-sections z of experiment 3 for $z = -15, -7.5, 0$ (centre of cavity), 7.5 and 15 mm.

The experiments show a hardly distorted interface, thus $\partial\sigma/\partial s \approx \partial\sigma/\partial x$ with s the coordinate along the interface. Therefore the surface tension gradient $\partial\sigma/\partial x$ is calculated with:

$$\frac{\partial\sigma}{\partial x} = \frac{\partial\sigma}{\partial T}\frac{\partial T}{\partial x} \tag{4.3}$$

with μ the dynamic viscosity, u the velocity component in x-direction, see Fig. 4.3. From Eq. (4.3) making use of the values for $\partial\sigma/\partial T$ and $\partial T/\partial x$, $\partial\sigma/\partial x$ is found. In table 4.2 these values are given for the experiments.

4.3.2 Flow fields and velocities

The flow field consists of a horizontal flow near the interface away from the heating wire and a return flow in deeper layers between, approximately 4 and 8 mm below the interface. Acceleration is observed in the area close to the heating wire since the temperature gradient is largest there. No flow is seen at depths more than 8 mm below the interface. Significant roll-cells of different sizes are seen: small

exp. nr.	$\Delta T/\Delta x$ [° C/mm]	$\Delta\sigma/\Delta x$ [N/m^2]	average velocity [mm/s]
1	0.17(±0.01)	0.017(±0.001)	1.76(±0.22)
2	0.20(±0.03)	0.020(±0.003)	1.72(±0.21)
3	0.18(±0.01)	0.018(±0.001)	1.43(±0.18)
4	0.14(±0.01)	0.014(±0.001)	1.21(±0.15)

Table 4.2: The average temperature gradient $\Delta T/\Delta x$ ° C/mm, the surface tension gradient $\Delta\sigma/\Delta x$ N/m^2 and surface velocity at $z = 0$ for some experiments during the first 90 s. For each experiment the gradient $\Delta T/\Delta x$ is determined 6 or 4 times, see appendix H.

ones near the wire, large ones over the whole cavity and those in between, see Fig. 4.7. At distances

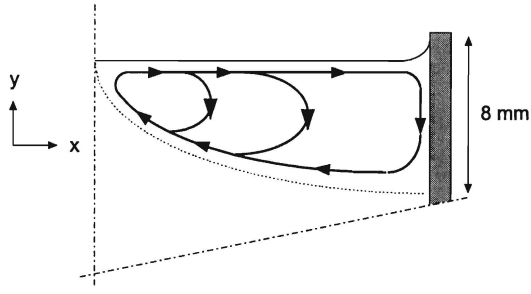

Figure 4.7: Roll-cells of different sizes.

between 2 and 20 mm from the heating wire the velocity at the interface is almost constant with a value to be discussed below.

In appendix G all result of the measurements are gathered. At the interface, velocities are determined along two paths between two sets of vertical lines by measuring the time needed to travel known distances, see section 4.2.3. 38 mm of the cavity corresponds to 370 mm on the screen as measured with a ruler. With this scale the real distances of the two paths are determined on 8.5 and 8.7 mm, respectively. The error due to the accuracy of the ruler and the curvature of the screen is estimated to be 1 mm, 11.8% and 11.5% for the two paths respectively; the error in measuring the time is 0.1 s for switching on and off, so 0.2 s in total in approximately 5 s, yielding 4% in total. The error in the velocity is determined from percentages of the error in both the time and the distance by: $((4.0)^2 + (11.8)^2)^{1/2} = 12.43\%$ and 12.17% respectively. Table 4.2 shows the time-averaged flow velocities determined during the first 90 s of experiments. For experiment 3 the averaged velocity measured between $30 < t < 70$ s over path $2 < x < 10.5$ and path $10.5 < x < 19.2$ mm is 1.43 ± 0.18 mm/s.

4.3.3 Analysis

Since the heating wire is placed above the liquid, a temperature gradient at the interface is established and thermocapillary convection develops. But, inevitably, the bulk of the liquid in the cavity will also be heated up, which results in density differences which in turn invoke buoyancy effects. Since the hottest liquid largely lies on top the latter effect is minimal. An estimate of the influence of buoyancy

convection is described below.

When the wire heats up, liquid particles close to the wire are accelerated along the interface and are observed to reach a constant velocity. The temperature gradient at positions $-8 < x < 2$ mm cannot be measured because the screen is positioned there. This is the part where the strongest acceleration in the liquid occurs. Here measurements of the velocities are prone to large errors, since particles flow quickly and irregularly. Further away from the screen velocities can be determined more accurately. In experiment 3, for example, the velocity at positions $2 < x < 19.2$ mm is 1.43 ± 0.18 mm/s for all z-values. Because of the relatively large magnitude of the velocity, especially near the screen, it is clearly a result of the thermocapillary effect. This effect is a result of a temperature gradient and is expected to be large near the wire and is measured to be constant at positions $2 < x < 19.2$ mm, see Fig. 4.6. These results are very similar to those of Limbourg et al. [35] and Wozniak et al. [38], see table 2.3. Differences in driving forces and resulting flows between their experiments and that of the present investigation are most likely due to differences in liquid and circumstances at which the experiments are performed.

It has been found that a so-called "wedge-shaped" region is formed, in which all elevated temperatures and all induced liquid motion occur. This region is shown in Figs. 4.9 and 4.10. After about three minutes the wedge-shaped region is clearly discernable from the rest of the liquid because of the higher temperature. However it also exists at earlier times as demonstrated by thermocouple measurements. Measurements are performed with thermocouples intruding the liquid to measure the temperature differences in the liquid. In Fig. 4.11 the position of the nine thermocouples is shown. In three layers (y-positions) below the surface the temperature is measured. Putting thermocouples in the liquid interferes with the flow. Since in the end the thermocouples are bent to different z-positions the flow is in z-cross sections disturbed by the thermocouples at one location only. The thermocouples are not irradiated by the heater because of the presence of the screen. Before the experiment starts the thermocouples are put into the cavity. The first temperature, T_1, is registered 30 s after starting heating the liquid. Next, T_2 and T_3 etc. are measured with an interval of 5 s. Every temperature is measured five times and the experiment is repeated four times. Fig. 4.8 shows isotherms of a characteristic measurement, nr. 3, at $t = 70$ s. It shows that the hottest liquid lies on top everywhere and

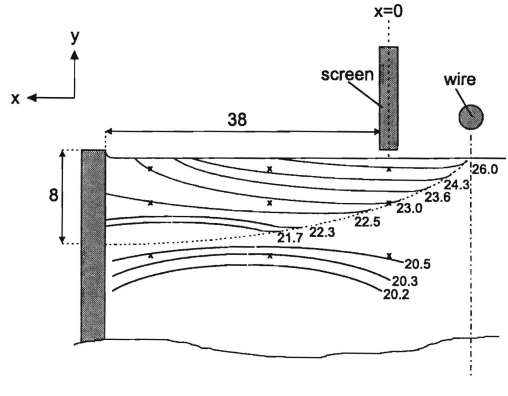

Figure 4.8: Temperature isotherms in liquid layer heated from above of experiment 3.

that in the wedge-shaped region the temperature gradient in y-direction is 5 K maximum of a ± 10 mm thick layer of ± 38 mm length. In appendix I tables are presented in which the temperatures are shown. These temperatures are interpolated at four successive instants in time using the temperature measurements. To investigate the influence of the position of the thermocouples on the flow pattern

measurements are done in the configuration of Fig. 4.12. Three groups of three thermocouples with each thermocouple at a different y-position are used. In this test each group of thermocouples is positioned at a different z-section, i.e. not each others wake and not bend at the end, see Fig. 4.12. In appendix I these results are also presented. The measurements for the two situations turned out to be independent of the configuration of the thermocouples. These measurements provide arguments for the following analysis.

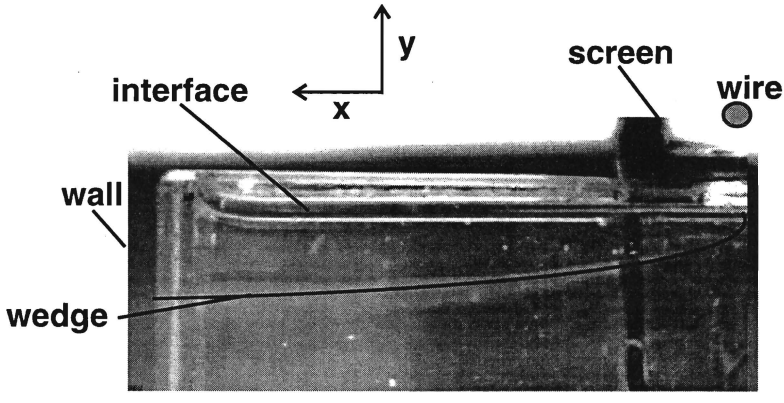

Figure 4.9: Picture of observed wedge-shaped region.

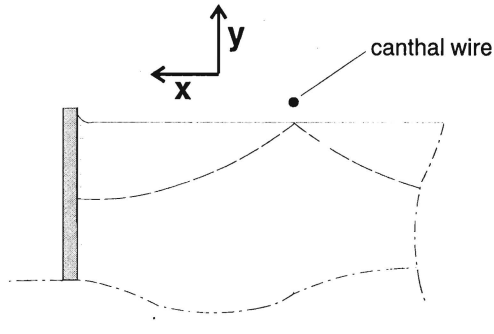

Figure 4.10: Observed wedge-shaped region.

If diffusion of heat from the hottest spot of the surface to other positions would be dominant, the heated liquid would assume a shape as shown in Fig. 4.13. This is because heat diffusion is proportional to the distance. However, a wedge-shaped region as shown in picture 4.9 is observed. Fig. 4.10 is a drawing of the observed pattern. This region with higher temperature diffuses slowly downwards, see appendix I. After about three minutes, the typical vertical dimension of the wedge-shaped region is of the order of 8 mm. Because of the difference of Fig. 4.13 and Fig. 4.10 it is concluded that convection is responsible for the observed shape.

Temperature 1, 2 and 3, i.e. the temperature at the points near the interface, indicate that the temperature increases along the surface, as already observed with the infrared camera. This gradient is largest during the first 90 s. After a while, the convection homogenizes the temperature in deeper layers underneath the interface in a way that temperature $4-6$, see Fig. 4.11, in horizontal direction differ only $\pm$ 2.0 °C over 10 mm (see appendix I). In vertical direction the hottest liquid layers are on top. Pure buoyancy effects are therefore negligible in the wedge-shaped region. Temperature $7-9$,

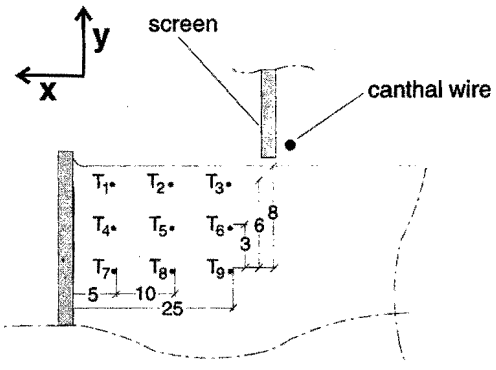

Figure 4.11: Thermocouple positions (in mm) of situation 1.

see Fig. 4.11, are lower because these measuring-points lie below the wedge-shaped region. Consider a horizontal line over the entire cavity from the wedge to the region below the wedge, f.e. the line $T_4 - T_5 - T_6 \ldots$. Then the temperature in the wedge is nearly the same and relatively warm (f.e. 27.3 $°C$, see experiment 5 at $t = 160$ s for thermocouple 1) and below the wedge the temperature is nearly the same as T_9 and relatively cold (f.e. 22.4 °C, the same experiment at the same time). From the data in appendix I it is clear that the temperature difference between the wedge and the region outside the wedge is initially small and that it increases with time. Since these temperature differences invoke mass density differences the production of circulation by gravity, the so-called baroclinic effect, increases in the area outside the wedge as indicated by the cross product $\nabla(1/\rho) \times \nabla p$. This cross product equals zero when the vectors $\nabla(1/\rho)$ and ∇p are aligned. When this is not the case, as in the area outside the wedge, secondary buoyancy flows are established. Fig. 4.14 schematizes this effect with the corresponding flow circulation. It is concluded that the established flow in the wedge-shaped region during the first period of $t < 90$ s is dominated by the thermocapillary effect.

Results obtained with glycerol ($C_3H_8O_3$) instead of n-paraffin $C_{10}-C_{13}$ confirm the above analysis. No liquid motion was established, so convection is absent. Only diffusion of heat can therefore take place. Temperature measurements, see table I.10, show similarity to the ones with n-paraffin, see table I.6 to table I.9. isotherms similar to those shown in Fig. 4.8 and a wedge-shaped region, as expected for diffusion-cases, are established, see Fig. 4.13. This is easily explained as follows. The thermal diffusivities for n-paraffin $C_{10} - C_{13}$ and glycerol are nearly equal, so a similar wedge-pattern is expected. However the viscosity of glycerol is almost 1000× larger ($\mu = 1.2 \times 10^{-3}$ m^2/s) than that of n-paraffin $C_{10} - C_{13}$. Therefore, a surface tension gradient hardly induces liquid motion in glycerol. This means that diffusion of heat into this liquid is not disturbed by thermocapillary convection.

A second confirmation is found with water measurements. Again no liquid flow is established and only diffusion can take place. The measurements confirm this since the same temperature field, in which diffusion is the dominant factor is established, see table I.11. In this case it is not the viscosity ($\mu = 1.002$ Pas) that inhibits the liquid flow since it is nearly the same as for n-paraffin $C_{10} - C_{13}$. However, water is very susceptible to contamination, and only slight contamination inhibits Marangoni convection to be established. n-paraffin $C_{10} - C_{13}$ is not susceptible to contamination and Marangoni convection can occur. This is a phenomena well known from literature, see [27][44]. Kao et al. [44] investigated that Marangoni convection can only be investigated when water is not contaminated. Nengli Zhang et al. [27] confirm this as powder contamination to visualize flows suppresses the surface tension flows. The cavity always contains contamination, so in this configuration Marangoni convection in water can not be investigated. In chapter 6 of this thesis Marangoni flows are visualized in a small droplet of clean water on a clean plate.

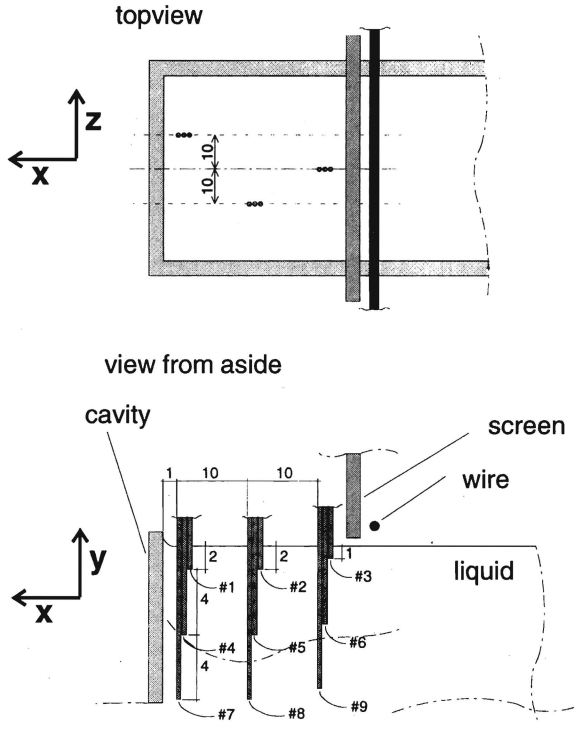

Figure 4.12: Thermocouple positions (in mm) of situation 2.

It can be concluded that the wedge-shaped region in n-paraffin $C_{10} - C_{13}$ is due to convection. In the wedge-shaped region the motion is mainly due to thermocapillarity.

4.4 Conclusions

The temperature gradient at the interface of a layer of n-paraffin $C_{10} - C_{13}$ heated from above is measured with an infrared camera. For various experiments the resulting thermocapillary flows at the interface are visualized and analyzed. Measurements of the surface tension of $C_{10} - C_{13}/air$ at various temperatures are performed resulting in a gradient of $\Delta\sigma/\Delta T = -9.8 \times 10^{-5}$ N /(mK). During the first 90 s buoyancy effects are negligible and the thermocapillary effect dominates. Nearly stationary flows are established with an almost homogeneous surface tension gradient. The influence of the side-walls is found to be negligible and the same flows in each cross-section perpendicular to the wire are established. Particles assume a constant velocity at the interface after being accelerated away from the heating wire and return in deeper layers. A characteristic constant driving force of $\Delta\sigma/\Delta x = 0.018 \pm 0.001$ N/m^2 at the interface results in an averaged constant velocity of 1.43 ± 0.18 mm/s. These experimental data are used for the validation of the numerical method of chapter 2.

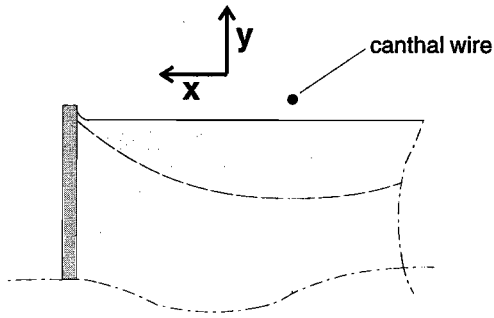

Figure 4.13: Expected wedge-shaped region.

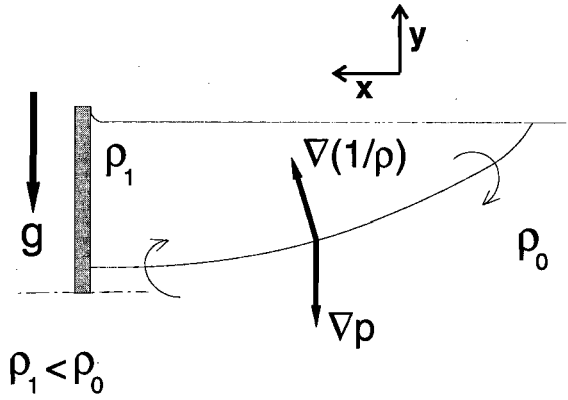

Figure 4.14: Baroclinic effect.

Chapter 5

Thermocapillary convection of an axisymmetrical droplet

5.1 Introduction

In chapter 2 two-dimensional Marangoni flow in a rectangular cavity has been numerically simulated with a new approach. The present chapter presents a computational method for numerically simulating Marangoni flows in axisymmetrical droplets [45], such as those experimentally investigated in chapter 6. The method is based on the same approach as described in chapter 2.

Thermocapillary convection has been studied often, [4][11][27][46][30][45][47], either experimentally or numerically. Marangoni flows and interface motion in droplets condensing on plastic condenser plates are particularly interesting since they might affect the heat resistance of droplets [1], see chapter 1. Thermocapillary Marangoni convection is induced when at the interface a temperature gradient exists [46]. In the present case a temperature gradient exists because at the top of a condensing droplet the temperature is higher than at the bottom, see chapter 6. Petri et al. [4] numerically investigated Marangoni convection in spherical coordinates using the vorticity transport equation and a stream function. Zhang et al. [27] and Su et al. [47] observed flow patterns in evaporating droplets with and without cooling at the bottom of the droplet. Hoefsloot [11] both numerically and experimentally describes Marangoni convection in water in which acetone diffuses.

To compute the flow a system of partial differential equations with initial and boundary conditions has to be formulated and solved. The algorithm to be described below describes the time evolution of thermocapillary convection induced at dynamic interfaces. It accounts for the prescribed stress conditions at the free boundary, solves all equations simultaneously and is based on the collocation method. An adapted Singular Value Decomposition is introduced to tune the significance of the tangential stress condition.

In section 5.2 the problem statement, the physical model and the governing equations are described. The solution procedure is described in section 5.3. In chapter 7, simulation results are discussed with realistic profiles derived from experiments, described in chapter 6.

5.2 The droplet problem

In this section the droplet problem is considered. An application of this configuration is a droplet condensing on a plate, see section 5.1. The problem statement and physical model are described in section 5.2.1, the governing equations that form the basis for the numerical algorithm are given in section 5.2.2.

5.2.1 Problem statement and physical model

The considered droplet has a convex axisymmetrical shape. The used coordinate system is the spherical (r, θ, φ) one, see Fig. 5.1. The model is based on the right half of a cross-section through half the droplet as depicted in Fig. 5.1.

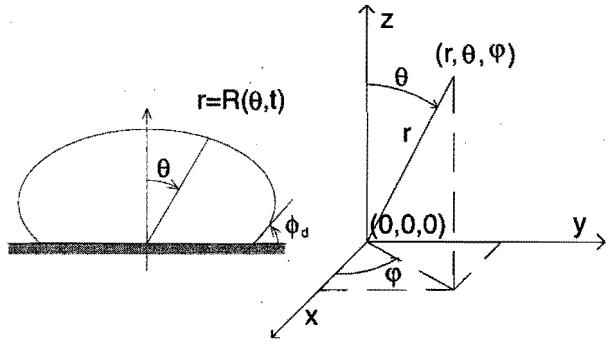

Figure 5.1: Spherical coordinate system and the cross-section used to depict the flow field.

Assumptions of the physical model are:

1. The flow in the droplet is incompressible and laminar with dynamic viscosity μ, which is assumed constant: it is assumed that evaporation can be neglected.

2. The flow is axisymmetric, i.e. $u = u(r, \theta, t)$ and the droplet is given by $r = R(\theta, t)$.

3. The free interface is allowed to deform due to stresses at the air/liquid interface.

4. The initial shape is hemispherical.

5. The velocity in φ-direction is zero, i.e. $u_\varphi = 0$.

6. Symmetry exists at $\theta = 0$, so $u_\theta(r, 0, t) = 0$ and only the right half of the hemispherical droplet is considered.

7. The bottom of the droplet is assumed to rest on a flat plate and the no-slip condition, $u_r = 0$ at $\theta = \pi/2$, is assumed to be valid for $r \leq R(\pi/2, t)$. The dynamic contact angle ϕ_d at $\theta = \pi/2$ satisfies the condition: $(\phi_d)^\epsilon = (\mu u_t)/\sigma$, with u_t the velocity of the line of contact between the liquid (water), the plate and the ambient air, see [48]. $(\mu u_t)/\sigma$ is called the capillary number. In the simulations usually $\epsilon = 2$.

8. At the plate $(\theta = \pi/2)$ is $u_\theta(r, \pi/2, t) = 0$.

9. The tangential stress at the free interface is prescribed and varies in time and position on the interface. Since now the temperature is not needed the energy equation is decoupled and does not need to be solved unless one is interested in the temperature distribution within the droplet.

10. It is assumed that the viscosity of the gas is negligible as compared to that of the liquid.

5.2.2 Governing equations

The continuity equation for an incompressible flow reads [1]:

$$\frac{1}{r}\frac{\partial}{\partial r}\left(r^2 u_r\right) + \frac{1}{\sin\theta}\frac{\partial}{\partial\theta}\left(u_\theta \sin\theta\right) = 0 \tag{5.1}$$

The Navier-Stokes equation in θ and r-direction are respectively:

$$\frac{\partial p}{\partial \theta} = -r\rho\left(\frac{\partial u_\theta}{\partial t} + u_r\frac{\partial u_\theta}{\partial r} + \frac{u_\theta}{r}\frac{\partial u_\theta}{\partial \theta} + \frac{u_r u_\theta}{r}\right) + r\mu\left(\nabla^2 u_\theta + \frac{2}{r^2}\frac{\partial u_r}{\partial\theta} - \frac{u_\theta}{r^2\sin^2\theta}\right) \tag{5.2}$$

$$\frac{\partial p}{\partial r} = -\rho\left(\frac{\partial u_r}{\partial t} + u_r\frac{\partial u_r}{\partial r} + \frac{u_\theta}{r}\frac{\partial u_r}{\partial\theta} - \frac{{u_\theta}^2}{r}\right) + \mu\left(\nabla^2 u_r - \frac{2}{r^2}u_r - \frac{2}{r^2}\frac{\partial u_\theta}{\partial\theta} - \frac{2}{r^2}u_\theta\cot\theta\right) \tag{5.3}$$

with:

$$\nabla^2 = \frac{1}{r^2}\frac{\partial}{\partial r}\left(r^2\frac{\partial}{\partial r}\right) + \frac{1}{r^2\sin\theta}\frac{\partial}{\partial\theta}\left(\sin\theta\frac{\partial}{\partial\theta}\right) \tag{5.4}$$

and ρ the mass density of the liquid. The normal stress condition at the interface reads:

$$\frac{-1}{R_s}\left\{\left(\mu\frac{\partial u_r}{\partial r}\right)\left(-R_m\cos 2\theta + 2R_p\sin 2\theta + R_s\right) + \mu\left(\frac{\frac{\partial u_r}{\partial\theta}}{R} - \frac{u_\theta}{R} + \frac{\partial u_\theta}{\partial r}\right)\times\right.$$
$$\left.\left(-R_m\sin 2\theta - 2R_p\cos 2\theta\right) + \mu\left(\frac{\frac{\partial u_\theta}{\partial\theta}}{R} + \frac{u_r}{R}\right)\left(R_m\cos 2\theta - 2R_p\sin 2\theta + R_s\right)\right\}$$
$$+p_{li} - p_g = \sigma\left(\frac{1}{R_1} + \frac{1}{R_2}\right) \tag{5.5}$$

with:

$$R_m \stackrel{\text{def}}{=} \left(\frac{\partial R}{\partial\theta}\right)^2 - R^2 \qquad R_s \stackrel{\text{def}}{=} \left(\frac{\partial R}{\partial\theta}\right)^2 + R^2$$
$$R_p \stackrel{\text{def}}{=} R\frac{\partial R}{\partial\theta}$$

and

$$R_1 = \frac{\left(\left(\frac{\partial R}{\partial\theta}\right)^2 + R^2\right)^{\frac{3}{2}}}{\left(R^2 + 2\left(\frac{\partial R}{\partial\theta}\right)^2 - R\frac{\partial^2 R}{\partial\theta^2}\right)} \tag{5.6}$$

$$R_2 = \frac{R^3\left(1 + \left(\frac{\partial R}{\partial\theta}\right)^2\frac{1}{R^2}\right)^{1/2}}{\left(R^2 - R\frac{\partial R}{\partial\theta}\cot\theta\right)} \tag{5.7}$$

The tangential stress condition is given by:

$$\frac{\mu}{R}\left\{\left(R\frac{\partial u_r}{\partial r} - \frac{\partial u_\theta}{\partial\theta} - u_r\right)\left(R_m\sin 2\theta + 2R_p\cos 2\theta\right) + \left(-u_\theta + R\frac{\partial u_\theta}{\partial r} + \frac{\partial u_r}{\partial\theta}\right)\times\right.$$
$$\left.\left(2R_p\sin 2\theta - R_m\cos 2\theta\right)\right\} = \left(\cos\theta\frac{\partial\sigma}{\partial r} - \sin\theta\frac{\frac{\partial\sigma}{\partial\theta}}{R}\right)\left(\frac{\frac{\partial R}{\partial\theta}\sin\theta + R\cos\theta}{\sqrt{R_s}}\right) \tag{5.8}$$

$\frac{\partial\sigma}{\partial\theta}$ and $\frac{\partial\sigma}{\partial r}$ are the surface tension gradients along the interface in the θ- and r-direction, respectively.
The time evolution of the interface is computed with the aid of the kinematic boundary condition:

$$\frac{\partial R}{\partial t} = u_r - u_\theta\frac{1}{R}\frac{\partial R}{\partial\theta} \tag{5.9}$$

In the present method the equations are not made dimensionless as done in chapter 2.

[1] $u_\theta(r,\theta,t)$, $u_r(r,\theta,t)$ and $R(\theta,t)$ are in other parts of this thesis abbreviated as u_θ, u_r and R respectively.

5.3 Numerical solution

Instead of dividing the geometry of Fig. 5.1 in elements, as done in FEM, a type of spectral collocation method is used with expansions containing time-dependent coefficients that contain the time evolution of the Marangoni flow. A mesh in θ-direction of "a cross-sectional region through the droplet" is chosen at equidistant angles to weight each part of the region equally. Radial locations, r_i, are chosen in such a way that $c_i = r_i/R$ is constant at all times. Here i numbers the discrete points in radial direction. n_k points exist for every c_i value. The points of intersection in θ- and r-direction are taken as the collocation points. The mesh of collocation points is shown in Fig. 5.2.

In section 5.3.1 the velocity and interface expansions are presented. The contour integrals, see section 5.3.2, and the tangential stress condition at the interface, see section 5.3.3, yield the governing equations of the numerical method. The SVD technique to weight these equations is described in section 5.3.4. The computation of the interface is described in section 5.3.5.

5.3.1 Expansions

For the velocity in θ-direction, u_θ, the following expansion is selected:

$$u_\theta(r,\theta,t) = \sum_{i=0}^{n_{ic}-1} \sum_{k=0}^{n_{kc}-1} a_{i,k}\, \theta^{k+1} \left(\frac{r}{R}\right)^{i+1} (\pi/2-\theta)^{\epsilon+1} \tag{5.10}$$

The $a_{i,k}$-coefficients are time-dependent. A polynomial series in θ is chosen because it is an orthonormal basis. Also, in radial-direction a polynomial, in terms of r/R, is used. Because of symmetry, $u_\theta(r,\theta,t) = 0$ at $\theta = 0$ and $\theta = \pi/2$ which is automatically fulfilled by the expansion 5.10. n_{kc} is the number of polynomial θ-elements for constant r, n_{ic} gives the number of elements of the (r/R)-polynomial expansion for constant θ.

The velocity in r-direction, u_r, is derived by integration of the continuity equation, Eq. (5.1) from $r = 0$, where $u_r = 0$, with respect to r. This yields

$$u_r(r,\theta,t) = \sum_{i=0}^{n_{ic}-1} \sum_{k=0}^{n_{kc}-1} \frac{a_{i,k}}{i+3} \left\{ \theta(1+\epsilon) - (k+1)\left(\frac{\pi}{2}-\theta\right) + (i+1)\theta \frac{1}{R}\frac{\partial R}{\partial \theta}\left(\frac{\pi}{2}-\theta\right) - \theta\, \mathrm{ctg}\theta \left(\frac{\pi}{2}-\theta\right)\right\} \theta^k \left(\frac{\pi}{2}-\theta\right)^{\epsilon} \left(\frac{r}{R}\right)^{i+1} \tag{5.11}$$

The no-slip condition $u_r = 0$ at $\theta = \pi/2$, see section 5.2, is automatically fulfilled by Eq. (5.11). From these velocity expansions, all derivatives with respect to θ and r are analytically computed and used in the method. For the time-dependent expansion for R use is made of the fact that the volume of the droplet is constant. For R a series is selected based on cubic splines:

$$R(\theta,t) = \sum_{m=0}^{m=n_k+3} b_m \tau_m(\theta) \tag{5.12}$$

with:

$$\begin{aligned} &\tau_m(\theta) = \theta^m && \text{for } m = 0,1,2,3 \\ &\tau_m(\theta) = (\theta-\theta_{m-3})^3 && \text{for } \theta > \theta_{m-3} \text{ and } m = 4,\ldots,n_k+3 \\ &\tau_m(\theta) = 0 && \text{for } \theta < \theta_{m-3} \text{ and } m = 4,\ldots,n_k+3 \end{aligned} \tag{5.13}$$

The coefficients b_m are time-dependent. With θ_{m-3} the $(m-3)^{th}$ collocation point is meant. As upper limit $n_k + 3$ is chosen since the interface is divided in $n_k + 4$ collocation points. In this way the interfacial radial distance and first derivatives with respect to θ of the interface description are continuous at all points. Symmetry at $\theta = 0$ is fulfilled, i.e. $\partial R/\partial\theta = 0$, since $b_1 = 0$.

5.3.2 Contour integrals

A closed contour integral of the momentum equation is evaluated for each collocation point. The contour starts at the collocation point P_2, see Fig. 5.2, proceeds to the nearest collocation point in positive θ-direction along the contour at constant c_i-value, P_3, from that collocation point to the interface keeping θ constant, position P_4, then crosses the interface into the gas, position P_0, in the gas to a position with the same value for θ as the collocation point where the contour was started, crosses the interface again into the liquid, position P_1, and finally into the liquid to P_2 again. The

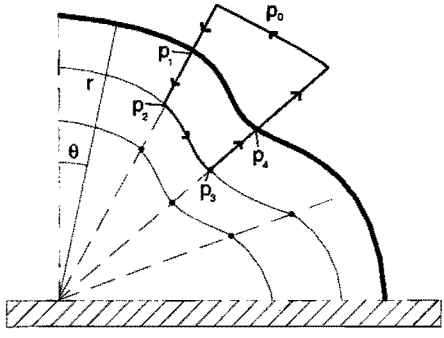

Figure 5.2: Schematic of closed contour integral.

pressure drop over a closed contour is zero:

$$(p_0 - p_1) + (p_1 - p_2) + (p_2 - p_3) + (p_3 - p_4) + (p_4 - p_0) = 0 \tag{5.14}$$

which is used to derive equations for $\partial u_r/\partial t$ and $\partial u_\theta/\partial t$. For $(p_1 - p_2)$, $(p_2 - p_3)$, and $(p_3 - p_4)$ the following expressions hold:

$$(p_1 - p_2) = \int_{r=c_i R}^{r=R} \frac{\partial p}{\partial r}\, dr \tag{5.15}$$

$$(p_2 - p_3) = \int_{\theta=\theta_{i+1}}^{\theta=\theta_i} \left(\frac{\partial p}{\partial \theta} + c_i \frac{\partial R}{\partial \theta} \frac{\partial p}{\partial r} \right) d\theta \tag{5.16}$$

$$(p_3 - p_4) = \int_{r=R}^{r=c_i R} \frac{\partial p}{\partial r}\, dr \tag{5.17}$$

For the terms containing $\partial p/\partial \theta$ and $\partial p/\partial r$ the Navier-Stokes equations are substituted. All integrals appearing in $(p_1 - p_2)$, $(p_2 - p_3)$, and $(p_3 - p_4)$ are evaluated numerically using a fourth-order Simpson-rule, given by:

$$I \overset{def}{=} \int_{x=x_1}^{x=x_2} f(x)\, dx \tag{5.18}$$

$$\approx \frac{h}{3} \left[f(x_1) + 4f(x_1 + h) + 2f(x_1 + 2h) + 4f(x_1 + 3h) + 2f(x_1 + 4h) \right. \tag{5.19}$$

$$\left. + \ldots + 2f(x_1 + (n-2)h) + 4f(x_1 + (n-1)h) + f(x_1 + nh) \right] \tag{5.20}$$

$$= S(h) \tag{5.21}$$

with the considered interval divided in n parts of stepsize h. $S(h)$ is called the Simpson-approximation for integral I.

The normal stress boundary condition, Eq. (5.5), is used to eliminate $(p_0 - p_1)$ and $(p_4 - p_0)$. In this way all terms in Eq. (5.14) are evaluated, which results in a matrix equation:

$$\underline{\underline{B}}\underline{a}' = \underline{s} \tag{5.22}$$

The left-hand side encompasses the $\partial p/\partial\theta$ and $\partial p/\partial r$ terms. The right-hand side contains the other velocity terms substituted in Eq. (5.14). The vector $\underline{a}'$ contains the time-derivatives of the $a_{i,k}$-coefficient of Eq. (5.10). [2]

5.3.3 Tangential stress condition

Since the tangential stress condition is the driving force of the Marangoni convection, Eq. (5.8) is accounted for in a specific way in the numerical algorithm, i.e. by determination of the significant singular values of the matrix equation resulting from application of condition 5.8, see section 2.3.4 and appendix B:

$$\underline{\underline{A}}\underline{a} = \underline{q} \tag{5.23}$$

The left-hand side encompasses the velocity term and derivatives with respect to θ and r, the right-hand side contains the surface tension gradient. Eq. (5.22) is combined with Eq. (5.23) in the numerical algorithm of the next section 5.3.4.

5.3.4 Singular Value Decomposition

Consider three time levels: the old time, index "old", the present time, index "pre" and the new time, without index. Two sets of equations result that have to be solved simultaneously, namely the $(n_k \times n_i)$ equations formed by the contour integrals (in matrix form $\underline{\underline{B}}\underline{a}'_{pre} = \underline{s}$, see Eq. (5.22)) and the n_k equations obtained from the tangential stress condition, Eq. (5.8), at the interface (in matrix form $\underline{\underline{A}}\underline{a} = \underline{q}$, see Eq. (5.23)). At the present time the coefficients $a_{i,k_{old}}$, $a_{i,k_{old}}$ and $a_{i,k_{pre}}$ are known, and $a_{i,k}$ is to be calculated.

The number of unknowns is first reduced by expressing the coefficients $a_{i,k_{pre}}$ in $a_{i,k}$ and $a_{i,k_{pre}}$ using a second-order Adams-Bashford integration:

$$a'_{i,k_{pre}} = \frac{1}{3}\left(\frac{2}{\Delta t}\left(a_{i,k} - a_{i,k_{pre}}\right) + a'_{i,k_{old}}\right) \tag{5.24}$$

Substitution of (5.24) in $\underline{\underline{B}}\underline{a}'_{pre} = \underline{s}$ results in a matrix equation of the form $\underline{\underline{C}}\underline{a} = \underline{p}$.

The matrix-equations $\underline{\underline{A}}\underline{a} = \underline{q}$ and $\underline{\underline{C}}\underline{a} = \underline{p}$ are joined into a "grand" matrix equation $\underline{\underline{D}}\underline{a} = \underline{r}$ and simultaneously solved using a matrix solver based upon Singular Value Decomposition, see section 2.3.4. The solution-vector contains the $a_{i,k}$-coefficients at the new time level. The terms in the important "grand" matrix, which contains the driving force of the process, are weighted by weighting the singular values. This method computes the $a_{i,k}$-coefficients in a way which almost exactly meets the tangential stress condition at minimum loss in accuracy of the equations stemming from the contour integrals, i.e. the (integrated) Navier-Stokes equations.

In this way, the $a_{i,k}$-coefficients for the new time level are derived.

[2] The $a_{i,k}$-coefficients are the elements of a $(n_{kc} \times n_{ic})$-matrix with columns $a_{i,0}, a_{i,1}, \ldots, a_{i,n_{kc}-1}$. Vector a is defined as $a = ({a_{i,0}}^T, {a_{i,1}}^T, \ldots, {a_{i,n_{kc}-1}}^T)^T$.

5.3.5 Computation of interface deformation

The b_m-coefficients of expansion 5.12 are found in the following way. At the present time level, the velocities, the interface contour and the derivative with respect to θ of this contour are known. The right-hand side of Eq. (5.9) is known, so using a second-order Adams-Bashford integration method, see Eq. (5.24), the b_m-coefficients of the new time level and thus the new interfacial height is easily computed.

The time evolution of the velocity field and interfacial height are determined by repeating the steps described in section 5.3.4 and above. Note that no iterations are necessary to obtain the solutions at each time level.

5.4 Conclusions

In this chapter, a numerical method for thermocapillary convection in an axisymmetrical droplet is presented. The method is based on a spectral collocation method and makes use of the contour integrated momentum equation. These integrals yield a matrix equation that is combined with the tangential stress condition at the interface in a SVD solution routine. The interfacial description is based on cubic splines.

With the method, experiments as described in section 6 can be simulated.

Chapter 6

Thermocapillary convection in a droplet cooled from below

6.1 Introduction

In chapter 4, Marangoni convection was experimentally investigated in a thin liquid layer heated from above by a wire, which radiates symmetrically with respect to a vertical plane through the layer. In this chapter, a similar situation but with symmetry around an axis, namely an axisymmetrical droplet resting on a flat plate, is studied. This situation occurs in dropwise condensation on plastic plates of a heat exchanger cooled from the inside [46]. A temperature gradient is induced along the interface of the droplet which causes thermocapillary convection. A set-up is used that encompasses a droplet and a PolyMethylMethAcrylate (PMMA) plate cooled electrically. Just as in chapter 4, buoyancy effects are minimal since the hottest parts in the droplet are on top and the droplet size is relatively small. In Fig. 6.1 a droplet is shown with typical dimensions and the definitions as used in this chapter.

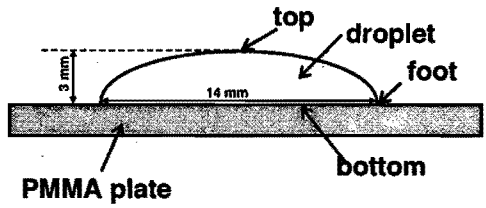

Figure 6.1: Droplet with characteristic values and names.

In water Marangoni convection can only occur if the liquid is not contaminated [27][44]. Kao & Kenning [44], for example, experimentally observed that contamination, which lowers the static surface tension slightly, suppresses thermocapillary motion at a *bubble* interface. The mechanism is as follows. Contamination and/or surfactant are absorbed at the bubble interface to form a surface film. Since desorption and diffusion are slow processes, and any liquid motion near the interface causes a concentration variation of the surfactant with an accompanying surface tension gradient that opposes the motion, a boundary condition of near-zero velocity is established. During condensation, however, water condenses on clean, cold plates and this water does not contain contaminations. This situation is studied in this chapter.

Only few visualization studies of thermocapillary flows in droplets have been found in the literature

[11][27]. Nengli Zhang et al. [27] used a shadowgraph method to visualize the flow pattern, which had better results than their alternative, using a suspension of aluminium particles, that suppressed the surface tension driven flow. They investigated a small droplet that was asymmetrically *heated* from below, thus invoking buoyancy effects. Nengli Zhang et al. visualized a ring of roll-cells due to Marangoni convection near the foot of droplets. They did not measure the temperature gradient along the interface of the droplet and they did not perform measurements with water droplets. Under microgravity conditions Hoefsloot [11] observed that vortices established near the point where the interface is in contact with the solid wall.

The objectives of the present study are:

- to measure the temperature gradient along the interface of droplets that are cooled uniformly from below, in order to quantify the boundary condition for the numerical simulations;
- to visualize the flow pattern in the droplets.

6.2 Experimental set-up

A schematic of the test set-up is shown in Fig. 6.2. It consists of a hemispherical droplet of clean,

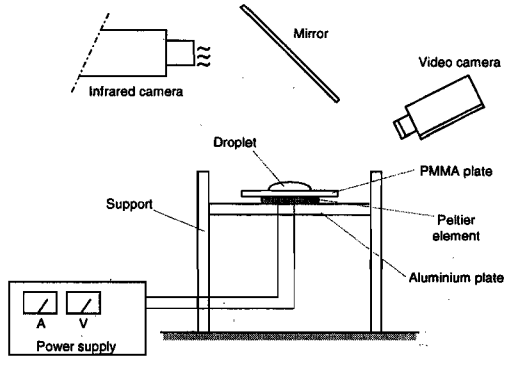

Figure 6.2: Schematic of test set-up.

distilled water with a small amount ($\pm$ 2.5 $\times$ 10^{-4} Vol %) of Liquid Crystals (LCs) and a PMMA plate of $L \times W \times H$, 70 $\times$ 70 $\times$ 8 mm^3. The plate has a heat conductivity κ = 0.19 W/(mK) and a specific heat capacity c = 1300 J/(kgK). The plate is positioned horizontally. The plate is cooled from below by a thermoelectric 'pump', a Peltier element type CP-1.0-127-08L of Melcor, glued onto the plate. This pump extracts heat from the PMMA-plate and transfers it to an aluminium plate of dimensions $L \times W \times H$, 24 $\times$ 10 $\times$ 1 cm^3, with a thermal conductivity of κ = 164 W/(mK) and a heat capacity of c = 880 J/(kgK), which functions as a heat buffer. The Peltier element is connected to a 'Delta'-power supply, and requires a current of 2.5 A (maximum) and a voltage of 15.4 V (maximum). Like in the measurements of two-dimensional motion in a liquid layer of chapter 4, a thermovision system is used to measure the temperature gradient along the droplet. A 'cold' lamp, Dedocool of Dedotec Munich Germany, is positioned at an angle of approximately 45° with the horizontal axes to illuminate the droplet. The lamp is a halogenlamp of 400 W. A built-in fan cools the lamp. Two video recording

systems are used: one camera makes recordings vertically from above the droplet and the other along a line at an angle of 43° with the horizontal. The second video system gives better visualization of the flow pattern inside the droplet. Visualization of the flow in the droplet in horizontal planes is impossible, since hardly any light is reflected in the horizontal plane due to the critical angle of the incoming beam being exceeded, causing the inside of the droplet to be hardly illuminated. A few seconds before the experiment starts the lamp is switched on to ensure that the droplet is not heated up by the radiation. Without cooling, motion was not observed in the droplet, showing that the lamp on its own cannot cause thermocapillary motion. The test liquid is obtained by mixing a small amount ($\pm$ 0.25 ml) of clean LCs into one litre of distilled water. LCs hardly have any effect on, for example, the surface tension of water since they are encapsulated. The mixture is homogeneous and the LCs do not evaporate so no concentration differences occur in the liquid. The particles also do not accumulate near the interface. LCs reflect the light entering from the light source. The density of LCs is equal to that of water, i.e. $\rho \approx 998$ kg/m^3, and their size is ± 100 μm. Distilled water is chosen since it is often the main condensing component in heat exchangers. The material PMMA is selected since the static contact angle of water on PMMA is 92° which corresponds well with the contact angle of condensed droplets on plastic plates used in compact heat exchangers.

6.3 Measurement procedure

Thermocapillary convection is established in water only if it is very clean [27][44]. The following procedure has been applied to cleanse the plate:

- Each element in contact with the test liquid was cleaned first with 96 % ethanol and dried in still air for some seconds so that virtually all ethanol was evaporated.
- The pipet, used for creating the droplets, is washed with the test liquid.
- The tests are performed immediately after cleaning to minimize contamination, e.g. from particles present in the environment.
- The containers which contain the mixture are closed after use.

At least 15 minutes before the tests, the Peltier element is supplied with 9W power, 9 V and 1A, to cool the PMMA plate. The top of the plate attains a temperature of 288.7 ± 0.2 K, measured with a contact thermocouple. The ambient temperature is about 296 K. The liquid is heated in a closed vessel, that rests inside a larger vessel in which also a heating element is placed. The liquid is heated to 303 ± 1 K to ensure that the full range of the minimum temperature bandwidth of the infrared camera (ca. 5 K) is used

Prior to cleansing, the thermograph and the cameras are focussed at the location where the droplet will be created and the data acquisition system is initialized. The temperature bandwidth of the thermograph is chosen 5 K, so temperature differences of $5/256 \approx 0.02$ K can be distinguished. After cleansing, all the equipment is simultaneously activated and a droplet is positioned on the PMMA-plate. The droplet rests exactly on top of the Peltier element and has a diameter of 1.0 to 1.5 cm. The height is $\pm$ 3 mm as measured with a marking gauge. Calibration of distances on the thermovision system is done by measuring fixed, well-known lengths of parts of equipment that have a temperature different from their surroundings. In the temperature range considered ($15 - 40$°C), intensity values of the images correspond linearly to the temperature according to the specifications of the thermovision system.

6.4 Experiments and results

The repeatability of the experiments turned out to be poor. Sometimes motion did not occur in the droplet because of impurities which hamper interfacial motion as discussed in section 6.1. If the equipment was not cleansed properly, or the time passed between cleansing and experiment was too long, contamination of vital parts troubled the experiment. The following flow patterns have been observed in the experiments that did yield thermocapillary motion. During the first approximately 10 s the liquid is in motion due to injection of liquid in the droplet. When the accompanying interface oscillation, a kind of wobbling, subdues, tracer particles in the droplet are seen to be accelerated in the direction from the top to the bottom of the droplet. Roll-cells of various sizes are distinguished: smaller ones appear near the bottom of the droplet, larger ones appear when particles are transported from higher positions to the bottom. Similar patterns have been found by Zhang et al. [27] and Hoefsloot [11], see 6.1. Velocities of the order of $3 - 4$ mm/s are established at the interface near the foot of the droplet and of the order $1 - 1.5$ mm/s near the top. At the inside, the particles turn back to the core region of the droplet, with velocities of 0.5 mm/s maximum. These velocity magnitudes are based on estimates made by estimating the distances moved by particles in time. The error in this observation is typically of the order of 10%. After approximately 60 s, the particles in the droplet stop moving since the temperature gradient at the interface has disappeared. In Fig. 6.3 some characteristic particle paths are presented, as seen from above and from aside. Mainly larger roll-cell are drawn. The onset of some smaller roll-cells near the bottom can also be observed.

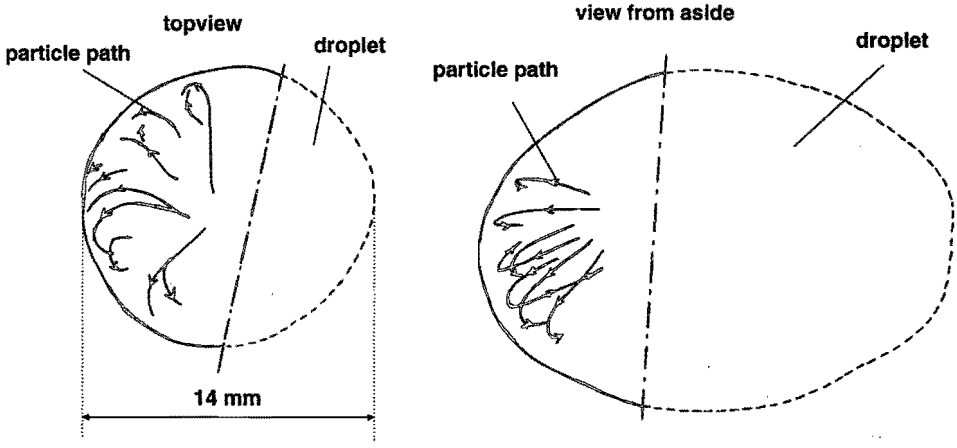

Figure 6.3: Tracer trajectories in half a droplet, topview (left, visualized vertically from above the droplet) and view from aside (right, visualized along a line at an angle of 43° with the horizontal).

Simultaneously with the velocity of the tracers, the evolution of the temperature at the interface of the droplet has been measured. In Fig. 6.4 a typical temperature history is shown.

The position of the droplet on the cooled plate is marked by the white circle. In the first plot ($t < 0$) of Fig. 6.4 the influence of the pipet in shaping the droplet is evident by the disturbed temperature profile. Let $t = 0$ s correspond to the moment the initial wobbling motion of the droplet has vanished. At subsequent times, $t > 0$, a temperature gradient exists at the interface, see Fig. 6.4. The mean

temperature of the droplet decreases in time due to the cooling by the Peltier element. As a result, the temperature gradient at the interface eventually disappears. In the next paragraph it will be shown that the interfacial motion and the occurrence of a temperature gradient coincide.

Fig. 6.5 shows the temperature differences over the droplet just after injection at $t = 5$ s and at $t = 67$ s as measured at various positions, indicated by their x- and y-coordinates. For the positions of the points of the grid over the droplet, see Fig. 6.4. It shows that the largest temperature difference is about 3.0 K, and that this is reached just after the injection. Nearly similar plots for the x- and y-direction are seen, proving that the droplet behaves nearly axisymmetrical, as is also shown by Fig. 6.4. The differences decrease in time, see Fig. 6.5, as was expected.

The evolution of the temperature gradient in time at five points is shown in Fig. 6.7. For the position of the points see Fig. 6.4. Two of these points lie just outside the droplet. It is clearly seen that the temperature becomes constant after $t = \pm 200$ s. The contour plots of Fig. 6.3 are drawn during the period that a temperature gradient at the interface exists. After this period, the thermocapillary convection stops, simultaneously with the disappearance of the temperature gradient along the interface.

From the profiles shown in Fig. 6.5 the surface tension gradient $\partial\sigma/\partial\theta$ can be derived from $\partial\sigma/\partial\theta = \partial\sigma/\partial T\ \partial T/\partial\theta$. The gradient for water/air, $\partial\sigma/\partial T = -0.148 \times 10^{-3}$ N/(mK), is obtained in a similar fashion as in chapter 4, using a surface tension meter, see appendix F, For values usually obtained, see [49], which come close to what we measured. $\partial T/\partial\theta$ is obtained from Fig. 6.5 and increases parabolically with increasing θ and reaches its maximum near the foot of the droplet. Therefore here the largest velocities are seen.

6.5 Conclusions

In this chapter thermocapillary convection in a water droplet without contamination has been investigated. In the experiments special consideration must be taken to cleanse the equipment. The temperature gradient along the droplet interface is measured and flow patterns in the droplet are visualized. The temperature gradient $\partial T/\partial\theta$ increases from top to foot; the velocity increases in this direction as it should. In time the temperature gradient vanishes since the induced flow homogenizes the temperature in the droplet. The flow pattern observed in the present experiments, small roll-cells near the foot and larger roll-cell elsewhere, are in good agreement with results found in the literature.

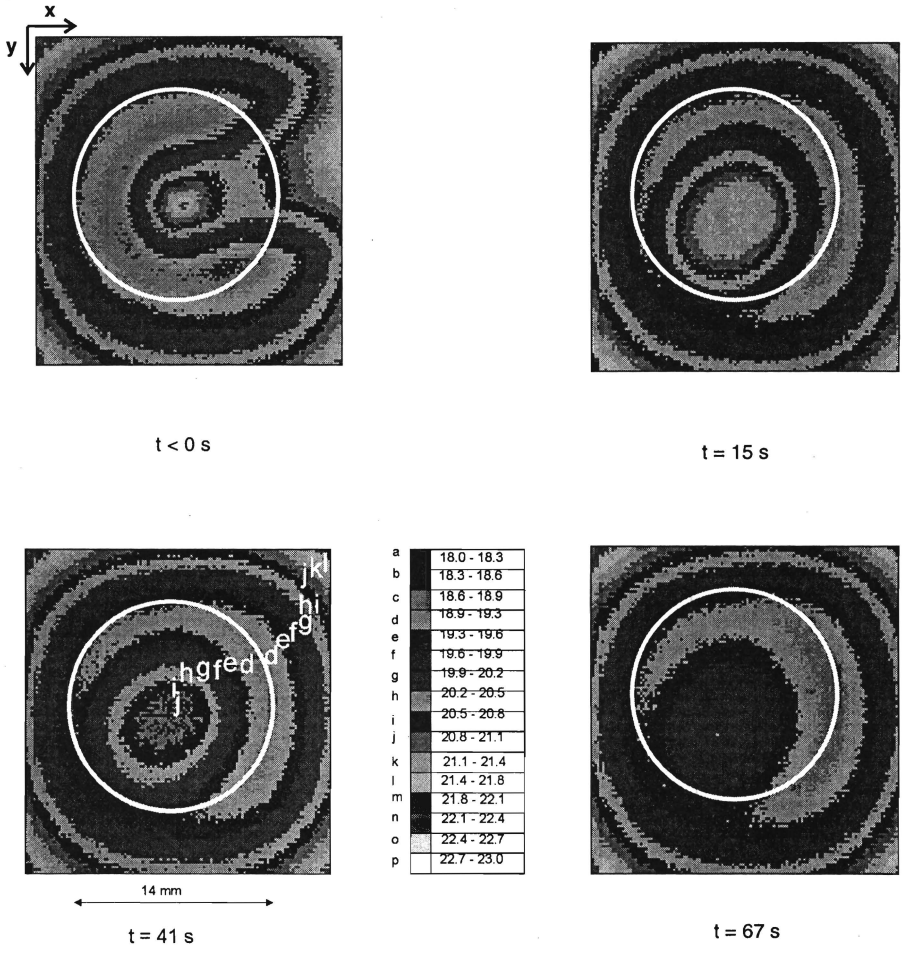

Figure 6.4: Typical time history of surface temperatures. Times 0, 15, 41 and 67 (left to right, top to bottom).

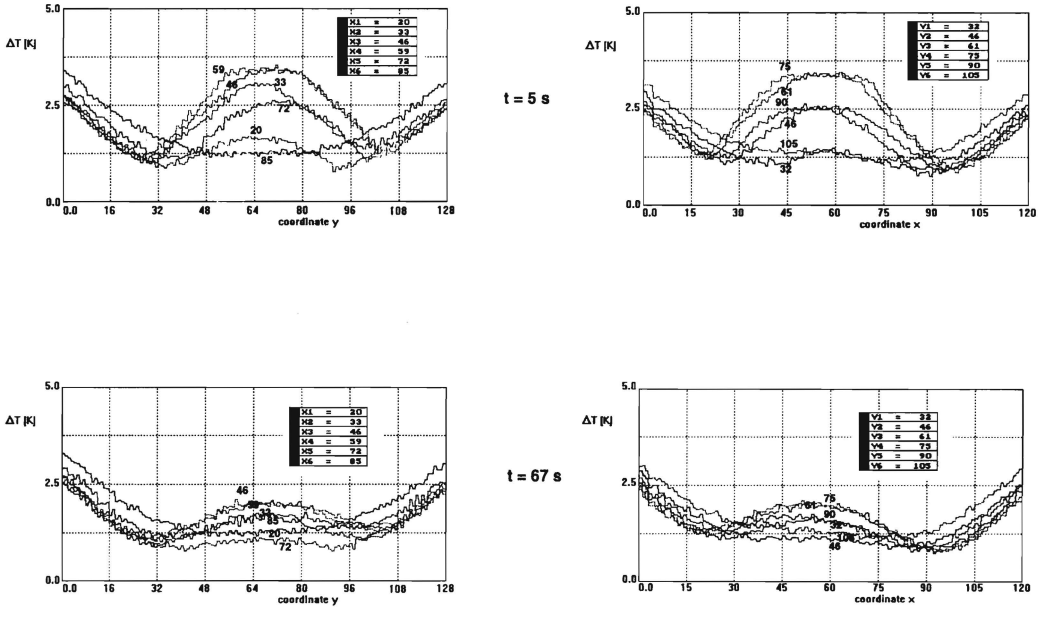

Figure 6.5: Plots of temperature distribution over droplet in x- and y-direction at $t = 5$ s and $t = 67$ s.

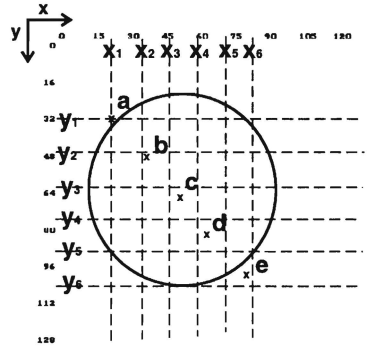

Figure 6.6: Position of lines and points on the droplet.

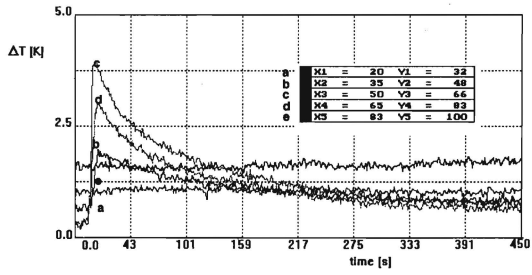

Figure 6.7: Temperature histories at five points near and at the droplet interface.

Chapter 7

Comparison of simulations with experiments

7.1 Introduction

In this chapter comparisons of numerical simulations with experiments are presented. From the interface temperature measurements, see chapter 4 and 6, the surface tension gradient is derived. This surface tension gradient distribution is prescribed in the method. The predicted flow patterns are compared with the ones observed during the experiments. Both the two-dimensional method of chapter 2 and the axisymmetrical droplet method of chapter 5 are employed. Some of the results of this chapter are not fully conclusive, since a number of parameters have not been varied over a wide range and since for some simulations the temperature field is required which would have to be obtained by solving of the energy equation simultaneously with the other equations.

7.2 Liquid layer heated from above

Numerical simulations are performed with the method described in chapter 2 to simulate the flow in the liquid layer heated from above as considered in the experiments described in chapter 4. Experiment 1, see appendix H is considered at $t^* = 65$ s since at that time a fully developed temperature gradient and flow pattern are established. The temperature gradient and surface tension gradient are stationary and constant over the entire cavity with values $\Delta T/\Delta x^* = 160$ K/m (see table H) and $\Delta\sigma/\Delta x^* = 0.016$ N/m^2, respectively. Typical values of the surface tension are 23.67×10^{-3} N/m at $x^* = 5$ mm and 24.16×10^{-3} N/m at $x^* = 37$ mm corresponding with temperatures at these positions of $T = 35$ and 30 °C, respectively. The length, L, is chosen 32 mm, the height, h_0^*, is chosen 8 mm since the experiment showed that velocities and velocity gradients such as $\partial u/\partial y$ near 8 mm of the interface are negligible small. Therefore, stresses at the bottom are minimal and are not taken into account. Thus $A = h_0^*/L = 1/4$. Furthermore, the resolution capacity of the grid is then utilized for the whole region of interest. The liquid (n-paraffin $C_{10} - C_{13}$) has $\rho = 752$ kg/m^3 and $\mu = 1.43 \times 10^{-3}$ Ns/m^2 which are assumed constant in the method.

With $\sigma = 24.16 \times 10^{-3}$ N/m and Eq. (2.8) the dimensionless quantities are easily calculated: $S_x = 1.04$ and $S_{gr} = \sigma/\Delta\sigma = 49.3$. These values are prescribed at the interface in the following way. The initial rise of S_x from zero at $t = 0$ to 1.04 at $t = 125\ \Delta t$ is accounted for by multiplying S_x with the smoothing function $F_1(t)$:

$$F_1(t) = \frac{1}{2}\left[\cos\left(\pi\left(1 + \frac{t}{125\ \Delta t}\right)\right) + 1\right] \quad \text{for } 0 \le t \le 125\ \Delta t \text{ and } F_1(t) = 1 \text{ at other times} \tag{7.1}$$

to ensure a gradually increase of S_x in time. The surface tension profile properly fulfils the symmetry condition, $S_x = 0$ at $x = 0$, by multiplying S_x with the correction factor $F_2(x)$:

$$F_2(x) = \frac{1}{2}\left[\cos\left(\pi\left(1 + 10\,x\right)\right) + 1\right] \quad \text{for } 0 \leq x \leq 0.1 \quad \text{and } F_2(x) = 1 \quad \text{elsewhere} \tag{7.2}$$

The no-slip condition, $S_x = 0$ at $x = 1$ is satisfied by multiplying S_x with $F_3(x)$:

$$F_3(x) = \frac{1}{2}\left[\cos\left(10\,\left(x - 0.8\right)\,\pi\right) + 1\right] \quad \text{for } 0.8 \leq x \leq 0.9 \quad \text{and } F_3(x) = 1 \quad \text{elsewhere} \tag{7.3}$$

The prescribed surface tension gradient, $S_{x,corr}(x,t)$, is given by: $S_{x,corr}(x,t) = 1.04\,F_1(t)\,F_2(x)\,F_3(x)$ and is shown in Fig. 7.1 with $F_1(t) = 1$.

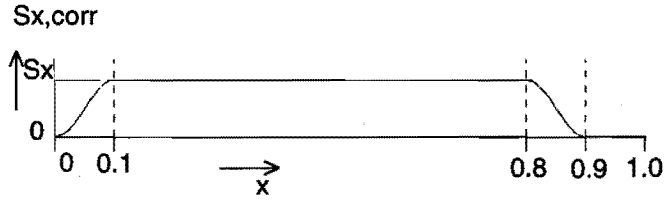

Figure 7.1: Corrected surface tension profile, $S_{x,corr}(x,t)$, with $F_1 = 1$.

The numerical parameters used are $n_k = 50$, $n_i = 50$, $n_{kc} = 15$, $n_{ic} = 7$ and $n_b = 12$. Runs are performed with gravity since the experiments have been carried out under 1-g conditions.

There are two time scales when gravity is involved, the one based on the tangential stress and the one based on the gravity force. The scaling of the velocity is based on the tangential stress, see Eq. (2.8), $u_t^* = h_0^*\,\Delta\sigma/\left(\mu\,L\right)$, with index t indicating that the velocity is related to the tangential stress. The velocity scale can also be based on the normal stress condition, Eq. (2.6), resulting in $u_g^* = \rho\,g^*\,L\,h_0^*/\mu$, with index g indicating that the velocity is related to the gravity force. $\Delta\sigma = 3.79$ is chosen so that the timescales, $t_t^* = u_t^*/L$ and $t_g^* = u_g^*/L$ are equal, to weight both the tangential stress and gravity force identical in the method.

Results are shown in Fig. 7.2 in dimensionless and dimensional coordinates and in the physical domain. Only the result at $t = 1.5$ is shown since the driving force is quasi-steady. A small roll-cell is distinguished near $x = 0$ similar to the one seen in the experiments. During the experiments, this roll-cell increased in size and extended over the entire length of the cavity. In the numerical simulation this is not the case, since numerical diffusion occurs. With numerical diffusion is meant that artificial terms, as the velocity v at the interface, increase in time. Therefore the interfacial deformation and the no-slip condition at $x = 1$ are not accounted for properly and the increase of the interfacial height near $x = 1$ is artificial. If the velocity v near the interface would not increase in time and the no-slip condition at $x = 1$ would have been exactly fulfilled at each time, the increase of the interfacial height near $x = 1$ would not occur. Because of this increase, the liquid is not forced back and the second roll-cell near $x = 1$ does not merge with the one originating near $x = 0$. Some adaptations are required in the method to ensure that this numerical diffusion is reduced. Such an adaptation could be that the velocity v at the interface is zero, so that hardly any interface deformation is established and that the roll-cells merge. Quantitative results of the dimensional velocities u^* and v^* at various x-positions over the height of the liquid are given in Fig. 7.3. The dimensional velocity in x-direction at the

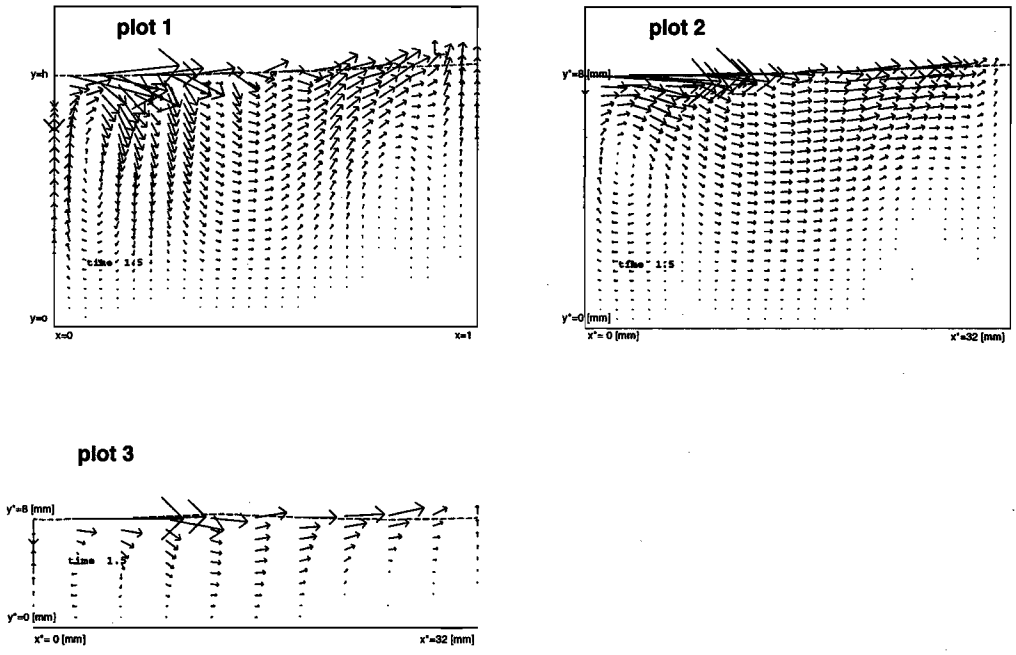

Figure 7.2: The velocity field in dimensionless (plot 1), dimensional (plot 2) and in the physical domain (plot 3) of simulation of layer experiment. Reference arrow of the velocity component in x-direction corresponds to 0.14 mm/s. Reference arrow of the velocity component in y-direction corresponds to 0.046 mm/s.

interface is of the order 2.5 mm/s for $0.3 < x < 0.7$, which compares quite well with the measured velocity of experiment 1 of 1.76 mm/s, see table 4.2.

7.3 Liquid droplet on a plate cooled from below

In this section, results of numerical simulations with the method of chapter 5 are compared with results of the experiments of a droplet on a cold plate, see chapter 6. In the method, an axisymmetrical water droplet, see Fig. 5.1, has been considered with an initial radius of $R = 1.0$ cm and $\rho = 998$ kg/m^3, $\mu = 1.002 \times 10^{-3}$ Pa s and $\sigma = 72.3 \times 10^{-3}$ N/m. The surface tension gradient is derived from the temperature profile as measured with the thermograph, see Fig. 6.5 at $t = 5$ s, with a temperature drop of 2.1°C along the droplet interface from the top to the foot. The largest gradient occurs near the foot of the droplet. A temperature of 0.7°C is assumed in the method at angles between $\pi/3$ and $\pi/2$. For $0 \leq \theta \leq \pi/3$, $d\sigma/d\theta = 0$. The measured surface tension gradient can be approximated by:

$$\frac{\partial \sigma}{\partial \theta} = 0.95 \times 10^{-4} \left[\sin\left(6 \left(\theta - \frac{\pi}{12}\right)\right) + 1 \right] \tag{7.4}$$

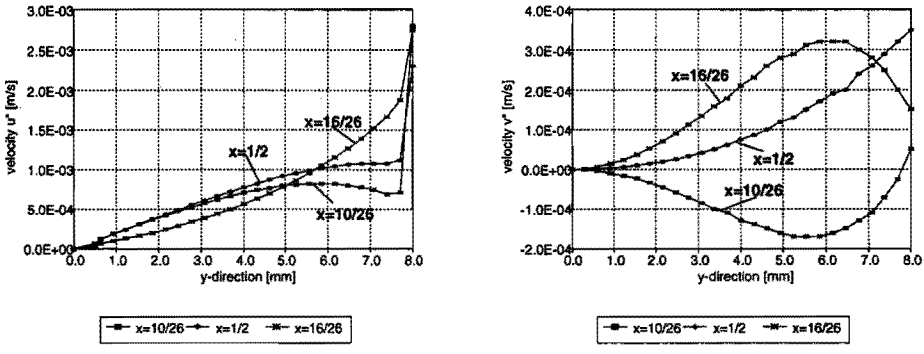

Figure 7.3: The dimensional velocities u^* and v^* over the height of the liquid at various positions x.

In Fig. 7.4 a plot is shown of the numerically prescribed gradient $\partial\sigma/\partial\theta$. Note that $\partial\sigma/\partial\theta$ is positive

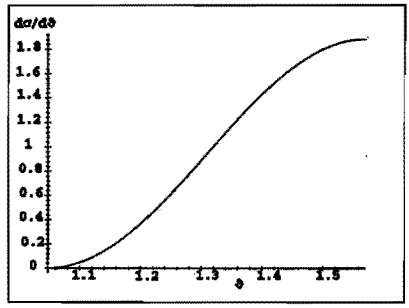

Figure 7.4: Surface tension gradient $d\sigma/d\theta$ versus θ (in radians).

for $\pi/3 \leq \theta \leq \pi/2$. At $\pi/3$, $\partial\sigma/\partial\theta = 0$ and at $\pi/2$, $\partial\sigma/\partial\theta$ reaches its maximum. Below the corrected surface tension gradient, $(\partial\sigma/\partial\theta)_{corr}$, is derived.

Numerically $\partial\sigma/\partial\theta$ is multiplied with a normal distribution $G_1(t)$ in time:

$$G_1(t) = (t\,(t-\beta))^2 \tag{7.5}$$

which guarantees that the driving force increases in first instance and decays later.

$\partial\sigma/\partial\theta$ is multiplied with a correction term $G_2 = 64$ to make sure that at $t = \beta/2$ the maximum amplitude of $\partial\sigma/\partial\theta$ (0.95×10^{-4}) is reached. The corrected surface tension profile is $(\partial\sigma/\partial\theta)_{corr}$:

$$\left(\frac{\partial\sigma}{\partial\theta}\right)_{corr} = 0.95 \times 10^{-4} \left[\sin\left(6\,\left(\theta - \frac{\pi}{12}\right)\right) + 1\right]\, G_1(t)\, G_2 \tag{7.6}$$

The distribution, Eq. 7.6, is used in the method of chapter 5. At $\theta = \pi/2$, the dynamic contact angle ϕ_d of the droplet on the plate is $\pi/2$ during the simulation. The interface is immobile in the simulation. Parameters used are $n_k = 50$, $n_i = 50$, $n_{kc} = 10$, $n_{ic} = 5$, $\epsilon = 1$ and $\Delta t = 0.006$ s. Note that $d\sigma/d\varphi = d\sigma/dr = 0$ during the simulations.

Fig. 7.5 shows the velocity profiles at times $t = 0.006$, 0.3, 0.6 and 0.9 s. The liquid flows from

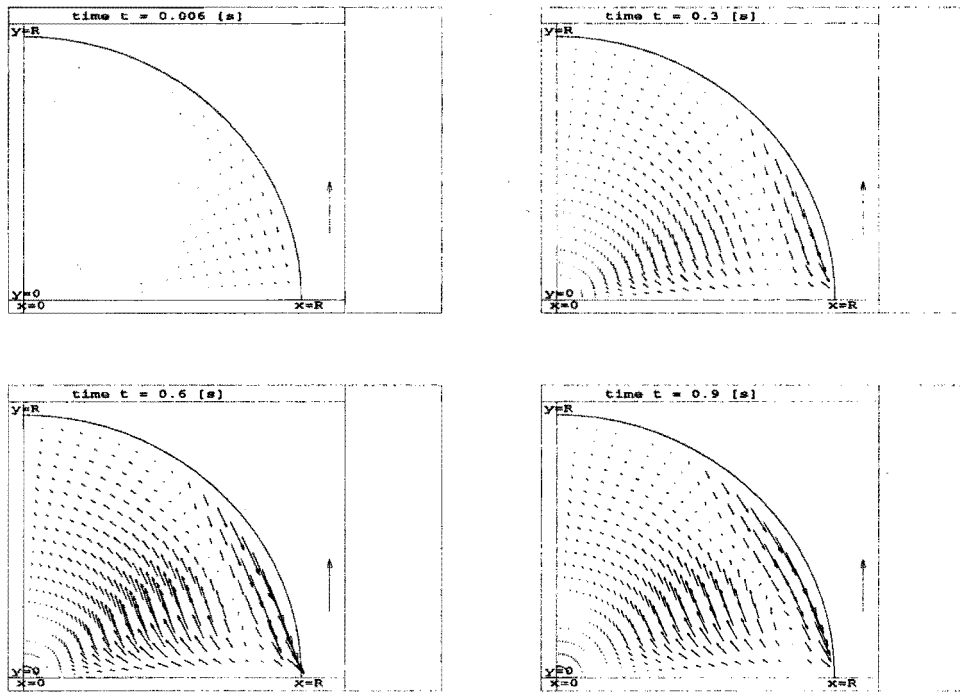

Figure 7.5: The simulated velocity profiles at times $t = 0.006$ (velocity multiplied by $1000\times$), 0.3, 0.6 and 0.9 s. The reference arrow of the velocity has a value of 0.1 mm/s.

$\theta = \pi/3$ to $\theta = \pi/2$ and roll-cells (vortices) below the interface form, that are qualitatively the same as those observed during the experiments, see Fig. 6.3. Velocities of ca. 0.1 mm/s are established at the interface at $t = 0.6$ s. Initially the velocity increases since the driving force increases. After some time the driving force decreases so the velocity decreases slightly, as seen from comparison of the plots at times $t = 0.6$ s and $t = 0.9$ s. Fig. 7.6 shows the velocity at $\theta = \pi/8$, $\pi/4$ and $3\,\pi/8$, to show better how the velocity varies with the radial distances.

7.4 Conclusions

Comparison of numerical simulations with results of experiments show that the present computational results correspond satisfactorily to the experimental results.

From the simulation of the flow in the liquid layer it is concluded that the predicted velocity is in quantitative agreement with the measured velocity although the predicted flow pattern is not fully established. The predicted flow pattern in the droplet corresponds well to the flow pattern seen in the experiments. The following adaptations of the numerical method are proposed in order to improve the correlation of numerical simulations and experiments:

- Adding of the energy equation to the system of partial differential equations to be solved. The

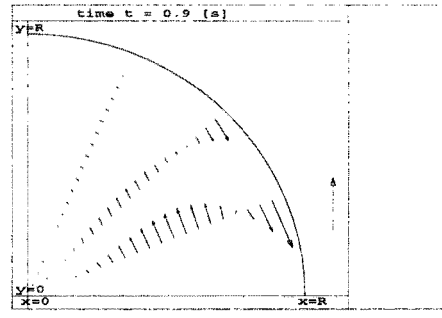

Figure 7.6: The velocity at time $t = 0.9$ s for $\theta = \pi/8$, $\pi/4$ and $3\ \pi/8$. The reference arrow has a value of 0.1 mm/s.

temperature distribution in the liquid is then taken into account too.

- Ensuring that numerical diffusion subdues, so that hardly any interface deformation can establish and the roll-cells merge.

Chapter 8

Conclusions and recommendations

Various aspects of Marangoni convection have been studied in this thesis. In section 8.1 the main conclusions are summarized. Some suggestions for future research are given in section 8.2.

8.1 Conclusions

8.1.1 Numerical simulations

An algorithm is presented to predict the time evolution of the velocity field and the interfacial motion due to the Marangoni effect. The accuracy of the numerical predictions depends on the choice of the basic expansion functions. One application is the simulation of the motion in a thin layer of liquid in a cavity, another that of axisymmetrical flow in an axisymmetric droplet on a plate.

The main characteristics of the algorithm are:

- It is related to the spectral collocation technique. The grid of collocation points is self-adapting to the motion of the liquid/air interface and not fixed or rigid because of the application of the Singular Value Decomposition (SVD) technique, see below.
- The tangential stress boundary condition at the free interface is simultaneously solved with the so-called contour integrals, that are derived from the Navier-Stokes equations and the normal stress condition.
- An adapted SVD-treatment is employed which automatically weights the importance of the contour integrals and the tangential stress condition.
- The kinematic boundary condition couples the evolution of the velocity field to the motion of the interface.
- Iterations are not employed.
- In both applications the solution is based on truncated expansions, so the accuracy of the solution is directly controlled through the number of terms in the expansions.

Applications for which the two-dimensional flow method can be used are:

- The drying of hydrophillic surfaces
- Thin layers of paint, coatings or glues
- Welding

- Metallurgical applications
- Growth of crystals

Thermocapillary flow in droplets, for example as exists in the droplets occurring in condensation on plastic heat exchangers, can be simulated with the axisymmetrical flow method.

Liquid layer

The approach is found to precisely reproduce an analytical solution for a heated thin liquid layer with steady motion. The velocity expansion converges rapidly and the tangential stress condition at the interface is satisfied within adequate order of magnitude. Parameter variation such as varying the number of collocation points and the number of expansion coefficients is performed leading to the choice of a suitable set of numerical parameters.

It is concluded that liquids with larger viscosity are more difficult to set into motion than those with smaller viscosity. Test cases with different viscosities show that when the driving force decreases or is not present, the velocity in the liquid decreases. These results are similar to that of investigations from the literature.

The solution algorithm has been tested with alternative expansions for the velocity and interface position. Each of these alternative expansions accommodates a specific set of boundary conditions best. For comparable test cases the results turn out to be similar, therefore the solution algorithm is found to be robust with respect to the choice of the expansion functions.

From the test cases it is concluded that the method presented can accurately predict thermocapillary two-dimensional convection in cavities.

Droplet

The axisymmetrical flow method is successfully applied to an axisymmetric droplet on a plate.

8.1.2 Experiments

In two test configurations the temperature gradient has been measured along the interface and the established flow is visualized. One experimental set-up consists of a layer of n-paraffin $C_{10} - C_{13}$ in a cavity heated from above by a wire, the other of a water droplet on a plate cooled from below by a Peltier element.

Liquid layer

In the liquid layer experiments, buoyancy effects are negligible and the thermocapillary effect dominates the flow during the first 90 s. Nearly steady flow is then established with an almost constant surface tension gradient. The influence of the side-walls is negligible and the same flow is established in each cross-section, i.e. in a plane normal to the straight heating wire, rendering the flow two-dimensional. After being accelerated away from the heating wire particles assume constant velocity at the interface and return along deeper layers of the cavity. A characteristic constant driving force of $\partial\sigma/\partial x = 0.018 \pm 0.001$ N/m^2 at the interface results in an averaged surface velocity of 1.43 ± 0.18 mm/s.

Droplet

The temperature gradient increases from the top to the foot of the droplet; the velocity also increases in this direction. In time the temperature gradient vanishes since the flow homogenizes the temperature

in the droplet. The flow pattern, small roll-cells near the foot and larger roll-cells elsewhere, is in good agreement with results from experiments reported in the literature.

8.1.3 Comparison of numerical simulations with experiments

Comparison of results of the simulations with those of experiments show that, in first approximation, computational results correlate satisfactorily.

From the simulation of the flow in the liquid layer it is concluded that the predicted velocity field is in quantitative agreement with the measured velocity field although the predicted flow pattern is not fully established.

The predicted flow pattern in the droplet corresponds well to the flow pattern observed in the experiments.

8.2 Recommendations

8.2.1 Numerical simulations

The two-dimensional flow method can be extended such that it can handle a segmented computational domain with for each segment a suitable expansion, resulting in a multi-domain method. More complicated geometries can then be treated. At domain boundaries the coupling of the solution in the neighbouring domain must be taken care of.

8.2.2 Experiments

For the measurements in the layer more accurate velocity measurements can be performed using for example Laser Doppler Anemometry. The proper choice of suitable tracers is then relevant.

For the measurements in the droplet more quantitative results can be found by improving the visualization technique. The repeatability of the experiments can be improved by performing the experiments under better controlled conditions.

8.2.3 Comparison of numerical simulations with experiments

Adaptations are required in the two-dimensional flow method to ensure that numerical diffusion leading to an artificial velocity normal to the interface is minimized. Parameters might be varied over a wider range and solving of the energy equation might be required.

Appendix A

Existing numerical techniques

In this appendix the main existing numerical methods for solving the Navier-Stokes equations are shortly described [19][20][21]. These methods are surveyed in section 1.3 for reasons given there. This appendix may help to refresh the memory of the reader who does not deal with numerical algorithms every day.

A.1 Finite Difference Method (FDM)

FDM is based on the properties of Taylor series expansions around the values at grid points and on discretizing the derivatives of the differential equations. The grid points are located at the intersections of a family of rectilinear or curved contours.

The derivative u_x of a function u at point x is defined by:

$$u_x = \frac{\partial u}{\partial x} = \lim_{\Delta x \to 0} \frac{u(x+\Delta x) - u(x)}{\Delta x} \tag{A.1}$$

A Taylor-series is developed of $u(x+\Delta x)$ to determine the order of accuracy of the scheme:

$$u(x+\Delta x) = u(x) + \Delta x\ u_x(x) + \frac{\Delta x^2}{2}\ u_{xx}(x) + \ldots \tag{A.2}$$

with: $u_{xx}(x) = \partial^2 u(x)/\partial x^2$.
Rewriting Eq. (A.2) yields:

$$\frac{u(x+\Delta x) - u(x)}{\Delta x} = u_x(x) + \mathcal{O}(\Delta x) \tag{A.3}$$

which means that the approximation is improved by reducing Δx, but for any finite value of Δx an truncation error $\mathcal{O}(\Delta x)$ must be accepted.

With the aid of FDM the PDEs are reduced to a system of algebraic equations in matrix-form that can be solved efficiently numerically. For example:

$$\frac{\partial u}{\partial x} = f \tag{A.4}$$

can be rewritten as:

$$A\ u = f \tag{A.5}$$

with A a positive definite matrix, which means:

- A is symmetric, so $A^T = A$

- Each $x \neq 0$ yields $x^T\ A\ x \geq 0$

The system of equations Eq. (A.5) can easily be solved with, for instance, a LU-decomposition.

The used differential-schemes for first-order derivatives can be chosen as a forward difference, see Eq. (A.1) or Eq. (A.6), or as a backward scheme, see Eq. (A.6), (both first-order approximations) or as a central scheme, see Eq. (A.6) (second-order approximation):

$$\begin{aligned}(u_x)_i &= (\frac{\partial u}{\partial x})_{x=x_i} = \frac{u_{i+1}-u_i}{\Delta x} + \mathcal{O}(\Delta x) \\ (u_x)_i &= (\frac{\partial u}{\partial x})_{x=x_i} = \frac{u_i-u_{i-1}}{\Delta x} + \mathcal{O}(\Delta x) \\ (u_x)_i &= (\frac{\partial u}{\partial x})_{x=x_i} = \frac{u_{i+1}-u_{i-1}}{2\ \Delta x} + \mathcal{O}(\Delta x^2)\end{aligned} \tag{A.6}$$

with $x_i = i\ \Delta x, i = 1, .., N$ and N discrete mesh points with equal spacing of Δx and u_i the value of function $u(x)$ at the point x_i. For second-order derivatives schemes derived from the first-order ones are easily obtained, for example:

$$\frac{\partial^2 u}{\partial x^2} = \frac{u(x+\Delta x) - 2\ u(x) + u(x-\Delta x)}{(\Delta x)^2} + \mathcal{O}(\Delta x^2) \tag{A.7}$$

with a truncation error of $\mathcal{O}(\Delta x^2)$. Ryazantsev et al. [50] used an implicit difference scheme on a non-uniform grid in a stream function-vorticity formulation to calculate the nonsteady distribution of velocity and temperature in a liquid layer of a plane cylindrical cuvette. They found a change in the direction of the thermocapillary forces/flows due to increasing and decreasing temperature gradients.

FDM was successfully applied for both 1D and 2D situations. Bestehorn et al. [51] used FDM to predict the transition from one roll cell to hexagon roll cells formation in different geometries. The transition occurred when additional thermocapillary convection was introduced by heating up the surface.

FDM can have some disadvantages. More complicated governing equations require much more calculation time. Another disadvantage is that when the boundaries are curved the formulation of FDM gets more difficult. A solution is found by using interpolation, but this makes the problem more complex, especially if complicated boundary conditions have to be imposed. Local grid refining near the boundaries is difficult to apply, which makes FDM less flexible than other methods, such as FEM. A third option to solve problems with a curved boundary is a transformation from the physical space to a computational space, but this is usually hard to do. Furthermore, oscillations can occur when due to the boundary condition the solution near the boundary fluctuates strongly. The reason for these oscillations is found in the matrix A of Eq. (A.5), that loses its diagonal dominance, which means that the matrix is close to being singular.

A.2 Boundary Element Method (BEM)

BEM is an useful tool for solving linear homogeneous differential equations. In situations in which the governing equations have solutions in terms of Green's functions, such as the Laplace equation $\nabla^2 u = 0$ with u an arbitrary scalar function, BEM has been applied successfully. The imposed boundary conditions are satisfied by a proper distribution of elementary solutions on boundaries of the flow domain.

The advantage of BEM is that only the boundary has to be discretized, not the entire flow field, which reduces the problem enormously. 3D-problems are in this way solved by distributions on surfaces, so instead of calculating with $\mathcal{O}(N^3)$ elements now $\mathcal{O}(N^2)$ elements are employed. A disadvantage is that for the solution of inhomogeneous equations, for example the Poisson-equation $\nabla^2 u = q$

with q an arbitrary scalar function, employing BEM is more troublesome. Extra terms for the discretization of the bulk of the liquid, i.e. spatial source terms, must then be introduced, which renders the problem much more complicated and the quasi two-dimensionality is lost. More details about BEM can be found in [19].

A.3 Finite Element Method (FEM)

FEM is based on the construction of an approximate solution of PDEs using basic functions. It is known [2] that the approximation of the PDEs converges to the true solution if an increasing number of basic functions is used. An approximation of the solution is found if only a finite number (N) of basic functions is used. In FEM the flow domain is divided into elements. In 1D these are intervals, in 2D triangles or rectangles. There is a finite number of them over the whole area and they are patched to each other without overlap. Consider some points on each element, the so-called basic points. Choose the basic functions in such a way that in one basic point its value is 1 and in the other(s) 0, that the desired order and type of interpolation polynomials are prescribed per element and such that each basic function is continuous in the whole domain. In this way an interpolation polynomial for the approximation is constructed for each element:

$$u(x,y) = \sum_{i=1}^{N} u_i \phi_i(x,y) \tag{A.8}$$

The coefficients of this polynomial are the unknown function values u_i in the basic points.

In FEM two methods can be used:

- **Ritz-method.**
  An approximate solution is constructed of an minimization problem which is equivalent to the PDEs. This minimization problem can be reduced to a solvable matrix equation under the condition that the solution $u(x,y)$ can be written as a linear combination of basic functions $\phi_i(x,y)$ with coefficients u_i as Eq. (A.8).

  The generated matrix is in general dense. Its condition is bad and when many basic functions are used, round-off errors will dominate the approximation. These round-off errors can be minimized when the form of the solution is known, since the selection of the basic functions then can conveniently be based on this solution. Remark that none of the basic functions has to fulfil the boundary conditions on its own, since in the limit of $N \to \infty$ the approximation fulfils these conditions.

- **Galerkin-method.**
  This method is called the method of weighted residuals and can be used when an equivalent minimization problem does not exist, as is the case for the convection-diffusion equation and the Navier-Stokes equations. Consider a PDE of the form with matrix L:

  $$L\,u(x,y) \;=\; f(x,y) \tag{A.9}$$

  on domain ω with $u(x,y) = 0$ on the boundary γ of the considered domain. The exact solution u of this differential equation satisfies:

  $$\int_\omega w\;(L\,u - f)\,dxdy \;=\; 0 \tag{A.10}$$

  for arbitrary function $w(x,y)$. An approximate solution is constructed if N independent functions $w_j(x,y)$ are selected, satisfying:

  $$\int_\omega w_j\;(L\,u - f)\,dxdy \;=\; 0 \quad j = 1,\ldots,N \tag{A.11}$$

When the approximate solution of Eq. (A.8) is substituted for u in Eq. (A.11), then the original PDE is written as a system of N equations with N unknowns. The best choice for the basic functions is according to Galerkin:

$$w_j(x,y) \;=\; \phi_j(x,y) \tag{A.12}$$

The Galerkin method has a lot in common with the Ritz-method. The matrix equation and the treatment of the boundary conditions are the same, so the result of the approximation is also equal. The Galerkin method is more general to use and is more direct, since the functional for the equivalent minimization problem does not need to be known.

Advantages of FEM are that no equidistant mesh is necessary, that difficult geometries are no problem and that it is easy to automate the computation of the same integral that has to be evaluated per element for all times. A disadvantage of FEM, in the velocity-pressure formulation, is that numerical problems occur for the pressure p, since the continuity equation does not contain the pressure. Several techniques are nowadays known to solve the Navier-Stokes equations and the continuity equation more accurately. These tools can be divided into two main groups:

- **Direct methods.**
  The Navier-Stokes equation and the continuity equation are reduced to a system of linear equations via the Galerkin method, for more details, see [20]. An advantage is that the velocity components u and v and pressure p are calculated without numerical differentiation, so they tend to be more accurate. A disadvantage is that the system of equations becomes very large requiring a lot of calculation time. Furthermore, zeros appear in the main diagonal of the matrix, so partial pivoting is required to get accurate result. Partial pivoting increases the calculation time even more. It is therefore concluded that this method is direct and clear but is hardly ever used because of the enormous calculation time.

- **Indirect methods.**
  There are two indirect manners:

  - **Penalty-function method.**
    The principle of the penalty-function method is the substitution of the continuity equation by a relation between the velocity vector u and pressure p of the form:

    $$\frac{p}{\tau} + \nabla \cdot u \;=\; 0 \tag{A.13}$$

    with τ a penalty-function parameter. The advantage of this technique is that the velocity- and pressure determination are decoupled. This leads to a smaller system of equations with less unknowns. First an approximate solution is constructed of the matrix equation after which the pressure is calculated from Eq. (A.13). Partial pivoting is not necessary which saves calculation time and memory. This method is also very useful in 3D situations. The parameter τ must be chosen well, for otherwise accuracy problems may occur since the resulting matrix may become singular.

  - **Methods with use of divergence-free elements.**
    The basic functions ϕ for the velocity approximation are chosen to fulfil the integral expression for the continuity equation:

    $$\int_e \nabla\phi \, dxdy \;=\; 0 \tag{A.14}$$

    with e an arbitrarily chosen element. By the proper choice of the used elements, the pressure terms are eliminated from the Navier-Stokes equations. Now the pressure and velocity are separated and the continuity equation is satisfied per element making the numerical

solution routine more efficient. The pressure is calculated after that the velocity has been determined. The matrix equation has a simple structure and calculation time and used memory is therefore strongly reduced. A disadvantage is that this method is only useful for 2D situations and axisymmetrical problems due to the use of the stream function, see for more details [20]. Another disadvantage is that boundary conditions have to be transformed before they can be used to fit in the used method. The solution has to be transformed as well in order to be interpreted. Especially the boundary conditions for the stream function may cause problems upon transforming.

Appendix B

Adapted Singular Value Decomposition

Consider the matrix equation of the contour integrals, Eq. (2.36), but then written as follows: $\underline{\underline{A}}\, d = \underline{q}$. Then $\underline{\underline{A}}^T\, \underline{\underline{A}}\, d = \underline{\underline{A}}^T\, \underline{q}$ [1]. More details about this appendix are described in [33].

The objective of this section is to obtain the total least-squares solution of this system. To that end the vector d is extended by an extra element, the scalar -1. Then the following block matrix equation is formed

$$\left(\underline{\underline{A}}\ \underline{q}\right) \begin{pmatrix} d \\ -1 \end{pmatrix} = 0 \tag{B.1}$$

I.e. $\underline{\underline{\tilde{A}}}\, \tilde{d} = 0$ with $\underline{\underline{\tilde{A}}} = \left(\underline{\underline{A}}\ \underline{q}\right)$ and $\tilde{d} = \begin{pmatrix} d \\ -1 \end{pmatrix}$

$\underline{\underline{\tilde{A}}}^T\, \underline{\underline{\tilde{A}}}$ is a positive symmetric matrix and its eigenvalues are real, non-negative and there exists an orthonormal basis of eigenvectors.

So, when $\underline{x}$ is an eigenvector of $\underline{\underline{\tilde{A}}}^T\, \underline{\underline{\tilde{A}}}$ with norm 1 and with positive eigenvalue λ^2, then

$$\underline{\underline{\tilde{A}}}^T\, \underline{\underline{\tilde{A}}}\, \underline{x} = \lambda^2\, \underline{x}$$

Define $\underline{y} = \frac{\underline{\underline{\tilde{A}}}\, \underline{x}}{\lambda}$, then

$$\lambda^2\, \underline{x} = \underline{\underline{\tilde{A}}}^T\, \underline{\underline{\tilde{A}}}\, \underline{x} = \lambda\, \underline{\underline{\tilde{A}}}^T\, \underline{y}$$

and

$$\underline{\underline{\tilde{A}}}\, \underline{\underline{\tilde{A}}}^T\, \underline{y} = \lambda\, \underline{\underline{\tilde{A}}}\, \underline{x} = \lambda^2\, \underline{y}$$

So, $\underline{y}$ is an eigenvector of matrix $\underline{\underline{\tilde{A}}}\, \underline{\underline{\tilde{A}}}^T$. Since $\underline{y} = \lambda^{-1} \underline{\underline{\tilde{A}}}\, \underline{x}$, $\underline{y}^T = \lambda^{-1} \underline{x}^T\, \underline{\underline{\tilde{A}}}^T$ and $\lambda^2\, \underline{y}^T\, \underline{y} = \underline{x}^T\, \underline{\underline{\tilde{A}}}^T\, \underline{\underline{\tilde{A}}}\, \underline{x} = \lambda^2\, \underline{x}^T\, \underline{x} = \lambda^2$ since $\underline{x}$ has norm 1. Hence $\underline{y}^T\, \underline{y} = 1$, so $\underline{y}$ has norm 1.

Define $n = n_{kc} \times n_{ic}$ being the number of unknown $d_{i,k}$-coefficients. Order eigenvectors $\underline{x}_1, \underline{x}_2, \cdots, \underline{x}_n$ and $\underline{y}_1, \underline{y}_2, \cdots, \underline{y}_n$ such that $\lambda_1 \geq \lambda_2 \geq \cdots \geq \lambda_n$. $\underline{\underline{\tilde{A}}} = \lambda_1\, \underline{y}_1\, \underline{x}_1{}^T + \cdots + \lambda_n\, \underline{y}_n\, \underline{x}_n{}^T$ which can be verified by multiplying both sides with the elements of the basis, i.e. the individual eigenvectors $\underline{x}_1, \underline{x}_2, \cdots, \underline{x}_n$.

The matrix $\underline{\underline{A'}}$ of rank j for which the Frobenius norm of $\underline{\underline{\tilde{A}}} - \underline{\underline{A'}}$ is minimal is given by:

$$\underline{\underline{A'}} = \lambda_1\, \underline{y}_1\, \underline{x}_1{}^T + \lambda_2\, \underline{y}_2\, \underline{x}_2{}^T + \cdots + \lambda_j\, \underline{y}_j\, \underline{x}_j{}^T \tag{B.2}$$

[1] The $d_{i,k}$-coefficients are the elements of a $(n_{kc} \times n_{ic})$-matrix with columns $d_{i,0}, d_{i,1}, \ldots, d_{i,n_{kc}-1}$. Vector d is defined as $d = (d_{i,0}{}^T, d_{i,1}{}^T, \ldots, d_{i,n_{kc}-1}{}^T)^T$.

which is a well-known property of the singular values λ_j. The choice for j, the number of significant singular values, and the purpose of this choice is discussed in section 2.3.4. To obtain a solution of $\underline{\underline{A'}}\,\underline{d} = 0$, see Eq. (B.2), the matrix $\underline{\underline{A'}}$ is written as a block matrix $\underline{\underline{A'}} = (\underline{\underline{A^*}}\ \underline{q^*})$, where $\underline{q^*}$ is a vector of length $n_i \times n_k$, corresponding to the number of contour integrals. For $1 \leq i \leq j$ let the eigenvectors $\underline{x_i}$ be: $\underline{x_i} = \begin{pmatrix} \underline{x_i^*} \\ \underline{s_i} \end{pmatrix}$, with $\underline{s_i}$ the last element of vector $\underline{x_i}$, see section 2.3.4. The equation $\underline{\underline{A'}}\,\underline{d} = 0$ yields:

$$\left(\underline{\underline{A^*}}\ \underline{q^*}\right) \begin{pmatrix} d \\ -1 \end{pmatrix} = 0 \quad \text{or} \quad \underline{\underline{A^*}}\,\underline{d} = \underline{q^*} \tag{B.3}$$

Eq. (B.2) yields:

$$\underline{\underline{A^*}}\,\underline{d} = \left(\lambda_1\,\underline{y}_1\,(\underline{x}_1^*)^T + \cdots + \lambda_j\,\underline{y}_j\,(\underline{x}_j^*)^T\right)\,\underline{d} \tag{B.4}$$

and

$$\underline{q^*} = \lambda_1\,\underline{y_1}\,\underline{s_1} + \cdots + \lambda_j\,\underline{y_j}\,\underline{s_j} \tag{B.5}$$

Because of $\underline{\underline{A^*}}\underline{d} = \underline{q^*}$ and $\lambda\underline{y} = \underline{\underline{\tilde{A}}}\,\underline{x}$ this yields:

$$\left(\underline{\underline{\tilde{A}}}\,\underline{x_1}(\underline{x^*})^T + \cdots + \underline{\underline{\tilde{A}}}\underline{x_j}(\underline{x^*})^T\right)\,\underline{d} = \underline{s_1}\,\underline{\underline{\tilde{A}}}\,\underline{x_1} + \cdots + \underline{s_j}\,\underline{\underline{\tilde{A}}}\,\underline{x_j} \tag{B.6}$$

$$\underline{\underline{A^*}}\underline{d} = \underline{q^*} \tag{B.7}$$

so:

$$\underline{\underline{A^{*T}}}\,\underline{\underline{A^*}}\underline{d} = \underline{\underline{A^{*T}}}\,\underline{q^*} \tag{B.8}$$

Substitution for $\underline{\underline{A^*}}$ and $\underline{q^*}$ shows:

$$\begin{aligned}\left(\underline{x_1}^*\,\underline{x_1}^T\,\underline{\underline{\tilde{A}}}^T + \cdots + \underline{x_j}^*\,\underline{x_j}^T\,\underline{\underline{\tilde{A}}}^T\right)\,\left(\underline{\underline{\tilde{A}}}\,\underline{x_1}\,(\underline{x_1}^*)^T + \cdots + \underline{\underline{\tilde{A}}}\,\underline{x_j}\,(\underline{x_j}^*)^T\right)\,\underline{d} \\ = \left(\underline{x_1}^*\,\underline{x_1}^T\,\underline{\underline{\tilde{A}}}^T + \cdots + \underline{x_j}^*\,\underline{x_j}^T\,\underline{\underline{\tilde{A}}}^T\right)\,(\underline{s_1}\,\underline{\underline{\tilde{A}}}\,\underline{x_1} + \cdots + \underline{s_j}\,\underline{\underline{\tilde{A}}}\,\underline{x_j})\end{aligned} \tag{B.9}$$

Note that $\underline{\underline{\tilde{A}}}^T\,\underline{\underline{\tilde{A}}}\,\underline{x} = \lambda^2\,\underline{x}$. Therefore:

$$\begin{aligned}\left(\underline{x_1}^*\,\underline{x_1}^T + \cdots \underline{x_j}^*\,\underline{x_j}^T\right)\,\left(\lambda_1^2\,\underline{x_1}\,(\underline{x_1}^*)^T + \cdots + \lambda_j^2\,\underline{x_j}\,(\underline{x_j}^*)^T\right)\,\underline{d} \\ = \left(\underline{x_1}^*\,\underline{x_1}^T + \cdots \underline{x_j}^*\,\underline{x_j}^T\right)\,(\underline{s_1}\,\lambda_1^2\,\underline{x_1} + \cdots + \underline{s_j}\,\lambda_j^2\,\underline{x_j})\end{aligned} \tag{B.10}$$

The eigenvectors $\underline{x}_1, \cdots, \underline{x}_j$ form an orthonormal set, hence:

$$\left(\lambda_1^2\,\underline{x_1}^*\,(\underline{x_1}^*)^T + \cdots + \lambda_j^2\,\underline{x_j}^*\,(\underline{x_j}^*)^T\right)\,\underline{d} = \underline{s_1}\,\lambda_1^2\,\underline{x_1}^* + \cdots + \underline{s_j}\,\lambda_r^2\,\underline{x_j}^* \tag{B.11}$$

This is the total least-squares solution of the contour integrals. In section 2.3.4 these equations are combined with the matrix equation obtained from the tangential stress condition, Eq. (2.30), after that the latter is being treated in a similar way as described above.

Appendix C

Surface tension distributions

Two surface tension distributions are tested:

- Case 1.
  Consider a bar of cotton wool wetted in ethanol. This bar is positioned just above the water layer at $x = 0$. Surface tension gradient S_x and surface tension S_{gr} are derived since ethanol is absorbed in the water just after $t = 0$. The ethanol start to spread over the surface of the layer and evaporates simultaneously. At $t = \beta$ all ethanol will have disappeared. This implies that at $x = 0$ $\sigma = \sigma_{water,air}$ (72.3×10^{-3}) for $t = 0$ and $t = \beta$. For $0 < t < \beta$ the properties are based on a normal distribution in time. In Fig. 2.6 plots of the surface tension gradient S_x and the surface tension S_{gr} are shown for $0 < t < \beta$. For $t > \beta$, $S_x = 0$ while $S_{gr} = \sigma_{water,air}/\Delta\sigma$, which implies that there is no effect of ethanol on the surface tension any more. It is assumed that the ethanol does not reach the right wall, so at $x = 1$ $\sigma = \sigma_{water,air}$ at all times t. Furthermore, at $x = 0$ and $x = 1$, $S_x = 0$ for all times t. Due to diffusion the gradient of the surface tension has a maximum moving in time from a location near $x = 0$ to the right and it reaches its largest value at $t = 0.35$. At $x = 0$ S_{gr} then has its lowest value. S_x and S_{gr} for $0 < t < \beta$ are given by:

$$S_x = \left\{ \sin\left[\pi \left(1 - (1-x)^{\frac{\beta}{t}}\right)\right] \frac{\pi}{t} (1-x)^{\frac{\beta}{t}} \frac{1}{1-x} \frac{4}{\beta^3} \right\} \times L \frac{(t\ (t-\beta))^2}{\sqrt{1 + \left(A \frac{\partial h}{\partial x}\right)^2}} \tag{C.1}$$

$$S_{gr} = \frac{\sigma_{water,air}}{\Delta\sigma} - \frac{4}{\beta^4} \left\{ 1 + \cos\left[\pi \left(1 - (1-x)^{\frac{\beta}{t}}\right)\right] \right\} (t\ (t-\beta))^2 \tag{C.2}$$

  with $\beta = \sqrt{2}/2$. The dimensionless surface tension S_{gr} equals $\sigma_{water,air}/\Delta\sigma$ at $x = 1$. These distributions are analogous to the ones used in the literature for similar models [13][14][16]. Gaver et al. [13][16] and Jensen et al. [14] consider the effect of an initially deposited surface monolayer of surfactants on the surface tension. They study transient effects during which surfactants absorb from the monolayer into the bulk. This surfactant distribution, and thus the driving force of the method, has a similar shape as the surface tension. The surface tension S_{gr} is similar to the spreading parameter as defined by Gaver et al. and Jensen et al.

- Case 2.
  This test case is constructed to study exchange of momentum in the fluid layer. By choosing a step function for the surface tension gradient the fluid is set into motion. The viscous shear stress takes care of the exchange of momentum with lower layers. This case is similar to the

diffusion problem, first analyzed by Rayleigh: an infinite plate that is suddenly put into motion with velocity V.

The governing equation is :

$$\frac{\partial u}{\partial t} = \nu \frac{\partial^2 u}{\partial y^2} \tag{C.3}$$

with $\nu = \mu/\rho$.
Initial and boundary conditions are:

$$\begin{array}{lll} t = 0 & u(x,y,0) = 0 & \\ t > 0 & y = 0 & u(x,0,t) = 0 \\ y \to \infty & u(x,\infty,t) \to V & \end{array} \tag{C.4}$$

The solution of the problem is given by:

$$\frac{u(x,y,t)}{V} = 1 - erf(\psi) \tag{C.5}$$

with $\psi = y/\sqrt{4\ \nu\ t}$ and $erf(\psi)$ the error function $2/\sqrt{\pi}\int_o^\psi e^{-x^2}dx$.

For the boundary layer thickness this solution yields, according to Rayleigh:

$$\delta = \alpha\sqrt{\nu t} \tag{C.6}$$

with ν the kinematic viscosity, t the time and α a constant depending on the configuration. Higher viscosities and larger times correspond to an increasing boundary-layer thickness.

S_x and S_{gr} are calculated using the leading term of the tangential stress condition $\tau = \mu\ \partial u/\partial y$ and are based on the solution given in Eq. (C.5). This means that a direct coupling between the prescribed surface tension gradient S_x and the established velocity gradient $\partial u/\partial y$ is realized.

Consider the velocity expansion of Eq. (2.16), which can be written by shifting the variable in x- and y-directions:

$$u = \sum_{k=0}^{n_{kc}-1} d_k\ \sin(\pi\ (k+1)\ x) \sum_{i=0}^{n_{ic}-1} d_i\ (\frac{y}{h})^{i+1} \tag{C.7}$$

In x-direction a parabolic function is fitted with the d_k-coefficients to the sine-series. In y-direction a function based on $e^{-\lambda(1-c)}$ is fitted with λ a time-dependent damping coefficient. This function is closely related to the error function and ensures that the gradient increases gradually in time. It is assumed that $\lambda = 60$ at $t = 0.01$ and $\lambda = 1$ at $t = 0.28$. At $y = 1$ this power function equals 1, for $y < 1$ it decreases quickly.

Multiplying the functions in x- and y-direction results in the velocity expansion in shifted variables. $\partial u/\partial y$ can easily be found by differentiating the velocity u. $y = h$ is substituted in $\partial u/\partial y$, since the surface tension gradient is prescribed at the interface. Now S_x is known from the tangential stress condition. The corresponding S_{gr} is calculated by $\int (S_x/L)\, ds$, see Eq. (2.8). The integration constant is evaluated imposing the surface tension difference between water and alcohol at the positions $x = 1$ and $x = 0$, respectively.

Appendix D

Analytical derivation of time-dependent b_m-coefficients

More details about this appendix are described by Pijnappel et al. [33].

D.1 Extra linear term

Let $\alpha_k = \sum_{i=0}^{n_{ic}-1} d_{i,k}/(i+2)$. Let N denote the value at which truncation takes place. Since the kinematic boundary condition is essential in the prediction of the time evolution of the interface, expansion 3.3 has been selected such that the kinematic boundary condition is satisfied for $N \to \infty$. The right-hand side and left-hand side are by this choice easily combined. Substituting Eq. (3.3) in Eq. (2.40) gives:

$$\begin{aligned}
\frac{d\tau_{l,r}}{dt} &= -\sum_{l=0}^{N}\Bigg[\sum_{r=1}^{n_{kc}-1}\Bigg\{\sum_{k=1}^{r}\frac{\alpha_k}{2}\Big((-1)^{l+1}(l+1)\tau_{l+1,r-k}+\pi r\tau_{l,r-k}\Big) \\
&\quad +\sum_{k=r}^{n_{kc}-1}\frac{\alpha_{k-1}}{2}\Big((l+1)\tau_{l+1,k-r}+(-1)^{l}\pi r\tau_{l,k-r}\Big)\Bigg\} \\
&\quad +\sum_{r=n_{kc}}^{\infty}\sum_{k=1}^{n_{kc}-1}\frac{\alpha_{k-1}}{2}\Big((-1)^{l+1}(l+1)\tau_{l+1,r-k}+\pi r\tau_{l,r-k}\Big) \\
&\quad +\sum_{r=0}^{\infty}\sum_{k=1}^{n_{kc}-1}\Bigg\{\frac{\alpha_{k-1}}{2}\Big((-1)^{l}(l+1)\tau_{l+1,r+k}+\pi r\tau_{l,r+k}\Big) \\
&\quad +\alpha_{n_{kc}-1}(l+1)\tau_{l,r}+\alpha_{n_{kc}-1}(-1)^{l}r\pi\tau_{l-1,r}\Bigg\}\Bigg]
\end{aligned} \tag{D.1}$$

D.2 Chebyshev polynomials

If Eqs. (3.5) and (3.6) are substituted in the kinematic boundary condition, Eq. (2.40), the db/dt-coefficient are found to be given by:

$$\begin{aligned}
\frac{db_0}{dt} &= -\sum_{k=0}^{n_{kc}-1}\sum_{i=0}^{n_{ic}-1}\frac{d_{i,k}}{i+2}\sum_{m=0}^{\infty}\max(2k+1,2m)b_m \\
\frac{db_r}{dt} &= -\sum_{k=0}^{n_{kc}-1}\sum_{i=0}^{n_{ic}-1}\frac{d_{i,k}}{i+2}\Bigg\{\sum_{m=\max(0,r-k)}^{\infty}(2k+2m+1)b_m
\end{aligned}$$

$$+\sum_{m=0}^{k-r}(2k-2m+1)b_m+\sum_{m=k+r+1}^{\infty}(-2k+2m-1)b_m\Bigg\} \quad \text{if } r>0 \tag{D.2}$$

$\sum_{\max(0,r-k)}^{\infty}$ denotes $\sum_{m=r-k}^{\infty}$ if $r>k$, and $\sum_{m=0}^{\infty}$ if $r<k$. ∞ in Eq. (D.2) is truncated at N, inducing a negligible error.

Appendix E

Thermovision system

The thermovision system produces images of the for human eyes invisible infrared thermal radiation emitted by the object focussed on. It contains among other things an optical-mechanical scanning mechanism, infrared transparent optics (sapphire windows and collimators system) and a detector. The detector is an Indium Antimonide (InSb)-photovoltaic cell, sensitive in the spectral range from 2 to 5.6 μm, called the middle infrared wavelength band. The detector is mounted in a Dewar vessel. This vessel is filled with liquid nitrogen to cool the detector to a temperature of -196 °C. At this temperature the detector obtains a maximum sensitivity. The intensity of the emission impinging on the detector is a measure for the temperature. Each photon has an energy as given by Eq. (4.1), so the number of photons per second per square meter gives the intensity. Since the InSb-detector counts photons, the number of photons is a measure for the local temperature at an instance. The relation between intensity and temperature is derived using Planck's formula and the Stefan-Boltzmann law. The former gives the spectral radiation distribution of a black body within a spectral interval of 1 μm at wavelength λ, W_{b_λ} in W/m$^2\mu$m:

$$W_{b_\lambda} = \frac{2\,\pi\,h\,c^2}{\lambda^5\left(e^{\left(\frac{h\,c}{\lambda\,k\,T}\right)}-1\right)} \times 10^{-6} \tag{E.1}$$

with: c the light velocity in vacuum, 3.0×10^8 m/s, h Planck's constant, 6.6×10^{-34} J/s, k Boltzmann's constant 1.4×10^{-23} J/K and T the absolute temperature in K. The latter results in the total radiant emittance (W_b) of a black body in W/m^2, obtained by integration of Planck's formula from $\lambda = 0$ to $\lambda = \infty$:

$$W_\lambda = \sigma\,T^4 \tag{E.2}$$

with σ the Stefan-Boltzmann constant, 5.7×10^{-8} W/(m^{2}K^4). From Planck's formula for a black body divided by the energy per photon, see Eq. 4.1, is written:

$$N_{b_\lambda} = \frac{2\,\pi\,c}{\lambda^4\left(e^{\left(\frac{h\,c}{\lambda\,k\,T}\right)}-1\right)} \tag{E.3}$$

with N_{b_λ} the spectral photon emittance. Using Stefan-Boltzmann's law the total radiant emittance is given by:

$$N_b = \frac{0.37\,\sigma\,T^3}{k} \tag{E.4}$$

with N_b the total photon emission counted by the detector per second and per square meter. Eq. (E.4) shows that the total photon emission per second and per square meter detected by the camera, and thus the intensity, is proportional to the third power of the absolute temperature. In practice, this

relation means that for temperatures outside the range of 20 to 40 °C calibration curves must be made and that the relation is linear for temperatures inside this range. For an opaque grey body the number of photons emitted at a specific temperature is $N_b = \epsilon\ 0.37\ \sigma\ T^3/k$, with ϵ the emission coefficient.

The intensity from the scanner impinging on the detector generates an electrical voltage signal. The amplitude of the signal varies according to the point by point temperature variation along the surface of the object as it is being scanned by the camera. This signal is via an AD converter translated into an 8-bits number $(0-255)$, representing the local temperature, which is transported to a 486-PC. Software is used written for our purposes specifically to detect these signals, to present them on a screen and to store them on disk. In this way postprocessing of the results enables us to interpret the measurements more easily. The PC is via a multilab (data acquisition system) connected to a Pt-100 element, used for calibration purposes. Software is implemented to facilitate calibrations.

Appendix F

Sensadyne 6000 surface tension meter

A constant volume flow of an inert gas (nitrogen) is bubbled slowly through two probes of different radii (r_1 and r_2) immersed in the test fluid. Therefore, below the tubes gas-bubbles are formed, see Fig. F.1. The maximum pressure is obtained when the radius of the bubble-curvature is minimum. The

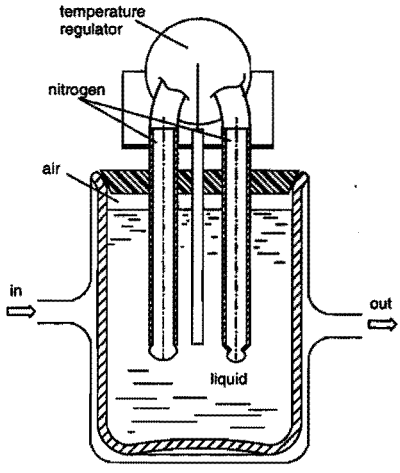

Figure F.1: Set-up of SensaDyne surface tension meter

differential pressure signal ΔP is measured by means of a differential pressure transducer, see Fig. F.2, consisting of a thin stainless steel diaphragm between two cavities inside a body. The diaphragm flexes to one side or the other in response to the pressure of the bubbles at the two orifices. The pressure drop is a measure for the fluid surface tension σ through the relation:

$$\Delta p = p_1 - p_2 = (\rho g L + \frac{2\sigma}{r_1}) - (\rho g L + \frac{2\sigma}{r_2}) \tag{F.1}$$

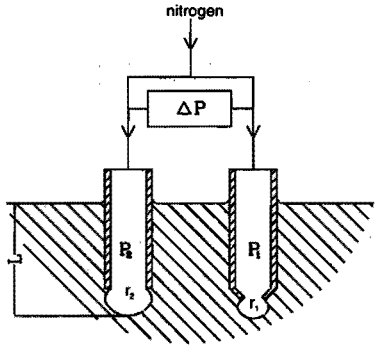

Figure F.2: Principle of surface tension meter

with L the depth in the fluid. The nitrogen expands slowly, so inertia forces are negligible. The probes are placed at equal depth L in the fluid, so:

$$\Delta p \;=\; p_1 - p_2 = \frac{2\sigma}{r_1} - \frac{2\sigma}{r_2} \tag{F.2}$$

Pressure variation is established since the rate of bubble formation at the small orifice is larger than that of the larger orifice. Therefore the pressure transducer contains cascaded pressure regulators to control and regulate these pressure variations. Separate metering valves at each orifice control the bubble time-rate frequency selection and the bubble rate ratio of the large to the small orifice. The differential pressure signal measured by the pressure transducer is a combination of the separate pressures which are measured at both orifices. Due to the differences in bubble rate frequency at both orifices the signal of the pressure transducer is not periodical. Therefore Eq. (F.2) is not directly applicable to determine the surface tension. However, the surface tension sensor package includes a filter circuit which separates the original pressure signal at both the orifices from the differential pressure signal. Next, the variation in amplitude of the pressure at the large orifice is filtered from the resulting signal which is a measure for Δp of Eq. (F.2). Now the surface tension can be determined from Eq. (F.2).

Appendix G

Velocity measurements

Velocity measurements of the experiments.

experiment	time [s]				distance [mm]	u [mm/s]				u avg. [mm/s]
1	5.5	5.2	4.8	3.8	8.5	1.55	1.63	1.77	2.18	1.76 ± 0.22
	3.9	5.2	6.8	5.0	8.7	2.23	1.67	1.28	1.74	
2	5.2	4.5	4.0	4.2	8.5	1.63	1.89	2.13	2.02	1.72 ± 0.21
	6.1	6.0	5.4	6.0	8.7	1.50	1.21	1.53	1.85	
3	5.5	6.1	5.3	5.8	8.5	1.55	1.39	1.60	1.47	1.43 ± 0.18
	6.1	6.0	5.4	6.0	8.7	1.43	1.45	1.61	1.45	
	8.4	5.6	7.0	7.0	8.5	1.01	1.52	1.21	1.21	
	5.2	5.6	6.7	7.0	8.7	1.67	1.55	1.30	1.24	
4	7.2	7.5	6.4	-	8.5	1.17	1.12	1.31	-	1.21 ± 0.15
	6.7	6.7	7.8	-	8.7	1.28	1.28	1.10	-	

Table G.1: Velocity measurement of the experiments. The (averaged) velocity for various particles are determined by measuring the time needed to travel along two paths between two sets of vertical lines, one 8.5 and one 8.7 mm apart, respectively.

Appendix H

Temperature gradient measurements

The temperature gradient measurement ($\Delta T/\Delta x$) of the experiments for various times are shown in this appendix. The temperature difference (ΔT) is determined over the part of the cavity where the temperature varies linearly (Δx) at $z = 0$ (in the middle of the cavity).

time [s]	ΔT [K]	Δx [mm]	$\Delta T/\Delta x$ [K/mm]
39	4.9	28.3	0.17 ± 0.01
52	4.7	30.9	0.15 ± 0.01
65	4.9	30.9	0.16 ± 0.01
78	4.5	30.9	0.15 ± 0.01
91	6.6	32.8	0.20 ± 0.01
104	4.7	27.1	0.17 ± 0.01
118	5.7	27.1	0.21 ± 0.01

Table H.1: Temperature gradient in x-direction for experiment 1.

time	ΔT	Δx	$\Delta T/\Delta x$
65	2.2	12.4	0.18 ± 0.03
78	2.2	11.7	0.19 ± 0.03
98	4.1	18.0	0.23 ± 0.02
131	4.0	13.1	0.30 ± 0.03

Table H.2: Temperature gradient in x-direction for experiment 2.

time	ΔT	Δx	$\Delta T/\Delta x$
39	3.1	19.4	0.16 ± 0.02
59	3.5	23.5	0.15 ± 0.01
65	4.4	26.9	0.16 ± 0.01
69	5.3	27.6	0.19 ± 0.01
72	5.4	26.3	0.20 ± 0.01
78	5.9	29.0	0.20 ± 0.01
85	6.3	28.3	0.22 ± 0.01

Table H.3: Temperature gradient in x-direction for experiment 3.

time	ΔT	Δx	$\Delta T/\Delta x$
78	4.3	35.3	0.12 ± 0.01
91	4.1	25.8	0.16 ± 0.01
104	5.3	25.8	0.20 ± 0.01
118	7.8	25.8	0.30 ± 0.01

Table H.4: Temperature gradient in x-direction for experiment 4.

Appendix I

Thermocouple measurements

The results from five thermocouple measurements in n-paraffin $C_{10} - C_{13}$ (situation 1, see Fig. 4.11) are tabulated in tables I.1, I.2, I.3, I.4 and I.5. At $t = 0$ s the voltage over the wire is switched on. At $t = 30$ s the temperature of the first thermocouple is registered, subsequent thermocouples are read after each 5 s. For every experiment the interpolated values for the temperatures at four successive instants in time are given using the temperature measurements.

exp. 1	T_1	T_2	T_3	T_4	T_5	T_6	T_7	T_8	T_9
t=70	23.6	25.1	26.2	24.0	23.5	24.7	21.7	21.0	21.2
t=115	26.4	27.5	28.4	26.6	25.6	27.0	23.0	21.8	22.1
t=160	28.5	29.3	29.8	29.0	27.4	29.0	24.3	22.8	23.1
t=205	30.0	30.7	31.2	30.7	28.9	30.6	25.4	23.7	24.2

Table I.1: Thermocouple experiment 1 with n-paraffin $C_{10} - C_{13}$ in situation 1.

The results of the thermocouple measurements (situation 2, see Fig. 4.12) of n-paraffin $C_{10}-C_{13}$ are tabulated in table I.6, I.7, I.8 and I.9 of glycerol in table I.10 and in water in table I.11. At $t = 0$ s the voltage over the wire is switched on. At $t = 5$ s the temperature of the first thermocouple is registered, subsequent thermocouples are read after each 5 s. For every experiment the interpolated values for the temperatures at four successive instants in time are given using the temperature measurements.

exp. 2	T_1	T_2	T_3	T_4	T_5	T_6	T_7	T_8	T_9
t=70	22.9	23.7	24.6	22.8	22.2	23.5	20.9	20.4	20.6
t=115	25.8	26.7	27.2	25.4	24.1	25.6	22.0	21.2	21.3
t=160	27.2	28.1	28.7	27.2	25.6	27.2	23.0	21.9	22.2
t=205	28.4	28.7	29.1	28.5	26.8	28.5	24.0	22.8	23.1

Table I.2: Thermocouple experiment 2 with n-paraffin $C_{10} - C_{13}$ in situation 1.

exp. 3	T_1	T_2	T_3	T_4	T_5	T_6	T_7	T_8	T_9
t=70	22.5	23.6	24.3	22.3	21.7	23.0	20.5	20.2	20.3
t=115	25.0	25.9	26.5	24.7	23.5	25.0	21.5	20.8	21.0
t=160	26.5	27.3	28.0	26.5	25.0	26.6	22.5	21.5	21.8
t=205	27.8	28.5	28.7	28.0	26.4	28.0	23.6	22.3	22.7

Table I.3: Thermocouple experiment 3 with n-paraffin $C_{10} - C_{13}$ in situation 1.

exp. 4	T_1	T_2	T_3	T_4	T_5	T_6	T_7	T_8	T_9
t=70	22.1	23.5	24.3	22.0	21.5	22.7	20.3	19.9	20.0
t=115	24.2	25.7	26.4	24.1	23.1	24.5	21.2	20.5	20.7
t=160	25.8	27.0	27.6	25.8	24.5	25.9	22.1	21.2	21.5
t=205	27.2	28.3	29.0	27.1	25.6	27.2	23.1	21.9	22.2

Table I.4: Thermocouple experiment 4 with n-paraffin $C_{10} - C_{13}$ in situation 1.

exp. 5	T_1	T_2	T_3	T_4	T_5	T_6	T_7	T_8	T_9
t=70	23.5	24.9	25.9	23.2	22.5	23.8	21.1	20.7	20.9
t=115	25.5	26.7	27.6	25.5	24.3	25.8	22.1	21.4	21.6
t=160	27.3	28.0	28.7	27.2	25.8	27.3	23.2	22.2	22.4
t=205	28.4	29.0	29.4	28.6	27.0	28.6	24.2	22.9	23.3

Table I.5: Thermocouple experiment 5 with n-paraffin $C_{10} - C_{13}$ in situation 1.

exp. 6	T_1	T_2	T_3	T_4	T_5	T_6	T_7	T_8	T_9
t=45	23.6	25.5	26.3	23.8	24.0	24.7	22.7	22.4	23.3
t=90	28.0	31.3	31.9	27.9	28.0	30.6	25.0	24.3	26.2
t=135	32.4	36.0	36.4	32.5	31.7	34.9	27.5	26.1	29.0
t=180	36.0	39.9	40.0	36.5	35.0	38.5	30.0	28.1	31.9

Table I.6: Thermocouple experiment 6 with n-paraffin $C_{10} - C_{13}$ in situation 2.

exp. 7	T_1	T_2	T_3	T_4	T_5	T_6	T_7	T_8	T_9
t=45	29.4	30.8	31.1	29.1	29.1	31.0	26.6	26.5	28.4
t=90	38.0	40.0	40.8	38.1	36.4	40.2	31.7	29.1	33.0
t=135	45.4	47.4	48.7	46.2	42.8	47.9	35.7	32.7	38.1
t=180	51.1	53.4	54.9	52.6	48.6	53.7	39.9	36.3	43.0

Table I.7: Thermocouple experiment 7 with n-paraffin $C_{10} - C_{13}$ in situation 2.

exp. 8	T_1	T_2	T_3	T_4	T_5	T_6	T_7	T_8	T_9
t=45	24.3	25.8	26.6	24.4	24.3	25.1	22.8	22.8	23.8
t=90	28.9	31.1	31.3	28.8	28.2	30.3	25.5	24.5	27.0
t=135	30.6	34.9	35.4	32.6	31.3	31.1	27.5	26.0	29.0
t=180	35.9	38.1	38.9	35.7	33.9	37.0	29.4	27.7	31.2

Table I.8: Thermocouple experiment 8 with n-paraffin $C_{10} - C_{13}$ in situation 2.

exp. 9	T_1	T_2	T_3	T_4	T_5	T_6	T_7	T_8	T_9
t=45	28.4	28.6	29.4	27.4	26.7	28.3	24.4	24.4	26.7
t=90	35.5	35.8	37.2	34.7	32.6	35.7	28.4	26.6	30.0
t=135	41.8	42.2	43.9	40.9	37.6	41.7	31.6	29.3	33.5
t=180	46.6	47.7	49.7	46.4	37.5	46.5	34.9	32.1	37.3

Table I.9: Thermocouple experiment 9 with n-paraffin $C_{10} - C_{13}$ in situation 2.

exp. 10	T_1	T_2	T_3	T_4	T_5	T_6	T_7	T_8	T_9
t=180	-	29.2	30.3	28.7	29.2	29.6	28.9	29.3	29.4
t=360	-	29.8	31.8	28.9	29.7	30.7	28.9	29.5	31.1
t=540	29.6	31.3	33.6	29.3	31.2	32.7	29.3	30.5	31.7
t=720	31.0	33.0	36.0	30.6	32.8	34.7	30.3	31.8	33.2
t=900	32.5	34.4	37.2	31.9	34.0	36.0	31.3	32.8	34.6

Table I.10: Thermocouple experiment 10 with glycerol in situation 2.

exp. 11	T_1	T_2	T_3	T_4	T_5	T_6	T_7	T_8	T_9
t=45	22.6	22.0	22.9	22.0	22.2	22.4	22.0	21.9	22.0
t=90	23.1	23.6	24.9	22.7	23.0	23.9	22.5	22.3	22.6
t=135	24.2	25.4	25.8	24.1	24.3	25.1	23.2	22.9	23.5
t=180	25.0	26.9	26.6	25.4	25.4	26.0	23.7	23.5	29.5

Table I.11: Thermocouple experiment 11 with water in situation 2.

List of symbols

Symbols

A	aspect ratio, $A = h_0^*/L$	[-]
a, b, d	time-dependent spectral coefficients	[-]
Bo	Bond number, $Bo = \rho\ g\ L^2/\sigma$	[-]
c	dimensionless height, y/h, see chapter 2	[-]
	dimensionless radius, r/R, see chapter 5	[-]
	heat capacity, see chapter 4 and 6	[J/(kgK)]
D	$D \equiv A\ \partial h/\partial x$, see Eq. (2.12)	[-]
e	$e = \partial d/\partial t$	[-]
f_k	function	[-]
g	gravity constant: 9.81	[m/s^2]
Gr	Grashof number, $Gr = \beta\ g\ \Delta T\ L^3/\nu^2$	[-]
h	interfacial height, $h = h(x,t)$	[m]
H	cavity height	[m]
j	number of significant singular values of equations resulting from contour integrals	[-]
L	cavity length	[m]
Ma	Marangoni number, $Ma = (\partial\sigma/\partial T)\ \Delta T\ L/(\rho\ \nu\ \kappa)$	[-]
N	$N \equiv (1 + D^2)^{1/2}$, see Eq. (2.14)	[-]
n_b	number of coefficients in expansion of interfacial height, see chapter 2	[-]
	number of coefficients in expansion of interfacial radius, see chapter 5	[-]
n_i	number of collocation points in y-direction, see chapter 2	[-]
	number of collocation points in r-direction, see chapter 5	[-]
n_{ic}	highest power of polynomial-expansion in y-direction, see chapter 2	[-]
	highest power of polynomial-expansion in r-direction, see chapter 5	[-]
n_k	number of collocation points in x-direction, see chapter 2	[-]
	number of collocation points in θ-direction, see chapter 5	[-]
n_{kc}	highest mode of Fourier-expansion in x-direction, see chapter 2	[-]
	highest order of polynomial in θ-series, see chapter 5	[-]

n_l	number of exponential functions	[-]
p	pressure	[N/m^2]
r	number of significant singular values of tangential stress condition	[-]
R	interfacial radius of drop	[mm]
Re	Reynolds number, $Re = \Delta\sigma\ A\ h_0^*\ \rho_0/\mu^2$, see Eq. (2.8)	[-]
R_m, R_p, R_s	defined functions, see chapter 5	[-]
R_1, R_2	radii of curvature	[mm]
S_{gr}	$S_{gr} = \sigma/\Delta\sigma$	[-]
S_x	surface tension gradient in x-direction	[-]
t	time	[s]
T_k	Chebyshev polynomial	[-]
u	velocity component in x-direction, $u = u(x, y, t)$	[m/s]
v	velocity component in y-direction, $v = v(x, y, t)$	[m/s]
W	cavity width	[m]
r, s, x, y, z	coordinates	[m]

Greek symbols

β	parameter of surface tension profile, see Eq. (C.1)	[-]
	volumetric expansion coefficient, see chapter 4	[1/K]
θ, ϕ, φ	angle	[rad]
κ	thermal diffusivity, $\kappa = \lambda/(\rho c)$	[m^2/s]
$\Delta\sigma$	spreading parameter, see Eq. (C.2)	[N/m]
Δt	timestep	[-]
ΔT	temperature difference	[K]
λ	eigenvalue	[-]
	heat conductivity	[W/(mK)]
μ	dynamic viscosity	[Ns/m^2]
ν	kinematic viscosity	[m^2/s]
ρ	mass density	[kg/m^3]
σ	surface tension	[N/m]
τ	cubic spline functions, see chapter 5	[-]

Subscripts

a	average
g	gas
i, k, m	integers
li	liquid
0	initial

Superscripts

*	dimensional, see chapter 2 and 3 and section 7.2
^{T}	transposed
$'$	matrix or vector with deficient rank

Summary

In the design of process equipment the prediction of fluid flow and gas-liquid interface behaviour is of great importance. A gradient of the surface tension along a gas-liquid interface causes forces that sometimes dominate the liquid flow. The resulting so-called Marangoni convection is studied both numerically and experimentally for two configurations:

- A thin liquid layer in a cavity heated from above by a straight wire.
- An axisymmetrical droplet on a plate cooled uniformly from below.

A numerical method is presented that predicts the time evolution of the velocity field and the interface deformation caused by the Marangoni effect. The algorithm simultaneously solves the tangential stress boundary condition at the free interface and the so-called contour integrals. These contour integrals combine the Navier-Stokes equations and the normal stress boundary condition. An adapted Singular Value Decomposition (SVD) method is employed in the approach which automatically weights the importance of the contour integrals and that of the tangential stress condition.

The method is found to accurately reproduce an analytical solution for a heated thin liquid layer in steady motion. The velocity expansion converges rapidly and the tangential stress condition at the interface is satisfied within adequate order of magnitude. Variation of the parameters of the algorithm, such as the number of collocation points, the number of expansion coefficients, the viscosity and aspect ratio showed that the algorithm is robust and established some parameter limitations. Alternative expansions are recommended to accommodate specific sets of boundary conditions. Results of the numerical simulation are comparable with results of similar investigations found in the literature.

The temperature gradient along the interface of a liquid layer is measured and the flow in the bulk of the liquid is visualized. A quasi-stationary flow is established during the first 90 s of heating with an almost constant surface tension gradient.

In the droplet experiments, the temperature gradient increases from the top to the foot of the droplet. Also velocities increase in this direction. In time, the temperature gradient vanishes since the Marangoni flow homogenizes the temperature in the droplet. Small roll-cells near the foot of the droplet are observed and larger roll-cells elsewhere.

The predicted velocities in the liquid layer are in quantitative agreement with the measured velocities. The predicted flow pattern in the droplet corresponds well to the flow pattern observed in the experiments.

Samenvatting

Het voorspellen van vloeistofstromingen en het gedrag van gas-vloeistof grensvlakken is voor het ontwerpen van proces-installaties van groot belang. Een gradiënt in de oppervlaktespanning aan een gas-vloeistof grensvlak veroorzaakt krachten die soms de stromingen in de vloeistof domineren. De ontstane stromingen, Marangoni convectie genoemd, worden zowel numeriek als experimenteel bestudeerd voor twee configuraties:

- Een dunne vloeistoflaag in een caviteit die van bovenaf wordt opgewarmd door een rechte draad parallel aan het grensvlak.
- Een axisymmetrische druppel op een plaat die van onderaf uniform wordt gekoeld.

Een numerieke methode wordt gepresenteerd die de tijdsevolutie van het snelheidsveld en de grensvlak-vervorming voorspelt die worden veroorzaakt door het Marangoni effect. Het algoritme voldoet aan de tangentiële spanningsvoorwaarde aan het vrije grensvlak, tegelijkertijd wordt voldaan aan de contourintegralen. Deze contourintegralen combineren de Navier-Stokes vergelijkingen met de normale spanningsvoorwaarde aan het interface. Een aangepaste singuliere waarde ontbinding (SVD) is toegepast die automatisch het belang van de contourintegralen en dat van de tangentiële spanningsvoorwaarde weegt.

De methode reproduceert de uit de literatuur bekende analytische oplossing voor een verwarmde, dunne vloeistoflaag. De snelheidsexpansie convergeert snel en aan de tangentiële spanningsvoorwaarde aan het grensvlak wordt overal voldaan binnen een bepaalde nauwkeurigheid. Parameter-variatie zoals het aantal collocatiepunten, het aantal expansie-coëfficiënten, de viscositeit en de hoogte/breedte verhouding tonen aan dat het algoritme robuust is en laten zien hoe het model kan worden toegepast. Alternatieve expansies zijn gevonden en gebruikt om te kunnen voldoen aan specifieke sets van randvoorwaarden. Simulatie-resultaten zijn vergelijkbaar met die van vergelijkbare onderzoek uit de literatuur.

De temperatuurgradiënt aan het grensvlak van een vloeistoflaag is gemeten en de stromingen in de vloeistoflaag zijn gevisualiseerd. Gedurende de eerste 90 s ontstaat een quasi-stationaire stroming met vrijwel constante oppervlaktespanningsgradiënt.

Uit experimenten met een druppel blijkt de temperatuurgradiënt van top tot voet van de druppel toe te nemen. De snelheden nemen ook toe in deze richting. De temperatuurgradiënt neemt af in de tijd omdat de Marangoni stroming de temperatuur in de druppel homogeniseert. Kleine circulaire cellen bij de voet van de druppel en grotere op andere plaatsen zijn waargenomen.

De voorspelde snelheden in de vloeistoflaag stemmen kwantitatief overeen met de gemeten snelheden. Het voorspelde stromingspatroon in de druppel komt goed overeen met het stromingspatroon zoals waargenomen in de experimenten.

Dankwoord

Ongeveer 4 jaar geleden kreeg ik de mogelijkheid door te gaan met het onderzoek naar Marangoni convectie, waarop ik destijds ben afgestudeerd. Het leek me een uitdaging om me verder te verdiepen in dit onderzoek. Dit proefschrift is voortgekomen uit deze 4 jaar onderzoek. Het is zeer de moeite waard geweest en ik heb veel geleerd van wetenschap en de wereld daaromheen.

Als stuwende kracht heb ik altijd kunnen rekenen op Cees van der Geld. Op het wetenschappelijk vlak heeft hij me altijd met raad en daad bijgestaan, en hij was een enorme stimulans vooral tijdens de periode waarin dit proefschrift werd geschreven.

Wim Pijnappel heeft me enorm geholpen bij de wiskundige aspecten van het werk en het programmeren. Vele discussies (bij hem thuis) en telefoongesprekken zijn gevoerd om ideeën uit te wisselen.

Ik heb het genoegen gehad met Bob Brand en Frank Ganzevles te mogen samenwerken op één kamer. Zij hebben me enorm geholpen met computer-aangelegenheden en bij het beantwoorden van de vele "domme" vragen die ik ze hieromtrent stelde. Ik heb alle voor- en nadelen van Word en Latex regelmatig de revue horen passeren tijdens hun discussies. Ondanks dat onze werkplek voor studenten een zoete inval was en de telefoon vaak roodgloeiend stond, zodat ik regelmatig van mijn werk werd afgeleid, kijk ik met plezier terug op deze periode.

Tijdens mijn promotie heb ik hulp gehad van verschillende afstudeerders en vele stagiaires uit binnen- en buitenland. In alfabetisch volgorde hebben meegewerkt: Octaaf Eggermont, Thomas Ernst, Olivier Fallet, Peter Krijnen, Konrad Maestre, Markus Merkel, Peter Myrczik, Charles Norden, Michael Rantik, Carlo Simons en Sandra Sluijpers. Zij hebben me veel werk uit handen genomen.

Gedurende het laatste jaar is het schrijven van dit proefschrift de hoofdzaak geweest. De promotoren prof. ir. J.K. Nieuwenhuizen en prof. dr. ir. H.W.M. Hoeijmakers hebben me hierbij geholpen. De discussies met hen hebben een wezenlijke bijdrage geleverd aan het ontstaan van dit proefschrift. De overige leden van de promotiecommissie hebben met opbouwende kritiek mijn proefschrift becommentarieerd.

Toon Schoonen, Piet Boot, Jacques Verspagen, Klaas Amersfoort en Frits van Veghel hebben elk op hun eigen manier bijgedragen aan de totstandkoming van dit proefschrift.

Alle mensen die ik hierboven heb genoemd wil ik van harte bedanken. Zonder hen zou dit proefschrift niet zijn ontstaan.

Als laatste wil ik Chantal bedanken voor haar steun tijdens deze 4 jaar die vooral tijdens de drukke tijd van het schrijven onontbeerlijk is geweest.

Curriculum Vitae

17–08–1968	:	Born in Tilburg, the Netherlands.
05–1985	:	HAVO diploma,
05–1987	:	VWO diploma, at Cobbenhagencollege in Tilburg.
07–1992	:	M.Sc. degree in Mechanical Engineering and Biomedical Engineering at the Eindhoven University of Technology.
08–1992 / 09–1996	:	Ph.D. research student at the Eindhoven University of Technology, section Multiphase Flow with Heat Transfer.

Bibliography

[1] C.W.M. van der Geld and H.J.H. Brouwers. *The mean condensate heat resistance of dropwise condensation with flowing, inert gases.* Int. J. Heat and Mass Transfer, **30**, pp. 435-445, (1995).

[2] R. Velten, D. Schwabe, and A. Scharmann. *Gravity-dependence of the instability of surfaces-tension-driven flow in floating zones.* Proc. VIIth European Symp. on materials and fluid sciences in microgravity, ESA-report SP-295, (1990).

[3] M. Lacroix. *Effects of buoyancy and surface tension forces on the melting of a metal.* Num. Heat Transfer, part A, **19**, pp. 101-115, (1991).

[4] B. Petri, A. Delgado, and H.J. Rath. *Marangoni convection in spherical drops driven by rotationally symmetrical temperature fields under microgravity.* Proc. VIIth European Symp. on Materials and Fluid Sciences in Microgravity, ESA-report SP-295, (1990).

[5] R. Monti and R. Fortezza. *Oscillatory marangoni flow in a floating zone: design of a telescience experiment for Texus 23. rm Proc. VIIth European Symp. on materials and fluid sciences in microgravity, ESA-report SP-295*, (1990).

[6] W. R. Hu and Z. M. Tang. *Thermocapillary oscillatory convection in floating-zone simulation.* Proc. VIIth European Symp. on materials and fluid sciences in microgravity, ESA-report SP-295, (1990).

[7] H. Grunditz, M. Mathes, and G. Wozniak. *Fluid science module in maser 3 description and flight results.* Proc. VIIth European Symp. on materials and fluid sciences in microgravity, ESA-report SP-295, (1990).

[8] L. Blumenfeld and Soubbaramayer. *Combined effect of buoyancy and of interfacial phenomena on the heat transfer coefficient at the melt surface on an eb evaporator.* 7-FM-3, pp. 13-18.

[9] C.W. Lan and Sindu Kou. *Thermocapillary flow and natural convection in a melt column with an unknown melt/solid interface.* Int. J. for numerical methods in fluids, **12**, pp. 59-80, (1991).

[10] A. Cröll, W. Müller-Sebert, and R. Nitsche. *Transition from steady to time-dependent marangoni convection in partially coated silicon melt zones.* Proc. VIIth European Symp. on materials and fluid sciences in microgravity, ESA-report SP-295, (1990).

[11] H.C.J. Hoefsloot. Marangoni convection under microgravity conditions. PhD thesis, Groningen University, The Netherlands, (1992).

[12] J. Marra and J.A.M. Huethorst. *Physical principles of Marangoni drying.* Langmuir, **7**, pp. 2748-2755, (1991).

[13] D.P. Gaver and J.B. Grotberg. *The dynamics of a localized surfactant on a thin film.* J. Fluid Mech., **213**, pp. 127-148, (1990).

[14] O.E. Jensen and J.B. Grotberg. *The spreading of heat or soluble surfactant along a thin liquid film.* Phys. Fluids A, **5**, (1), pp. 58-68, (1993).

[15] D.J.M. Bergink-Martens. Interface dilation. The overflowing cylinder technique. PhD thesis, Wageningen University, The Netherlands, (1993).

[16] D.P. Gaver and J.B. Grotberg. *Dynamics and transport of a localized soluble surfactant on a thin film.* J. Fluid Mech., **237**, pp. 1-11, (1992).

[17] D. Raake and J. Siekmann. *Temperature and velocity fields due to surface tension driven flow.* Experiments in Fluids, **7**, pp. 164-172, (1989).

[18] W. v. Helden. On detaching bubbles in upward flow boiling. PhD thesis, Eindhoven University of Technology, (1994).

[19] C.A. Brebbia and J. Dominguez. Boundary elements. An introductory course. pp. 292. Computational Mechanics Publications, (1989).

[20] A.A. van Steenhoven. *De toepassing van de eindige elementenmethode bij stromingsproblemen.* Technical Report 4K030, Fac. of Mech. Eng., Eindhoven Univ. Techn., Eindhoven, The Netherlands, (1984).

[21] Susumu Kotake and Kunio Hijikata. Numerical simulations of heat transfer and fluid flow on a Personal Computer. Elsevier, (1993).

[22] A. Quarteroni C. Canuto, M.Y. Hussaini and T.A. Zang. Spectral methods in fluid dynamics. Springer-Verlag, (1988).

[23] Wen qiang Lu. *Boundary element analysis of thermocapillary convection with a free surface in a rectangular cavity.* Int. J. Heat Mass Transfer, **37**, pp. 1063-1071, (1994).

[24] M. Strani, R. Piva, and G. Graziani. *Thermocapillary convection in a rectangular cavity: Asymptotic theory and numerical simulation.* J. Fluid Mech., **130**, pp. 347-376, (1983).

[25] P.J. Shopov, P.D. Minev, and I.B. Bazhlekov. *Numerical method for unsteady viscous hydrodynamical problem with free boundaries.* Int. J. Num. Methods in Fluids, **14**, pp. 681-705, (1992).

[26] M.Y. Hussaini, D.A. Kopriva, and A.T. Patera. *Spectral collocation methods. Appl. Num. Math.*, **5**, pp. 177-208, (1989).

[27] Nengli Zhang and Wen-Jei Yang. *Evaporative convection in minute drops on a plate with temperature gradient.* Int. J. Heat and Mass Transfer, **26**, (10), pp. 1479-1488, (1983).

[28] S. Ostrach and A. Pradhan. *Surface-tension induced convection at reduced gravity.* AAIA Journal, **16**, (5), pp. 419-424, (1978).

[29] J.C. Legros, M.C. Limbourg-Fontaine, and G. Petre. *Surface tension minimum and Marangoni convection.* Proc. of Fluid dynamics and space, ESA-report SP-265, (1986).

[30] C.W.M. van der Geld, A.W.J.P. den Boer, and W.W.F. Pijnappel. *Tests of a numerical model for Marangoni driven convection.* Proc. of 31th European Two-Phase Flow Group Meeting, (1994).

[31] E.L. Koschmieder and S.A. Prahl. *Surface-tension-driven Bénard convection in small containers.* J. Fluid Mech., **215**, pp. 571-583, (1990).

[32] R.A. Pearson. *On convection cells induced by surface tension.* J. Fluid Mech., **4**, pp. 489-500, (1958).

[33] W.W.F. Pijnappel and C.W.M. van der Geld. *Some aspects of a new algorithm for Marangoni convection.* Technical Report WFW-96.101, Fac. of Mech. Eng., Eindhoven Univ. Techn., Eindhoven, The Netherlands, (1996).

[34] L.D. Landau and E.M. Lifshitz. Fluid mechanics; Course of theoretical physics, **6**, pp. 236-337. Oxford: Pergamon Press, (1959).

[35] M.C. Limbourg and Ph. Georis. *Preliminary results of texus 19 (TEMO6-8) experiment: Marangoni convection around a surface tension minimum.* Proc. 7^{th} European Symp. on Materials and Fluid Sciences in Microgravity, ESA-report SP-295, (1990).

[36] D. Schwabe, O. Dupont, P. Queeckers, and J.C. Legros. *Experiments on Marangoni-Bénard instability problems under normal and microgravity conditions.* Proc. VIIth European Symp. on Materials and Fluid Sciences in Microgravity, ESA-report SP-295, (1990).

[37] J.A. Szymczyk, J. Siekman, Ch.H. Chun, and K. Wozniak. *Liquid crystal tracers as a method for thermocapillary flow diagnostics.* Arch. Mech., **41**, (2-3), pp. 351-360, (1989).

[38] G. Wozniak and K. Wozniak. *Simultaneous measurement of the temperature and velocity field in the thermocapillary convection of a bubble.* Technical report, Univ.-GH-Essen, D-4300 Essen 1, Germany.

[39] A.W.J.P. den Boer and C.W.M. van der Geld. *Thermocapillary convection in a liquid layer heated from above.* Proc. of 2^{nd} European Thermal-Sciences and 14^{th} UIT National Heat Transfer Conference, (1996).

[40] L.P.B.M. Janssen and M.M.C.G. Warmoeskerken. Transport phenomena data companion. pp. 292. Delftse Uitgevers Maatschappy, (1987).

[41] J.A. Szymczyk and J. Siekman. *Experimental investigation of the thermocapillary flow along cylindrical interfaces under rotation.* Proc. VIIth European Symp. on Materials and Fluid Sciences in Microgravity, ESA-report SP-295, (1990).

[42] Thermodynamics Research Center. Selected infrared spectral data, **391** , pp. 161-236. College Station: Texas A & M University, (1968).

[43] J. Sillekens. Laminar mixed convection in ducts. PhD thesis, Eindhoven University of Technology, (1995).

[44] Y.S. Kao and D.B.R. Kenning. *Thermocapillary flow near a hemispherical bubble on a heated wall.* J. Fluid. Mech., **53**, (4), pp. 715-735, (1972).

[45] A.W.J.P. den Boer and C.W.M. van der Geld. *Thermocapillary convection and interfacial deformation of a hemispherical drop.* Computational modelling of free and moving boundary problems III: Proc. of Third International Conference on Moving Boundaries, (1995).

[46] F.L.A. Ganzevles and C.W.M. van der Geld. *In-situ measurements of wetting rate and local temperatures with dropwise condensation in a compact heat exchanger.* Proc. of 24^{th} National Heat Transfer Conference, (1995).

[47] Yeong-Jen Su and Wen-Jei Yang. *Thermocapillary convection in evaporating sessile drops with internal solidifications.* Proc. of the International Energy and Mass Transfer Conference, (1994).

[48] A.J.J. van der Zanden. The hydrodynamics of a moving fluid-liquid contact line. PhD thesis, Eindhoven University of Technology, (1993).

[49] J.K. Platten and D. Villers. *On thermocapillary flows in containers with differentially heater side walls.* Physicochemical Hydrodynamics, Interfacial Phenomena., NATO ASI Series. Series B: Physics. Edited by M.G. Velarde., (174), pp. 1111, (1986).

[50] Y.S. Ryazantsev, V.M. Shevtsova, and Y.V. Val'tsiferov. *Effect of the form of the temperature dependence of surface tension on motion and heat transfer in a layer of liquid during local heating.* Translated from Inzhenerno-Fizicheskii Zhurnal, **57**, (1), pp. 27-33, (1989).

[51] M. Bestehorn and H. Haken. *A calculation of transient solutions describing roll and hexagon formation in the convection instability.* Physics letters, **99A**, (6.7), pp. 265-267, (1983).

List of Figures

List of Tables

STELLINGEN

behorende bij het proefschrift

Marangoni Convection: Numerical Model and Experiments

1. De twee-dimensionale stromingsmethode, zoals beschreven in hoofdstuk 2 van dit proefschrift, kan worden aangewend in een methode waarbij het rekendomein wordt verdeeld in segmenten met voor elk segment geschikte expansies.
   Dit proefschrift, hoofdstuk 2.

2. De numerieke methode zoals beschreven in hoofdstuk 2 is robuust in de zin dat voor bestudeerde test cases verschillende expansies dezelfde resultaten geven.
   Dit proefschrift, hoofdstuk 3.

3. Een temperatuur distributie ontstaan ten gevolge van Marangoni convectie of ten gevolge van diffusie hangt af van eigenschappen van de vloeistof, met name de viscositeit en de gevoeligheid van de vloeistof voor vervuiling.
   Dit proefschrift, hoofdstuk 4.

4. De zogeheten destillocapillaire convectie geïnduceerd in de meniscus van een waterlaag zich bevindend op een hydrofiel oppervlak, resulteert in een droger oppervlak dan bij een conventionele techniek zoals centrifugeren kan worden bereikt.
   J. Marra en J.A.M. Huethorst, Physical principles of Marangoni drying, Langmuir **7**, *pp. 2748-2755, 1991.*

5. Indien Marangoni convectie optreedt in condensdruppels op kunststof warmtewisselaars kan dit de warmteoverdracht naar de warmtewisselaar verbeteren.
   C.W.M. van der Geld en H.J.H. Brouwers, The mean condensate heat resistance of dropwise condensation with flowing, inert gases, Int. J. Heat and Mass Transfer **30** *, pp. 435-445, 1995.*

6. Het kwantificeren van destillocapillaire convectie is momenteel nog moeilijker dan die van thermocapillaire convectie omdat technieken om een concentratiegradiënt langs een interface te meten nog niet zo goed zijn ontwikkeld als die voor het meten van een temperatuurgradiënt langs een interface.

7. Het voortdurend up to date houden van software wordt door sommigen verheven tot doel in plaats van dat het eigenlijke gebruik ervan wordt gezien als hulpmiddel.

8. Het handhaven van de internationale vrede is gebaseerd op economisch eigenbelang.

9. De milieu-problematiek is door de jaren heen steeds meer een mode verschijnsel geworden. Het wordt tijd voor een nieuwe collectie.

10. Het getuigt van kennis om je onwetendheid te tonen.

11. Hoe meer kennis je vergaart, des te duidelijker wordt het dat er nog veel kennis te vergaren is.

12. Tegenwoordig worden veel applicaties zoals bijvoorbeeld tekstverwerkers zo groot dat het werken ermee te vergelijken is met "het naar de bakker gaan in een Boeing 747".
    H. Blankesteijn in "Technisch Weekblad", 19-04-1995.

Anton den Boer
Tilburg, september 1996